POLITECNICO DI TORINO

Facoltà di Ingegneria

Corso di Laurea Magistrale in Ingegneria Meccanica

Tesi di Laurea Magistrale

Laminar flame speed prediction for Natural Gas/Hydrogen blends and application to the combustion modeling in IC Engines

Relatori:

prof. Mirko Baratta

prof. Daniela Misul

prof. Fabian Mauss

Ing. Corinna Netzer

Tutor aziendale:

Ing.Lars Seidel

Candidato:

Francesco Arpaia(s241986)

Aprile 2019

Joint work with:

[1]

[2]

[1]: LOGE AB – Lund Combustion Engineering, Cottbus (Germany)

[2]: BTU – Brandenburg University of Technology, Cottbus (Germany)

Sommario

Abstract

In recent years, air quality has become a severe problem in many countries. The use of natural gas as an alternative fuel has been growing in recent years, since it is a promising alternative fuel to meet strict engine emission regulation. Natural gas has the potential to provide a good compromise in cost, efficiency and emission when used in Internal Combustion Engines. Thanks to its higher resistance to auto-ignition, engine efficiency can be increased through the use of higher compression ratios. Its high H/C ratio thanks to its low carbon level leads to less carbon dioxide, carbon monoxide and hydrocarbon emissions compared to gasoline fuels. The lower peak combustion temperatures under lean conditions, in comparison to stoichiometric conditions, lead to a lower knock tendency. The main problem of this type of engines is that the methane burns quite slowly. This causes reduced thermal efficiency and increased fuel consumption, due to significant cycle-to-cycle variations and reduced power. This work investigates the prediction of laminar flame speed using 3D and 0D SI-SRM. To cope with that problem, different blends were studied, with specific reference to the addition of hydrogen. As the laminar flame speed is one of the most relevant parameters for the prediction of the combustion properties inside the engine cylinder, its evaluation has been the main target of this work. The laminar flame speed has been calculated with two different approaches. First the Freely Propagating Flame Module in LOGEresearch has been used, that performs combustion and chemical kinetics simulation for different surrogate composition. Second, the laminar flame speed for the single surrogate components has been calculated and applied in a new correlation tool to compose the flame speeds for the multicomponent surrogate. The flame speeds calculated with both approaches are stored in look-up tables and retrieved within the engine simulation. It is fundamental to choose a good kinetic mechanism and to validate it. It was found that an accurate evaluation of the laminar flame speed has been carried out for a wide range or pressure, temperature, EGR and Equivalence ratio. The generated and validated flame speed tables are applied in 3D and 0D engine simulations for further validation, considering MFB50.

1. Introduction

in this first chapter, an overview of the main differences between a common fuel and an alternative fuel (such as Natural Gas) are shown. The main differences in terms of performance and properties on an Internal combustion engine are exposed.

1.1. Performance of an Internal Combustion Engine (ICE)

The power supplied by an Internal Combustion Engine is normally indicated with P_U (Net Power) that is the power made available to the crankshaft [1]. The power can be expressed as (1):

$$P_u = C\omega \ (1)$$

That is a volumetric machine, so the useful power supplied can be written also as (2):

$$P_u = L_u i \frac{n}{m} \ (2)$$

Where:

- L_U the net work per cycle and for each cylinder (3);
- i number of cylinders;
- n/m number of rotates per unit of time [rps];
- m number of crank revolutions for each power stroke per cylinder (m=1 in 2T, m=2 in 4T);

The Net Work is function of the energy that is available for each cycle thanks to the process of combustion (conversion of thermal chemical energy in thermal energy):

$$L_u = \eta_u E_u = \eta_u m_b H_i \ (3)$$

Where:

- E_u Net Energy per cycle [kJ];
    - m_b mass of fuel used per cycle for each cylinder [kg]
    - α Air-to-Fuel ratio, equal to (4):

$$\alpha = \frac{m_a}{m_b} = {}^{A}/_{F} \ (4)$$

- m_a mass of air aspirated per cycle for each cylinder;

- H_i lower heating value [kJ/kg];
- η_u useful efficiency.

Using the relation (3) and (4), the (2) becomes:

$$P_u = \eta_u \frac{m_a}{\alpha} H_i i \frac{n}{m} \quad (5)$$

By observing the relation (5), it is possible to notice that the parameters directly linked with the fuel properties are α and H_i; so, by modifying these parameters, it is possible to improve the engine power. It is important to introduce the *air to fuel* ratio also because in a volumetric machine the space available to store the working fluid at each cycle is limited. The value of α can't deviate much from value of the α_{st} .For that reason to compare fuels with different characteristics we can't consider only the α but we must consider the *energetic parameter* H_i/α_{st} . In the following *Table 1* a comparison between several types of fuels used in engine is made.

Fuel	Lower heating value [MJ/kg]	Stoichiometric dosing [-]	Energetic parameter [MJ/kg]
Diesel	42.5	14.5	2.93
Gasoline	44.0	14.6	3.01
Methane	50.0	17.2	2.90
Hydrogen	120.0	34.3	3.5

Table 1: Parameter for different fuels

Another important parameter to consider is the *volumetric efficiency* (λ_V) defined as the ratio of the mass density of the air-fuel mixture drawn into the cylinder at atmospheric pressure (during the intake stroke) to the mass density of the same volume of air in the intake manifold:

$$\lambda_V = \frac{m_a}{m_{a,rif}} = \frac{m_a}{\rho_a V} \quad (6)$$

Where:

- m_a mass of air aspirated per cycle for each cylinder [kg];
- $m_{a,rif}$ mass of air theoretically aspirated [kg];
- ρ_a air density [kg/m^3];
- V cylinder displacement [m^3]

Replacing the (6) in the (5):

$$P_u = \eta_u \frac{\rho_a \lambda_V}{\alpha} H_i \; i \; V \frac{n}{m} \quad (7)$$

But, to compare engines with different displacements, it is possible to use another parameter called *mean effective pressure* (mep). Even if it contains the word "pressure" it's not an actual pressure measurement within the engine cylinder. By definition, mean effective pressure is the ratio between the work and engine displacement (8):

$$mep = \frac{L_u}{V} = \eta_u \frac{\lambda_v \rho_a H_i}{\alpha} \quad (8)$$

Where:

- V cylinder displacement [m^3];
- L_u work performed in a complete engine cycle [J];

Considering all the parameters of the mep:

- η_u for automotive application it is equal to 0.3-0-4, limited by thermodynamic reasons;
- ρ_a its value is 1.2 Kg/m^3, if the air is aspirated at standard conditions (p=1 bar and T=293 K);
- λ_v for naturally aspirated engines, its value is about 0.8-0-9;
- $\frac{H_i}{\alpha}$ its value depends from the fuel.

The only way to improve the performance of the engine is to try to improve the volumetric efficiency, the fuel used and the air density. Considering the energetic parameter, the fuel with a higher value of it is the hydrogen, but It has also the problem that is mixed with the air in gaseous state and for this reason the value of the volumetric efficiency it is not acceptable. It is possible to increase the air density by using turbocharging system and the volumetric efficiency by modifying the valve and the intake runners. Thanks to the turbocharging the air density could reach also values 2.5 times higher than those of naturally aspirated engines.

Here is the comparison between the performance of a SI and a CI engine:

SI Engine	CI Engine
η_u=0,3	η_u=0,35
λ_v=0,9	λ_v=0,9
ρ_a=1,2 kg/m^3	ρ_a=1,2 kg/m^3
H_i=44 MJ/kg	H_i=42,5 MJ/kg
$\alpha \simeq \alpha_{st}$=14,6	$\alpha \simeq \alpha_{st}$=17,5
$mep \simeq$10 bar	$mep \simeq$9 bar

Table 2: Comparison between the performance of a SI engine and a CI engine

Both the engines in the *Table 2* have a naturally aspirated system. CI engines have a lower mep than SI engines because the fuel of CI engine has a lower energetic parameter but also because CI engine needs to work with an excess of air to guarantee a good combustion. But the advantage of CI engine has the possibility to reach higher values or compression ratio and higher levels of turbocharging; thanks to this a turbocharged CI engine can reach a mep of 20÷25 bar. This is not possible for SI engines because at elevated levels of turbocharging there could be phenomena of knocking caused by auto-ignition of the mixture. Unfortunately, using high levels of turbocharging, in a CI engine, high temperatures are reached during combustion, these cause high NOx emissions. For

that reason, there was the introduction of methane and it became one of the most valid alternatives to common fuels thanks to its properties.

1.2. Natural Gas Engines

Natural gas is promising alternative fuel to meet strict engine emission regulations in many countries. Compressed natural gas (CNG) has long been used in stationary engines, but the application of CNG as a transport engines fuel has been considerably advanced over the last decade by the development of lightweight high-pressure storage cylinders [25]. It is a fossil fuel that has been investigated for use in spark-ignition (SI) and compression-ignition (CI) engines. It is a cleaner fuel than either gasoline or diesel as far as emissions are concerned. Compressed natural gas is an environmentally clean alternative to those fuels. Compared with conventional gasoline engines, SI engines using natural gas, thanks to its anti-knocking properties can run at higher compression ratios (up to 16:1 without "knock"), thus producing higher thermal efficiencies [26]; its low carbon level guarantees an high H/C ratio which allows a reduction of the emissions of carbon dioxide (CO2) about 20-25% if compared with gasoline, carbon monoxide (CO), unburned hydrocarbons (HC) and particulate matter (PM) but at the same time, because of these high temperatures reached, there is an increase of the emissions of nitrogen oxide (NOx). High NOx emissions, especially at high loads, can be reduced with exhaust gas recirculation (EGR) because adding EGR to the inlet mixture will reduce the oxygen partial pressure in the inlet mixture, and consequently the in-cylinder NOx production will decrease; but in this case the EGR rate is limited due to its low burning velocity because it would makes the mixture less reactive and then the propagating flame too slow. While CNG engines offer many advantages over conventional gasoline and diesel combustion engines, their performance can be improved in the lean operating region. Lean operation has several benefits, the most important is reduced emissions [27]. However, the extremely low flame propagation velocities of CNG restrict the lean operating limits of CNG engines. Hydrogen, however, has a high flame speed and a wide operating limit that extends into the lean region. The addition of hydrogen to a CNG engine makes it a viable

and economical method to significantly extend the lean operating limit and thus improve performance and reduce emissions. The addiction of hydrogen allows combining the benefits of both methane and hydrogen in terms of lower pollutant emissions and increased combustion velocity [54]. Hydrogen itself represents a promising alternative to gasoline, even though, the lack of distribution infrastructure limits its use ad an additive. Drawbacks of hydrogen as a fuel source, include lower power density due to a lower heating value per unit volume as compared to CNG, and susceptibility to pre-ignition and engine knock due to wide flammability limits and low minimum ignition energy. Combining hydrogen with CNG, however, overcomes the drawbacks characteristic of each fuel type.

Like methane and hydrogen is a lighter than air type of gas and can be blended to reduce vehicle emission by an extra 50%. Natural gas composition varies considerably over time and from location to location. Methane content is typically, 70-90% with the reminder primarily ethane, propane and carbon dioxide.

2. Premixed Combustion

In premixed combustion, fuel and oxidizer are mixed at the molecular level prior to ignition. This creates a thin flame front as all the reactants are easly available. Combustion occurs as a flame front propagating into the unburnt reactants. This premixing is possible only at sufficiently low temperatures where the chain-breaking mechanism that drives the reaction chain in hydrogen and hydrocarbon oxidation is unable to compete with the effect of three-body chain breaking reactions. Under such low-temperature conditions, combustion reactions are considered frozen. The frozen state is metastable because a sufficiently strong heat source, a spark for example, can raise the temperature above the threshold and initiate combustion. Once the fuel and oxidizer species have been homogeneously mixed, and a heat source is supplied, a flame front can propagate through the mixture.

Examples of premixed combustion include aspirated internal combustion engines, lean-premixed gas turbine combustors, and gas-leak explosions.

2.1. Laminar Premixed Flame

When a premixed gaseous mixture of fuel and oxidizer inside the flammability limits is contained in a long tube, a combustion wave will propagate down the tube from the burned gases to the unburned gases (*Figure 1*) if an ignition source is applied at one end. If the tube is opened at both ends, the velocity of the combustion wave is in the range of 20-200 cm/s [9]; its velocity is controlled by transport processes, mainly simultaneous heat conduction and diffusion of radicals. This low speed (subsonic) flame propagation is called “Deflagration”. This combustion wave is normally referred to as a “*flame*”.

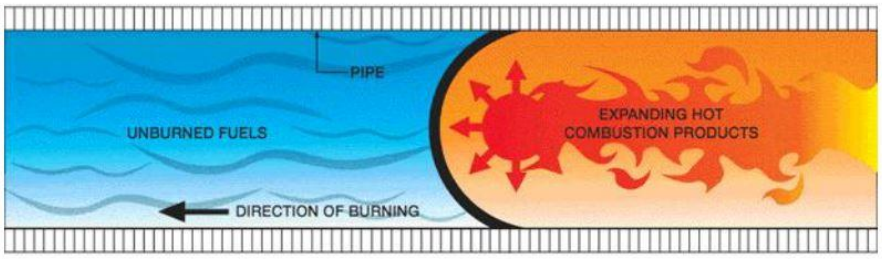

Figure 1: Combustion wave

If the tube is closed at the ignition end, the flame will accelerate in the tube as it propagates. Eventually it will transition from subsonic to supersonic. This supersonic process is called a "*detonation*". In a detonation, the shock wave which occurs at supersonic velocity raises T and P of the mixture to create an explosive reaction and energy release to sustain wave propagation (*Figure 2*).

Figure 2: Combustion wave fixed in laboratory frame

To better understand the structure of this flame wave phenomenon we will apply the conservation equations.

- $\rho_1 u_1 = \rho_2 u_2$ continuity; (9)
- $p_1 + \rho_1 u_1^2 = p_2 + \rho_2 u_2^2$ momentum; (10)
- $c_p T_1 + \frac{1}{2} u_1^2 + q = c_p T_2 + \frac{1}{2} u_2^2$ energy; (11)

Also, we can use the ideal gas equation of state. However, note that the final state equation is not independent of the initial state equation.

- $p_1 = \rho_1 R T_1$ state; (12)
- $p_2 = \rho_2 R T_2$ state; (13)

Where:

- q is the chemical energy release;

Thus, there is a system of 4 equations and 5 unknowns $(u_1, u_2, p_2, T_2, \rho_2)$ .However, combining the equations we can obtain two new equations (14) (15) given as:

$$\frac{\gamma}{\gamma-1}\left(\frac{p_2}{\rho_2}-\frac{p_1}{\rho_1}\right)-\frac{1}{2}(p_2-p_1)\left(\frac{1}{\rho_1}+\frac{1}{\rho_2}\right)=q \quad (14)$$

$$\gamma M_1^2=\left(\frac{p_2}{p_1}-1\right)\Big/\left[1-\frac{(1/\rho_2)}{(1/\rho_1)}\right] \quad (15)$$

Where:

- γ is the ratio of specific heats and it is equal to $\frac{C_p}{C_v}$;
- $M_1$is the Mach number, defined as the local gas velocity divided by the local speed of the sound, *c*:

$$M_1=\frac{u_1}{c_1}=\frac{u_1}{\sqrt{\gamma R_1 T_1}}$$

In CONVERGE, to simulate premixed combustion, it is available the level set *G-Equation model* and it is considered a less predictive combustion model because its derivation includes some simplifications.

2.1.1. Laminar Flame Speed

The flame velocity – also called the burning velocity, normal combustion velocity, or laminar flame speed – is defined as the velocity at which unburned gases move through the combustion wave in the direction normal to the wave surface and it is an important parameter for the flame propagation prediction. It depends on the fuel type, air-fuel ratio, temperature and pressure and, as we will see later, it can be calculated with good approximation also by kinetic mechanisms for various fuels.

Theoretical analyses for the determination of the laminar flame speed:

- Thermal theories:
    - Mallard and LeChatelier who postulated that heat transfer (specifically thermal conductivity) is the driving mechanism. In their work the flame was divided into two regions: an inert *Preheat Zone* and a chemically active *Reaction Zone*.
    - Zeldovich and Frank-Kamenetskii included the diffusion of molecules as well as heat but did not included the diffusion of free radicals or atoms.

2.1.1.1. Theory of Mallard and LeChatelier

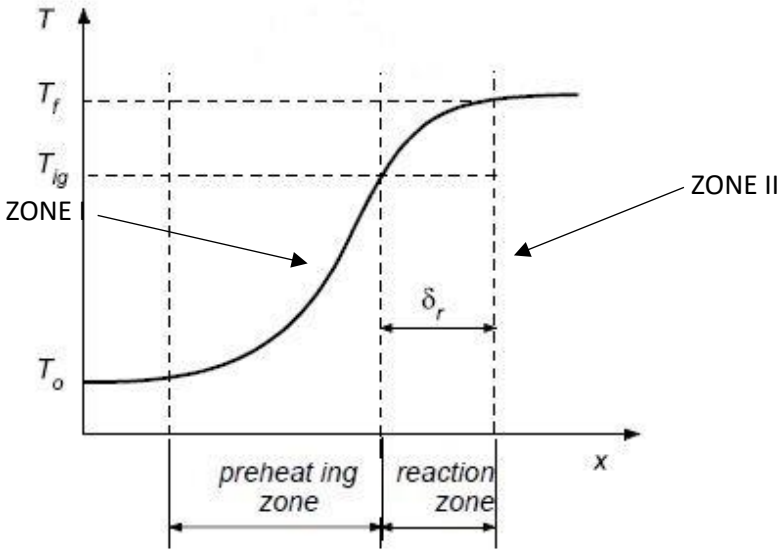

Figure 3: Schematically illustration of the temperature and the zone in the theory of Mallard and LeChatelier [58]

According to Mallard and LeChatelier, the flame is divided into two regions (*figure 3*): the burning region (zone I) with the flame thickness d and the conduction region (zone II) in which the unburnt gases are heated up. In order for the flame to be self-sustaining, the amount of heat conducted from the burning zone must be sufficient to raise the temperature of the unburned fuel/air mixture to its ignition temperature. Thus, they theorized that in Zone I the gases are heated from their initial temperature, T_0, to their ignition temperature, T_{ig}, by heat from the combustion reaction conducted from Zone II into Zone I. The excess energy released from the combustion reaction then further raises the temperature of the gases from T_{ig} to the flame temperature T_f. They analysed this process by linearizing the temperature change in Zone II and by setting the sensible heat necessary to raise the unburned gases from T_0 to T_{ig} equal to the heat conducted from the flame into Zone I. The energy balance then is given by (16):

$$\dot{m}C_p(T_i - T_0) = \lambda \frac{(T_f - T_{ig})}{\delta} A \quad (16)$$

Where:

- λ thermal conductivity

If we treat this flame propagation as a 1–D problem, then the mass flow rate (17) in the preheat region is given by:

$$\dot{m} = \rho A u = \rho S_L A \text{ (17)}$$

Where:

- $\dot{m} = \frac{dm_b}{dt}$ is the mass burning rate;
- A is the cross section area;
- ρ is the density;
- u is the velocity of unburned gas;
- S_L is the symbol for the laminar flame velocity, because the unburned gases enter normal to the wave, by definition: $S_L = u$ (18);

$$S_L = \frac{\dot{m}}{A\rho} (18)$$

Laminar flame speed depends on the fuel type, fuel-air ratio, temperature and pressure. It can be calculated with good approximation by kinetic mechanisms for various fuels. So, by replacing the (17) in the (16) the energy balance around the flame becomes (19) or (20):

$$\rho\, S_L C_p (T_i - T_0) = \lambda \frac{(T_f - T_{ig})}{\delta} (19)$$

or

$$S_L = \left[\frac{\lambda}{\rho_u C_p} \frac{(T_f - T_{ig})}{(T_{ig} - T_0)} \frac{1}{\delta}\right] (20)$$

But in this last equation the reaction zone thickness δ is unknown. To remedy the problem, it is possible to use chemical kinetics to get an expression for δ (21):

$$\delta = S_L \tau = S_L \frac{1}{\frac{d\varepsilon}{dt}} = \frac{S_L}{RR} (21)$$

Where*:*

- τ reaction time;
- $\frac{d\varepsilon}{dt} = RR = \dot{\omega}$ reaction rate;

In other words, the faster RR, the thinner is the reaction zone. Eliminating the flame thickness

δ with this relation, yields a quadratic equation for the laminar flame speed (22):

$$S_L = \left(\frac{\lambda}{\rho_u C_p}\frac{(T_f - T_{ig})}{(T_{ig} - T_0)}(RR)\right)^{1/2} \sim (\alpha RR)^{1/2} \quad (22)$$

Where α is the *thermal conductivity* and it is equal to $\frac{\lambda}{\rho_u C_p}$. The laminar flame speed is increasing with reaction rate RR and with thermal conductivity of the unburnt gases since the preheated zone gets smaller. The RR depends on the available oxidizer, T_i and T_f depend on the equivalence ratio and for this reason S_L is limited by the fuel lean and fuel rich limits; the flammability limit is, typically, in the range of ϕ:]0.5-1.5[and at the flammability limits T_i and T_f converge and S_L is zero.

2.1.1.2. Changes made by Zeldovich, Frank-Kamenetskii and Semenov

But note that this result depends explicitly on T_{ig} that is unknown. Zeldovich, Frank-Kamenetskii, and Semenov [58] postulated that the ignition temperature is very close to the final temperature (*figure 4*), that the reaction zone has a virtually nil thickness, and that the profile of *T* in the preheating zone is virtually linear (source/sink term is nil). Hence T_{ig} is eliminated.

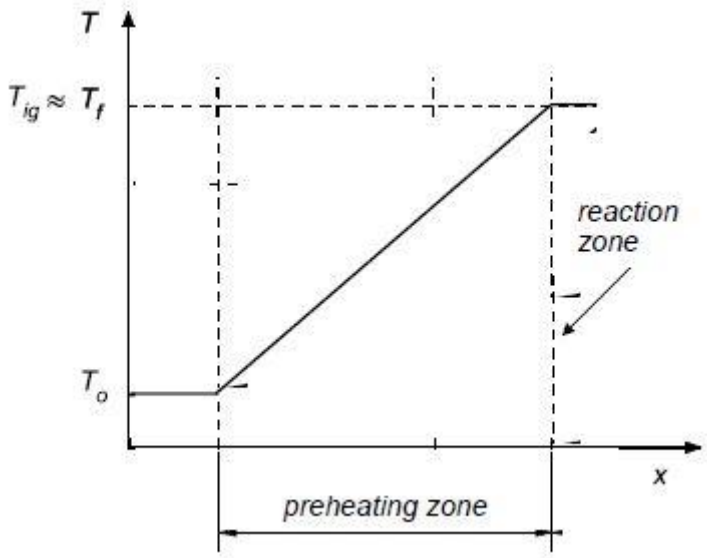

Figure 4: Schematically illustration of the temperature and the zone in the theory of Zeldovich [58]

2.1.1.3. Laminar Flame Speed in CONVERGE

In CONVERGE the laminar Flame Speed can be calculated by one of three different approaches [22]:

- *Metghalchi and Keck correlation (1982);*
- *Gulder correlation (1984);*
- *User-supplied data tables;*

The model used in this work is the *Gulder model* and its correlation is given by (23):

$$s_{l\_ref} = \omega \phi^{\eta} exp[-\xi(\phi - 1.075)^2] \quad (23)$$

Where ω, η and ξ are user-supplied constants appropriate for the fuel and oxidizer used in the simulation. One the s_{l_ref} is calculated at the reference pressure and

temperature, the laminar Flame Speed is adjusted for the actual pressure and temperature thanks to (24):

$$s_l = s_{l\_ref}\left(\frac{T_u}{T_{u\_ref}}\right)^{\gamma}\left(\frac{p}{p_{ref}}\right)^{\beta}(1 - 2.1Y_{dil}) \ (24)$$

Where:

- T_u is the unburned temperature;
- T_{u_ref} is the reference unburned temperature;
- p is the pressure;
- p_{ref} is the reference pressure;
- Y_{dil} is the mass fraction of dilution species;
- γ is the temperature exponent and it is defined as (25):

$$\gamma = a + m(\phi - 1) \ (25)$$

- β is the pressure exponent, defined as (26):

$$\beta = b + n(\phi - 1) \ (26)$$

The coefficients a, b, m, n are different for each fuel and they are tabulated.

2.1.2. Impact of laminar flame speed on a vehicle performance

Laminar burning velocity is an important measurement describing how a planar flame propagates into quiescent unburned mixture ahead of the flame at a specified pressure and temperature. Since the laminar flame speed affects directly the turbulent flame propagation, there is also direct proportionality to engine performance: a fuel with higher S_L leads to a faster combustion [24]. A difference in laminar burning velocity can be carried through into a turbulent combustion regime such as an engine and influence the turbulent burning velocity. In a SI engine, the generation of power occurs by the expansion of gaseous combustion products that exercise pressure on the piston; for an ideal fuel, the combustion process would begin and end when the piston is at the TDC (*top dead centre)* at the end of the compression stroke, because an ideal fuel would burn instantaneously. In the past years several tests were made to prove that there is a

correlation between engine performance and fuels with a higher laminar burning velocity. A faster burning fuel is desirable because the whole torque curve can be shifted to higher torque and earlier spark timings That work was made by Bradley and co-workers and they tested several types of fuel on a single cylinder Ricardo Hydra engine and vehicles sourced from Europe and the US.

Fuels were run in an A-B-A-B-A-B-A sequence where A was the base fuel and B was the test fuel; the reference fuel used was a 95 RON commercial gasoline mixed with 20 vol% of paraffins, olefins and aromatics that increase the laminar flame speed of the base gasoline. The results confirm a correlation between acceleration benefits with laminar burning velocity of gasoline fuel. The observed benefits can be attributed to the changes in V_L, as the spark timing in these experiments was fixed.

3. Software used

3.1. LOGEresearch

LOGEresearch is an intuitive tool [42] for combustion and chemical kinetics simulations. The software can be used in stand-alone mode as well as interfaced with different software. LOGEresearch contains a solver for complex chemical schemes, it contains a transient 1D model for integrated engine combustion and after treatment simulation with detailed chemistry. The after-treatment models complete LOGEresearch's 1D in-cylinder capabilities for analysis and optimization of full powertrain systems. The models are easy to use and numerically fast, but accurate enough to represent, in detail, chemical processes that predict emission levels of soot, NO_x, CO and unburned HC. LOGEresearch 1D offers affordable computational times in comparison to CFD, with the bonus of detailed chemistry. In this work LOGEresearch is used for the calculation of Laminar Flame Speed for several types of pure fuels and blends for a wide range of temperatures, pressures, equivalence ratios and percentage of EGR.

3.2. Flame Speed Generation tool

The flame speed table generation tool (Flame Speed Generator) is delivered with a graphical interface but may also be run in standalone mode. It compiles the Flame speed tables based on precompiled flame speed tables for pure components obtained with LOGEresearch using the LOGEfuel Natural Gas reaction scheme v2.0 and compose the flame speeds for the multicomponent surrogate.

3.3. CONVERGE

As a general purpose CFD solver, CONVERGE is robust out of the box [53]. Autonomous meshing technology built into the solver eliminates the meshing bottleneck that has traditionally bogged down CFD workflows. CONVERGE automatically generates a perfectly structured, orthogonal grid a runtime based on simple, user-defined grid control parameters.

3.4. LOGEengine

LOGEengine [57] applies a 0D model to simulate processes like combustion, emission formation and abnormal combustion in ICE; it also helps to analyse existing engines and to prototype new engine development. It is a combustion analysis tool used for in-cylinder combustion modeling. This software uses a Stochastic Reactor Model for SI engines (SI-SRM), which will be discussed in the next chapter.

4. Models

Different model approaches are used for investigating the problem.

4.1. Laminar S_L model

A flat as a self – sustaining propagation of a localized combustion zone at subsonic velocity [43]. For a premixed laminar flame, the fuel and oxidant mixture move in the *z* direction with the burned mixture at z → ∞ and the unburned mixture at z →-∞. Conservation equations are the follows:

- Continuity: $\frac{d(\rho u)}{dt} = 0$
- Balance of species mass fractions: $\rho u \frac{dY_i}{dz} = -\frac{dj_i}{dz} + \dot{m}_\iota$
- Balance of energy: $\rho u c_p \frac{dT}{dz} = \frac{d}{dz}\left(\lambda \frac{dT}{dz}\right) - \sum_{i=1}^{N_s} h_i \dot{m}_\iota - \sum_{i=1}^{N_s} c_p j_i \frac{dT}{dz} - 4\alpha\sigma(T^4 - T_0^4) f_r$

where ρ is the density, *u* the gas velocity component, Y_i the mass fraction, j_i the diffusion flux and $\dot{m}$ the production rate of species i and N_s is the number of species. α is Planck's constant, σ the Stefan Boltzmann constant, T_0 the temperature of the surroundings and f_r a radiation factor. The species considered for radiation are CO_2 and H_2O and this factor represents the fraction of volume of burned gas to unburned gas. Its standard value in a supposed situation is 0.5 but it is possible to change it.

4.1.1. Freely Propagating Flame

The Freely Propagating Flame model is used for calculations of flame speeds and species concentration profiles in laminar freely propagating flames in LOGEresearch [43]. flame is defined as a self-sustaining propagation of a localised combustion zone at sub-sonic velocity. The freely propagating flame is a hypothetical model of a flat and infinitely large flame front propagating through a premixed medium. Due to its infinite extent no boundary conditions need to be considered and the total energy of the system can be regarded as constant. Also, phenomena such as flame strain and corresponding mass transfer in the direction normal to the flow field of the fuel and oxidizer are absent. The continuity equations describe the conservation of momentum, *ρu*, over the flame zone

and continuity requires that the speed of the burned gases is higher than that of the unburned gases (27):

$$\rho_u u_u = \rho_u S_L = \rho_b u_b \ (27)$$

The Freely Propagating Flame follows the conservation equations above.

4.1.2. Reaction scheme

The reaction scheme describes the transformation to be performed on the reactant molecules, it is a set of elementary reaction. Any elementary chemical reaction can be represented by the general equation (28):

$$\upsilon'_A A + \upsilon'_B B + \ldots = \upsilon''_C C + \upsilon''_D D + \cdots (28)$$

where υ are known as stoichiometric coefficients, defining how many moles of the given species take part in the reaction.

A net stoichiometric coefficient, υ_S (29), gives the total number of moles of species S that is produced or consumed by a reaction.

$$\upsilon_S = \upsilon''_S - \upsilon'_S \ (29)$$

The reaction rate $\dot{\omega}$, in a first approximation, can be expressed as the rate at which reactants are used up or products are formed.

$$\dot{\omega} = -\frac{\Delta[R]}{\Delta t} = \frac{\Delta[P]}{\Delta t} \ (30)$$

Where:

- $\Delta[R]$: is the concentration of the reactants
- $\Delta[P]$: is the concentration of the products

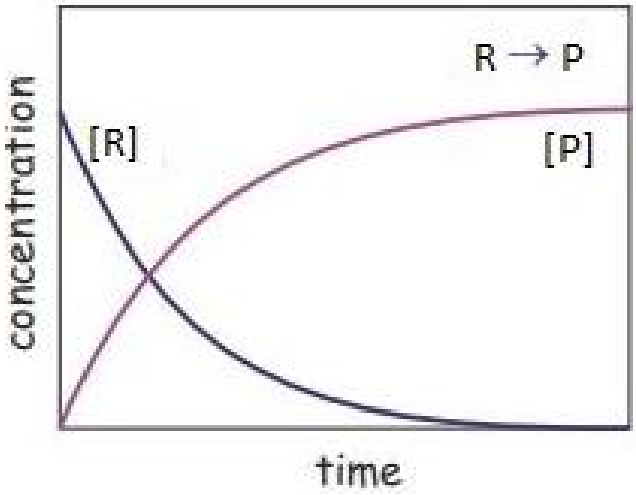

Figure 7: Change in the concentration of reactant and of the product over time

The rate is simply the slope of a plot of reactant or product concentration vs time. The mathematic relation that describes the reaction rate with the change in concentration of reactant is called *kinetic equation*. If we consider a generic reaction (31), it is possible to write:

$$v = k[A]^m[B]^n \ (31)$$

The exponents *m* and *n* denote the *reaction order*, they are calculated with experimental procedure. k denotes the *rate constant* or *reaction rate coefficient* and quantifies the rate of a chemical reaction when the molar concentrations of A and B are unitary; its value is given by the "modified" Arrhenius equation (32):

$$k = AT^n e^{-\frac{E_a}{RT}} \ (32)$$

- E_a is the activation energy representing the energy barrier, that needs to be overcome to initialize the progress of a reaction;
- R is the gas constant;
- T is the absolute temperature [K];
- A is the pre-exponential factor, it is the frequency of collisions in the correct orientation;
- n is the temperature correction of *A*;

A, n and E_a are empirical factors, specified for each reaction it is possible to obtain them with theoretical consideration or experiments. This equation is called "modified" because it makes explicit the temperature dependence of the pre-exponential factor, the original Arrhenius expression has a value of *n* equal to zero. The value for these coefficients are stated for each reaction in data input files and can be studied with the *LOGE mechanism overview module,* its aim is to help to explain the details of the chemical mechanism, to review all thermodynamic, kinetic and transport data.

4.1.2.1. Kinetic mechanism

Chemical kinetics is the study of rates of chemical processes. It includes the study of conditions that influence the speed of a chemical reaction, understanding the kinetic mechanism and building mathematical models that describe the characteristics of a chemical reaction. Each kinetic mechanism is characterized by a given number of reaction and of chemical species that take part to the combustion process; this number defines the computational load of the simulation and the time for obtaining the results. The mechanisms used for the work are shown in the follow table:

Mechanism	Species	Reactions
GRI 3.0	53	325
USC_II	111	784
LOGE	298	2262

Table 3:Numbers of species and reactions for three different chemical mechanisms

Here below are shown some validation results for the three mechanisms:

- Methane (CH_4) (*Figure 8*);

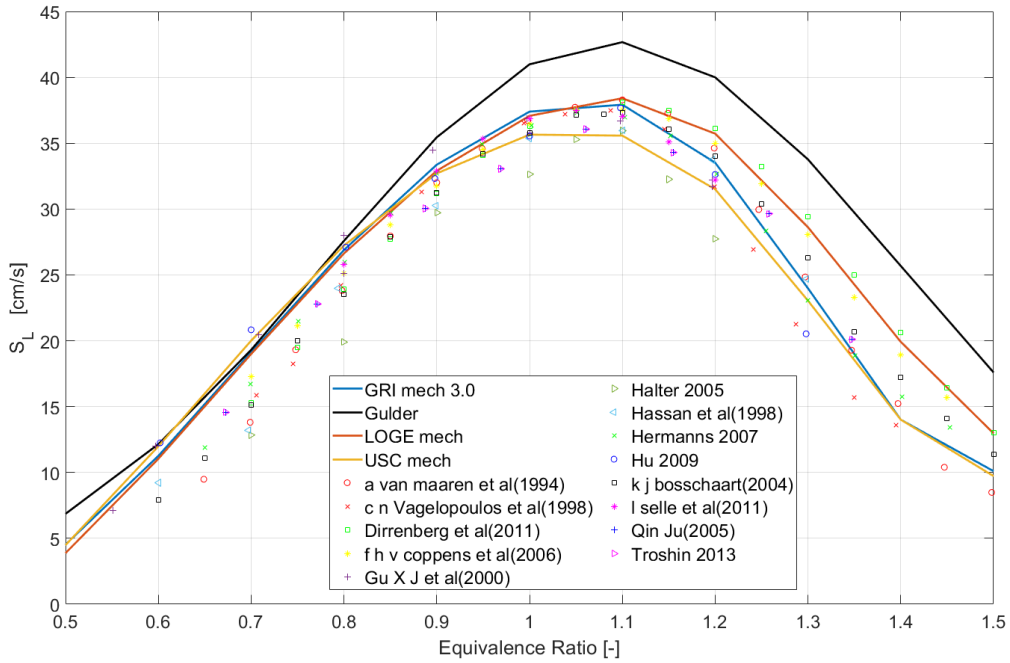

Figure 8: Laminar flame speed of CH_4 / air at 1 atm and 298 K. Symbols ([2], [10],[11],[12],[13],[14],[15],[16],[17], [18],[19],[20]) represent experimental data, line is the calculations with detailed scheme (GRI 3.0 mechanism [4] and LOGE mechanism) and the black line is the flame speed obtained with Gulder equation (23)

- Ethane (C_2H_6) (*Figure 9*);

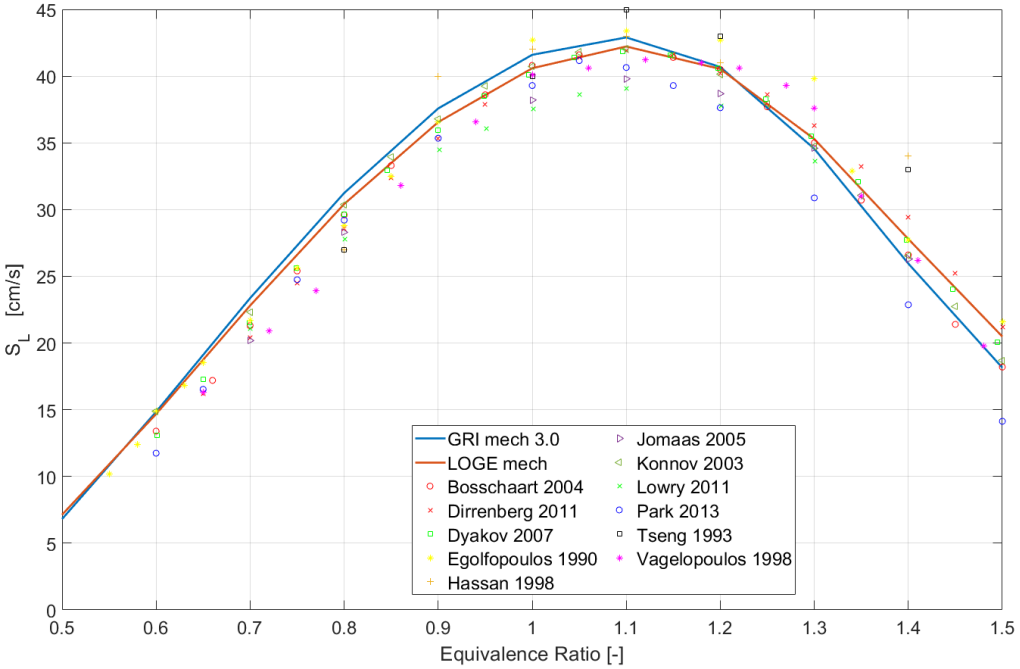

Figure 9: Laminar flame speed of C_2H_6 / air at 1 atm and 298 K. Symbols ([2],[12],[16],[20],[28],[29] ,[30] ,[31] ,[32] ,[33] ,[34]) represent experimental data, line is the calculations with detailed scheme (GRI 3.0 mechanism [4] and LOGE mechanism)

- Propane (C_3H_8) (*Figure 10*);

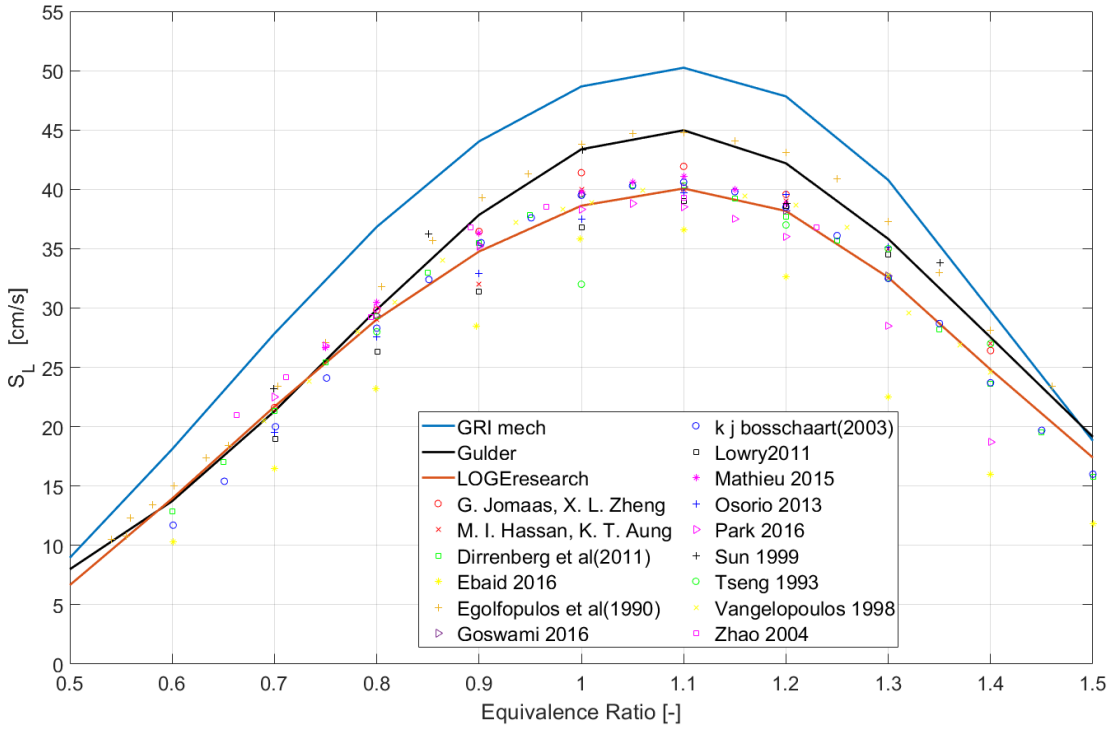

Figure 10: Laminar flame speed of C2H6 / air at 1 atm and 298 K. Symbols ([12],[16],[20],[29] ,[30],[35],[36],[39]) represent experimental data, line is the calculations with detailed scheme (GRI 3.0 mechanism [4] and LOGE mechanism) and the black line is the flame speed obtained with Gulder equation (23)

- Iso-Butane (I- C_4H_{10}) (*Figure 11*);

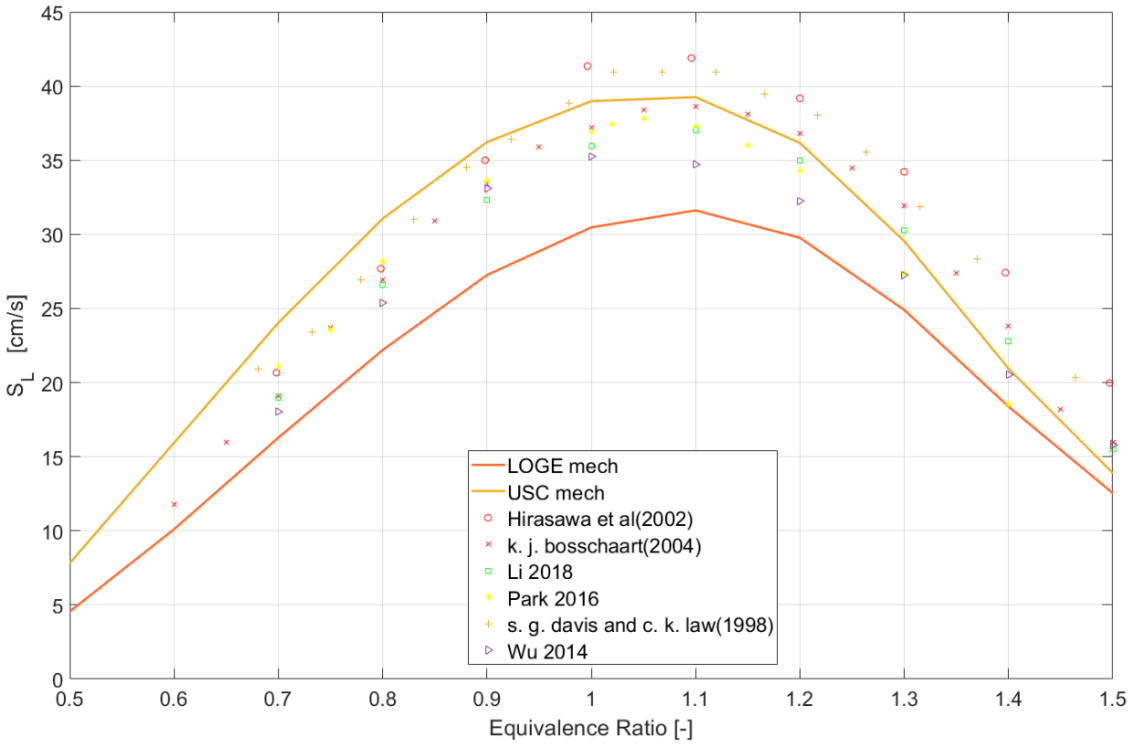

Figure 11: Laminar flame speed of C2H6 / air at 1 atm and 298 K. Symbols ([12], [47], [48], [49], [50], [51]) represent experimental data, line is the calculations with detailed scheme (LOGE mechanism and USC mechanism [52])

4.1.2.2. Reaction mechanism

LOGEresearch [44] uses information available in a chemical mechanism to simulate chemical reactions. A mechanism consists of three different files:

- *Gas Phase Data*: data files state which chemical elements that are included in the mechanism as well as the chemical species these elements make up. Thereafter the data files present a list of reactions the species may participate in and corresponding coefficients, A, n and E_a, used in the Arrhenius law reaction rate calculation. Variables for calculating the rate of the backwards reactions are also stated in the gas phase file. Below is an example of the structure of a gas phase data file. Below is an example of its structure (*Figure 12*)

```
ELEMENTS
O  H  C  N  AR
END
SPECIES
H2       H        O        O2       OH       H2O      HO2      H2O2
C        CH       CH2      CH2(S)   CH3      CH4      CO       CO2
HCO      CH2O     CH2OH    CH3O     CH3OH    C2H      C2H2     C2H3
C2H4     C2H5     C2H6     HCCO     CH2CO    HCCOH    N        NH
NH2      NH3      NNH      NO       NO2      N2O      HNO      CN
HCN      H2CN     HCNN     HCNO     HOCN     HNCO     NCO      N2
AR       C3H7     C3H8     CH2CHO   CH3CHO
END
!THERMO
! Insert GRI-Mech thermodynamics here or use in default file
!END
REACTIONS
2O+M<=>O2+M                                 1.200E+17   -1.000        .00
H2/ 2.40/ H2O/15.40/ CH4/ 2.00/ CO/ 1.75/ CO2/ 3.60/ C2H6/ 3.00/ AR/  .83/
O+H+M<=>OH+M                                5.000E+17   -1.000        .00
H2/2.00/ H2O/6.00/ CH4/2.00/ CO/1.50/ CO2/2.00/ C2H6/3.00/ AR/ .70/
O+H2<=>H+OH                                 3.870E+04    2.700    6260.00
O+HO2<=>OH+O2                               2.000E+13     .000        .00
O+H2O2<=>OH+HO2                             9.630E+06    2.000    4000.00
O+CH<=>H+CO                                 5.700E+13     .000        .00
```

Figure 12: Example of Gas Phase Data[4]

- *Molecular (Transport) Data*

The molecular data files list the following seven variables for each species in the mechanism:

- chemical name
- indicator for the structure of the species (0 = atom, 1 = linear molecule, 2 = non-linear
- molecule)
- two parameters describing the shape of the Lennard-Jones potential well: well depth divided
- by Boltzmann's constant [K] and collision diameter [Å], i.e. the (finite) distance at
- which the interparticle potential is zero.
- the bond dipole moment [Debye]
- the polarizability [Å]
- the rotational collision number (Z_{ROT}) at 298 K.

Below is an example of the structure of a molecular data file (*figure 13*).

C2H	1	209.000	4.100	0.000	0.000	2.500
C2H2	1	209.000	4.100	0.000	0.000	2.500
C2H2OH	2	224.700	4.162	0.000	0.000	1.000
C2H3	2	209.000	4.100	0.000	0.000	1.000
C2H4	2	280.800	3.971	0.000	0.000	1.500
C2H5	2	252.300	4.302	0.000	0.000	1.500
C2H6	2	252.300	4.302	0.000	0.000	1.500
C2N	1	232.400	3.828	0.000	0.000	1.000
C2N2	1	349.000	4.361	0.000	0.000	1.000
C3H2	2	209.000	4.100	0.000	0.000	1.000
C3H4	1	252.000	4.760	0.000	0.000	1.000
C3H6	2	266.800	4.982	0.000	0.000	1.000
C3H7	2	266.800	4.982	0.000	0.000	1.000
C4H6	2	357.000	5.180	0.000	0.000	1.000
I*C3H7	2	266.800	4.982	0.000	0.000	1.000

Figure 13: Example of Molecular Data [4]

- *State Function (Thermal) Data*

It is calculated such as enthalpy and heat capacity, using polynomial fits. The state function data files contain polynomial coefficients for these fits, so named NASA coefficients. For each species in the mechanism, coefficients for two separate temperature ranges and the temperatures that make up the ranges is provided. The input file also contains information regarding the elemental composition of each species. Since also state function data is species specific, any file that contains data for all species in the

gas or surface phase files can be used. Below is an example of the structure of a State function data. It contains four lines for each species, at the first line there is the name of the species and its composition. The elements are followed by the number of atoms of each element that the molecule contains, and this section is followed by three temperatures that define the end points of the two temperature ranges for which the NASA polynomials are valid. Below is an example of the structure of a state function data file (*Figure 14*).

```
O                 L 1/90O   1               G   200.000  3500.000  1000.000    1
 2.56942078E+00-8.59741137E-05 4.19484589E-08-1.00177799E-11 1.22833691E-15    2
 2.92175791E+04 4.78433864E+00 3.16826710E+00-3.27931884E-03 6.64306396E-06    3
-6.12806624E-09 2.11265971E-12 2.91222592E+04 2.05193346E+00                   4
O2                TPIS89O   2               G   200.000  3500.000  1000.000    1
 3.28253784E+00 1.48308754E-03-7.57966669E-07 2.09470555E-10-2.16717794E-14    2
-1.08845772E+03 5.45323129E+00 3.78245636E+00-2.99673416E-03 9.84730201E-06    3
-9.68129509E-09 3.24372837E-12-1.06394356E+03 3.65767573E+00                   4
H                 L 7/88H   1               G   200.000  3500.000  1000.000    1
 2.50000001E+00-2.30842973E-11 1.61561948E-14-4.73515235E-18 4.98197357E-22    2
 2.54736599E+04-4.46682914E-01 2.50000000E+00 7.05332819E-13-1.99591964E-15    3
 2.30081632E-18-9.27732332E-22 2.54736599E+04-4.46682853E-01                   4
H2                TPIS78H   2               G   200.000  3500.000  1000.000    1
 3.33727920E+00-4.94024731E-05 4.99456778E-07-1.79566394E-10 2.00255376E-14    2
-9.50158922E+02-3.20502331E+00 2.34433112E+00 7.98052075E-03-1.94781510E-05    3
 2.01572094E-08-7.37611761E-12-9.17935173E+02 6.83010238E-01                   4
OH                RUS 78O   1H  1           G   200.000  3500.000  1000.000    1
```

Figure 14: Example of State Function Data [4]

4.2. RANS Reynolds-Averaged Navier-Stokes Simulation

The description of turbulent combustion process using CFD (*Combustion Fluid Dynamics*) it is possible in three ways:

- RANS *Reynolds-Averaged Navier-Stokes:* it was developed to solve for the mean values of all quantities and the balance equations for Reynolds averaged quantities are obtained by averaging the instantaneous balance equations. These equations are obtained from the continuity and momentum equations by taking the time average of all the terms in the equations. The continuity equation does not change since it is linear in terms of the velocity. However, the momentum equation is non-linear, which means that all the fluctuating components do not vanish. Solving these equations provide averaged quantities corresponding to averages over time for stationary mean flows or averages over different realizations for periodic flows like those found in piston engines [5]. This procedure leads to an unclosed system of partial differential equations, so modeling is needed to close the system. The turbulence models introduce a model description of the turbulent viscosity. It can be applied in complex geometries (for example for modeling of engines with moving piston and valves), due its comparably low computational cost and well validated turbulences models for different application. The experiments are usually repeated several times and averaged, so it is easy to compare the mean values obtained with RANS equations, with them.

- LES *Large Eddy Simulations*: the turbulent large scales are explicitly dividing the turbulent flow into two parts: *large-scale* and *small-scale* motion. Large-scale motion is calculated in LES, while the small-scale motion needs to be modeled because of the effects of large-scale motion. The most important aspect in application of LES is the use of suitable sub-grid scale model. LES always solves three-dimensional, time dependent flow, calculating a mean of time-dependent flow fields. Therefore, it is best suited for transient simulations. The LES technique

does not involve the use of ensemble average; rather it consists in applying a spatial filter to N-S equations.

- DNS *Direct Numerical Simulation*: the full instantaneous Navier-Stokes equation are solved without any turbulence approximation, requiring a very fine numerical resolution to capture all the details of turbulence. The theory is that the whole range of spatial and temporal scales of the turbulence must be resolved. All the spatial scales of the turbulence must be resolved in the computational mesh, from the smallest dissipative scales, up to the integral scale *L*, associated with the motions containing most of the kinetic energy.

Those approaches are distinguished by the wave number kw spectrum that is solved or modeled (*Figure 15*)

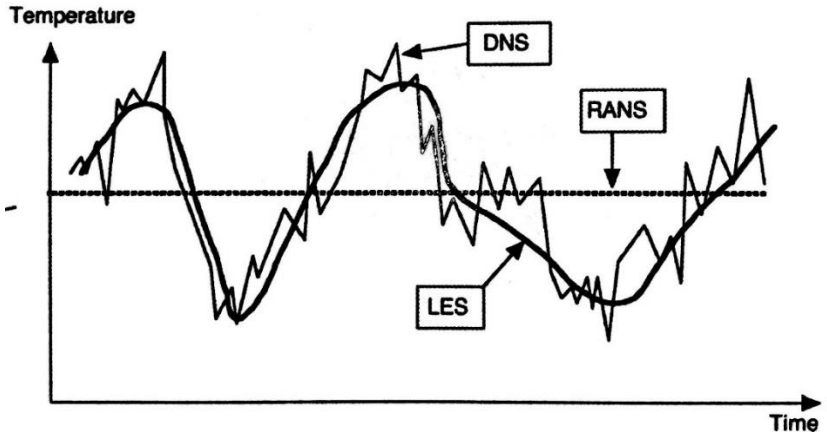

Figure 15: Time evolution of local temperature computed with the three methods in a turbulent flame brush [5]

RANS; LES and DNS properties are summarized in terms of energy spectrum (*figure 16*), all spatial frequencies in the spectrum are determined in direct numerical simulation, while only the largest ones (up to a cut-off wave number k_c) are computed in LES.

The wave number (k_W) is determined by (33):

$$k_W = \frac{(2\pi)}{l_{eddy}} \quad (33)$$

Where:

- l_{eddy}: eddy size

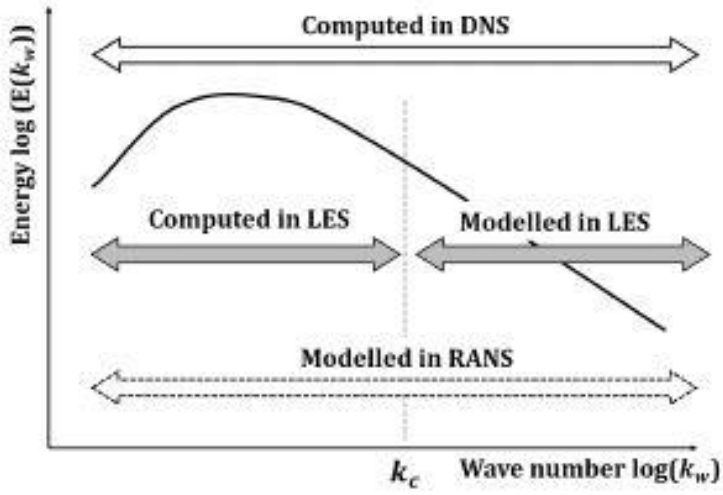

Figure 16: Turbulence energy spectrum plotted as a function of wave number [5].

One primary advantage of RANS is that the calculation load is the lowest among the other three methods, another advantage of RANS is its applicability to any configuration and operating conditions.

Balance equations for the mean quantities in RANS simulations are obtained by averaging the instantaneous balance equations:

- *Mass* $\frac{\partial \rho}{\partial t} + \frac{\partial}{\partial x_i}(\rho u_i) = 0$ (34)
- *Chemical species* $\frac{\partial \rho u_j}{\partial t} + \frac{\partial}{\partial x_i}\left(\rho u_i u_j\right) + \frac{\partial p}{\partial x_i} = \frac{\partial \tau_{ij}}{\partial x_i}$ (35)
- *Momentum* $\frac{\partial (\rho Y_k)}{\partial t} + \frac{\partial}{\partial x_i}(\rho u_i Y_k) = -\frac{\partial}{\partial x_i}\left(V_{k,i} Y_k\right) + \dot{\omega}_k \quad for\ k = 1, N$ (36)
- *Enthalpy* $\frac{\partial (\rho h_s)}{\partial t} + \frac{\partial}{\partial x_i}(\rho u_i h_s) = \dot{\omega}_T + \frac{Dp}{Dt} + \frac{\partial}{\partial x_i}\left(\lambda \frac{\partial T}{\partial x_i}\right) - \frac{\partial}{\partial x_i}\left(\rho \sum_{k=1}^{N} V_{k,i} Y_k h_{s,k}\right) + \tau_{ij} \frac{\partial u_i}{x_j}$ (37)

Where:

- Y_k is the mass fraction
- h_s is the sensible enthalpy $h_s = \int_{T_0}^{T} C_p dT$ (38)
- τ_{ij} is the viscous tensor

- $V_{k,i}$ is the i- component of the diffusion velocity V_k of species *k;*
- $\dot{\omega}_k$ is the reaction rate of species *k;*

Considering constant density flows, Reynolds or time averaging consists splitting any quantity *f* in to mean and fluctuating components as (39):

$$f = \bar{f} + f' \ (39)$$

If we consider this procedure in mass conservation equation (34), the result will be:

$$\frac{\partial \bar{\rho}}{\partial t} + \frac{\partial}{\partial x_i}(\overline{\rho u_i}) = \frac{\partial \bar{\rho}}{\partial t} + \frac{\partial}{\partial x_j}\left(\overline{\rho u_i} + \overline{\rho' u_i'}\right) = 0 \ (40)$$

Where:

- $\overline{\rho' u_i'}$ is an unclosed quantity, it is corresponding to the correlation between density and velocity fluctuations and it requires modeling. Using Reynolds averaging for variable density flows introduces a lot of other unclosed correlation and need closure, in a turbulent combustion the density is not constant. To avoid the generation of fluctuation terms that needs to be modelled it is introduced the Favre averages (41) (*density weighted average*):

$$\tilde{f} = \frac{\overline{\rho f}}{\bar{\rho}} \quad or \quad \bar{\rho}\tilde{f} = \overline{\rho f} \ (41)$$

Any quantity *f* may be split into mean and fluctuating components:

$$f = \tilde{f} + f'' \ (42)$$

$$\bar{\rho}\tilde{f} = \overline{\rho f} = \overline{\rho(\tilde{f} + f'')} = \bar{\rho}\tilde{f} + \overline{\rho f''} \ (43)$$

It remains:

$$\overline{\rho f''} = 0 \quad so \quad \overline{f''} = 0 \ (44)$$

Thanks to (44), averaging equations lead to:

- *Mass*: $\frac{\partial \bar{\rho}}{\partial t} + \frac{\partial}{\partial x_i}(\bar{\rho}\tilde{u}_i) = 0 \ (45)$
- *Momentum:* $\frac{\partial \bar{\rho}\tilde{u}_i}{\partial t} + \frac{\partial}{\partial x_i}\left(\bar{\rho}\tilde{u}_i\tilde{u}_j\right) + \frac{\partial \bar{p}}{\partial x_j} = \frac{\partial}{\partial x_i}\left(\bar{\tau}_{ij} - \bar{\rho}\widetilde{u_i'' u_j''}\right) \ (46)$

- Where $\bar{\tau}_{ij}$ are the mean viscous stress tensor components $\bar{\tau}_{ij} = \mu\left(\frac{\partial \bar{u}_i}{\partial x_j} + \frac{\partial \bar{u}_j}{\partial x_i}\right)$ (47)

- *Chemical species:* $\frac{\partial(\bar{\rho}\tilde{Y}_k)}{\partial t} + \frac{\partial}{\partial x_i}\left(\bar{\rho}\tilde{u}_i\tilde{Y}_k\right) = -\frac{\partial}{\partial x_i}\left(\overline{V_{k,i}Y_k} + \bar{\rho}\widetilde{u_i''Y_k''}\right) + \bar{\dot{\omega}}_k$ (48)

- *Enthalpy:* $\frac{\partial(\bar{\rho}\tilde{h}_s)}{\partial t} + \frac{\partial}{\partial x_i}\left(\bar{\rho}\tilde{u}_i\tilde{h}_s\right) = \dot{\omega}_T + \frac{\overline{Dp}}{Dt} + \frac{\partial}{\partial x_i}\left(\overline{\lambda\frac{\partial T}{\partial x_\iota}} - \bar{\rho}\widetilde{u_i''h_s''}\right) + \overline{\tau_{\iota J}\frac{\partial u_\iota}{x_J}} + -\frac{\partial}{\partial x_i}\left(\rho\sum_{k=1}^{N} V_{k,i}Y_k h_{s,k}\right)$ (49)

Where: $\frac{\overline{Dp}}{Dt} = \frac{\partial \bar{p}}{\partial t} + \overline{u_\iota\frac{\partial \rho}{\partial x_\iota}} = \frac{\partial \bar{p}}{\partial t} + \tilde{u}_i\frac{\partial \bar{p}}{\partial x_i} + \overline{u_i''\frac{\partial \rho}{\partial x_\iota}}$ (50)

Considering Favre and Reynolds averages it is not simple to find a relation between them; it requires the knowledge or the modeling of density fluctuation correlations. Formally the Favre average can be calculated from the time average (51):

$$\bar{\rho}\tilde{f} = \bar{\rho}\bar{f} + \overline{\rho' f'} \text{ (51)}$$

The presence of the Reynolds stresses and turbulent scalar flux in the conservation equations means that the latter are not closes and they contain more variables than there are equations [6]. The unclosed terms are: $\bar{\rho}\widetilde{u_i''u_j''}, \bar{\rho}\widetilde{u_i''Y_k''}, \bar{\rho}\widetilde{u_i''h_s''}$. Closure requires use of some approximations, in fact species and enthalpy fluxes can be approximated using a gradient assumption, but the turbulent Reynolds stresses need to be closed by a turbulence model. Usually, they are described using the viscous tensor τ_{ij} [6]. The Reynolds' stresses are determined using Boussinesq expression (52):

$$\bar{\rho}\widetilde{u_i''u_j''} = \tau_{ij} = -\mu_t\left(\frac{\partial \tilde{u}_i}{\partial x_j} + \frac{\partial \tilde{u}_j}{\partial x_i}\right) - \frac{2}{3}\rho\delta_{ij}k \text{ (52)}$$

Where:

- δ_{ij} is the Kronecker symbol
- μ_t is the turbulent viscosity
- k is the turbulent kinetic energy $k = \frac{1}{2}\widetilde{u_i''u_j''}$ (53)

Now it is important how to solve μ_t, there are three main approaches:

- *Zero-equation model (or Prandtl mixing length model)*
- *One-equation model (or Prandtl-Kolmogorov model)*
- *Two-equation model (or k-ε model)*

4.2.1. Rng k-ε model

In this work the model used is the *k-ε model* [7], it is the most used two-equation turbulence model due to its good convergence rate and relatively low memory requirements; the *ε* is the dissipation rate of turbulent kinetic energy. In particular, it is used the RNG *k-ε model,* it was developed using Re-Normalisation Group theory (RNG, a rigorous statistical technique) methods by Yakhot et al [40] to renormalize the Navier-Stokes equations, to account for the effects of smaller scales of motion. In the standard *k-ε model* the eddy viscosity is determined from a single turbulence length scale, so the calculated turbulent diffusion is that which occurs only at the specified scale, whereas all scales of motion will contribute to the turbulent diffusion. The RNG approach, which is a mathematical technique that can be used to derive a turbulence model like the *k-ε*, results in a modified form of the epsilon equation which attempts to account for the different scales of motion through changes to the production term.

The turbulent viscosity is estimated as:

$$\mu_t = \bar{\rho} C_\mu \frac{k^2}{\varepsilon} \quad (54)$$

Where:

- C_μ is the turbulent viscosity coefficient;

The models use turbulent diffusion and turbulent conductivity terms to account for the presence of turbulence in mass transport and energy transport. The turbulent diffusion D_t and conductivity K_t terms are:

$$D_t = \left(\frac{1}{Sc_t}\right)\mu_t \quad (55)$$

$$K_t = \left(\frac{1}{Pr_t}\right)\mu_t c_p \ (56)$$

Where:

- Sc_t is the turbulent Schmidt number;
- Pr_t is the turbulent Prandtl number;
- D_t is the turbulent diffusion;
- K_t is the turbulent conductivity;

Both the standard *k-ε* and RNG *k-ε models* require additional transport equations to obtain the turbulent viscosity μ_t; one for the turbulent kinetic energy *k* and one for the dissipation of turbulent kinetic energy *ε*. The turbulent kinetic energy transport equation and the transport equation for the dissipation of turbulent kinetic energy are given by (57):

$$\frac{\partial}{\partial t}(\rho k) + \frac{\partial}{\partial x_i}(\rho u_i k) = \tau_{ij}\frac{\partial u_i}{\partial x_j} + \frac{\partial}{\partial x_j}\frac{\mu}{Pr_k}\frac{\partial k}{\partial x_j} - \rho\varepsilon + \frac{c_s}{1.5}S_s \ (57)$$

Where 1.5 is an empirical constant

$$\frac{\partial}{\partial t}(\rho\varepsilon) + \frac{\partial}{\partial x_i}(\rho u_i \varepsilon) = \frac{\partial}{\partial x_i}\left(\frac{\mu}{Pr_\varepsilon}\frac{\partial \varepsilon}{\partial x_j}\right) + c_{\varepsilon 3}\rho\varepsilon\frac{\partial u_i}{\partial x_j} +$$

$$+\left(c_{\varepsilon 1}\frac{\partial u_i}{\partial x_j}\tau_{ij} - c_{\varepsilon 2}\rho\varepsilon + c_s S_s\right)\frac{\varepsilon}{k} + S - \rho R \ (58)$$

Where:

- S is the user-supplied source term;
- S_s is the source term;
- $c_{\varepsilon i}$ are model constants that account for compression and expansion;

As regard R_ε it is equal to zero for standard *k-ε model*, instead for RNG *k-ε model* it is equal to:

$$R_\varepsilon = \frac{C_\mu \eta^3(1-\eta/\eta_0)}{(1+\beta\eta^3)}\frac{\varepsilon^2}{k} \ (59)$$

Where:

- $\eta = \frac{k}{\varepsilon}|S_{ij}| = \frac{k}{\varepsilon}\sqrt{2S_{ij}S_{ij}}$

The effects of this term in the RNG ε equation can be seen more clearly by rearranging the previously equation. Using this equation, $c_{\varepsilon 2}\rho\frac{\varepsilon^2}{k}$ and ρR can be merged, and the resulting ε equation can be rewritten as:

$$c^*{}_{\varepsilon 2} = c_{\varepsilon 2} + \frac{C_\mu \eta^3(1-\eta/\eta_0)}{(1+\beta\eta^3)} \quad (60)$$

In regions where $\eta < \eta_0$, the R term makes a positive contribution and $c^*{}_{\varepsilon 2}$ becomes larger than $c_{\varepsilon 2}$. As a result, for weakly to moderately strained flows, the RNG model yields outcomes comparable to the standard *k-ε model.* In regions of large strain rate $\eta > \eta_0$, the R term makes a negative contribution, making the value of $c^*{}_{\varepsilon 2}$ less than $c_{\varepsilon 2}$. In comparison with the standard *k-ε model,* the smaller destruction of ε arguments ε, reducing *k* and the effective viscosity. As a result, in rapidly strained flows, the RNG model yields a lower turbulent viscosity than the standard *k-ε model*. Thus, the RNG model is more responsive to the effects of rapid strain and streamline curvature than the standard *k-ε model.*

This model is complete since it does not require specifications such as the turbulent length scale $l(x_i)$. Standard values of the model constants of the RNG *k-ε* turbulence model used in the model equations are :

$C_\mu = 0.0845$	$C_{\varepsilon 1} = 1.42$	$C_{\varepsilon 2} = 1.68$	$C_{\varepsilon 3} = -1.0$	$\beta = 0.012$	$\eta_0 = 4.38$

4.3. Combustion ECFM (Extended Coherent Flame Model)

The coherent flame model (CFM) is a combustion model adapted to the flamelet regime. This modeling is mostly suitable to the description of premixed flame combustion, which represents the main oxidation mechanism in SI engines. It supposes that the chemical reaction of fuel oxidation occurs in a very thin layer. The Extended Coherent Flame Model (ECFM) is an extension of the CFM, it was proposed by Marble and Broadwell. It was developed to model combustion in perfectly or partially mixed mixtures, its main aim is to describe the combustion in GDI engines. It is based on a flame surface density equation which considers the wrinkling of the flame front surface by turbulent swirls and conditioning averaging technique which allows to compute more accurately the local properties in fresh and burned gases even in the case of high fuel stratification, which is used to evaluate the local laminar flame speeds [41]. As the reaction rate of CFM-type models is proportional to the laminar flame speed, we expect that the ECFM improved fresh gases description will allow to better account for large scale stratification effect on combustion. To determine the flame surface density, the ECFM uses the fuel/air equivalence ratio in fresh gases, the composition and the temperature near the flame. The model assumes that the smallest turbulence length scales are larger than the laminar flame thickness, so the effect of turbulence is to wrinkle the laminar flame sheet; the increased surface area of the flame results in increased net fuel consumption and an increased flame speed. The range of applicability of the ECFM model is illustrated on the Borghi diagram (*figure 17*):

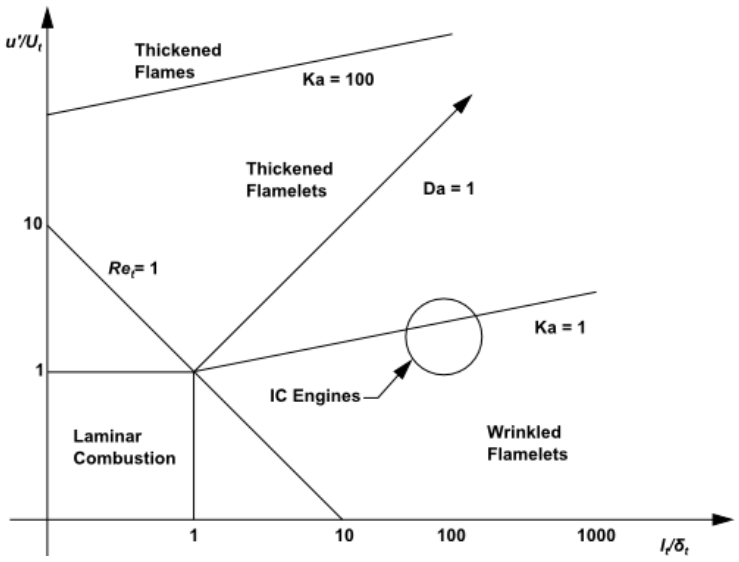

Figure 17: Borghi diagram for turbulent combustion

The wrinkled flamelets regime is indicated below the *Da=1* line. Typical Internal Combustion (IC) engines operate in this wrinkled flamelet range.

This model, as said before, solves an additional equation for the flame area density, denoted ∑ [22]. It is determined by the following transport equation (61):

$$\frac{\partial \Sigma}{\partial t} + \frac{\partial u_i \Sigma}{\partial x_i} = \frac{\partial}{\partial x_i}\left(\frac{\mu}{Sc}\frac{\partial(\Sigma/\bar{\rho})}{\partial x_i}\right) + (P_1 + P_2 + P_3)\Sigma - \mathrm{D} + P_k \quad (61)$$

Where:

- μ is the laminar viscosity;
- Sc is the Schmidt number;
- $P_1 = \alpha K_t$ is the flame surface production by turbulent stretch;
- $P_2 = \frac{2}{3}\frac{\partial \widetilde{u_i}}{\partial x_i}$ models the effects of the flame thermal expansion and curvature;
- $P_3 = \frac{2}{3}\bar{s}_l \frac{1-\tilde{c}}{\tilde{c}}\Sigma$ source due to dilatation of the flame;
- $D = \beta \bar{s}_l \frac{\Sigma^2}{1-\bar{c}}$ dissipation of flame area;
- $\bar{s}_l$ is the laminar flamespeed;
- $\tilde{c}$ is the mass progress variable and it is defined by:

$$\tilde{c} = 1 - \frac{\tilde{Y}_F}{\tilde{Y}_{FT}} \quad (62)$$

- $\tilde{Y}_F$ is the unburned fuel mass fraction;
- $\tilde{Y}_{FT}$ is the fuel tracer which tracks the fuel mass fraction before combustion;
- $\bar{c}$ is the volume progress variable, defined by:

$$\bar{c} = \frac{\bar{\rho}}{\rho_b}\tilde{c} \quad (63)$$

- ρ_b is the density of the burned gases;

4.4. SI-SRM (Stochastic Reactor Model for Spark-Ignition engines)

The SI-SRM is a 0D model of physical and chemical processes in SI engines [45]. The main features of the model are as follows:

- Quasi-3D consideration of the combustion chamber geometry;
- Quasi-3D turbulent flame propagation model;
- Particle-based representation of the in-cylinder mixture;
- Detailed chemistry consideration for the calculation of the heat release due to combustion emission formation and auto-ignition;
- Distinguishing between the burned and the unburned zone that result from the spherical flame propagating across the combustion chamber;
- Low computational cost;

The strength of the SRM is that it provides means to include effects of inhomogeneities and turbulence (*Figure 5*).

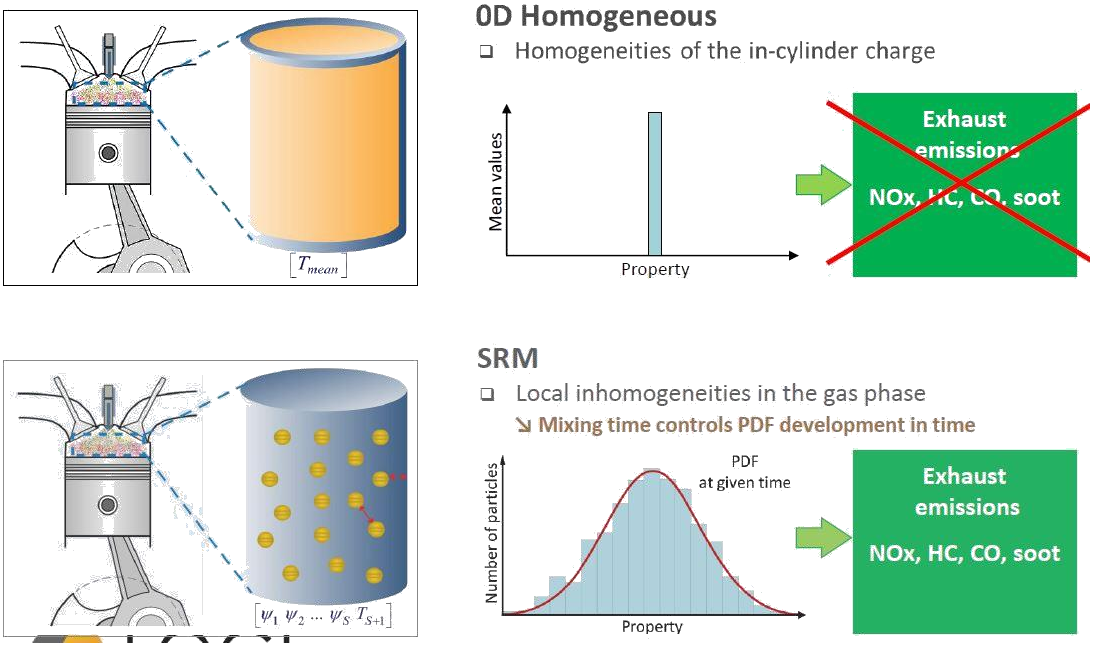

Figure 5: Concept of the SI-Stochastic Reactor Models [55]

In a real engine or in a CFD model the chemical composition, temperature and mass, have distributions in space, but in the space dimensionless SRM the distribution of the particles variables can be described with probability density functions (PDFs) [46], with one PDF for each variable (*Figure 5*). The PDF can be compared with the distributions from 3D CFD calculations or from measurements in real engines.

As said before, one of its advantage is a lower computational cost compared to the one of 3D CFD (*Figure 6*).

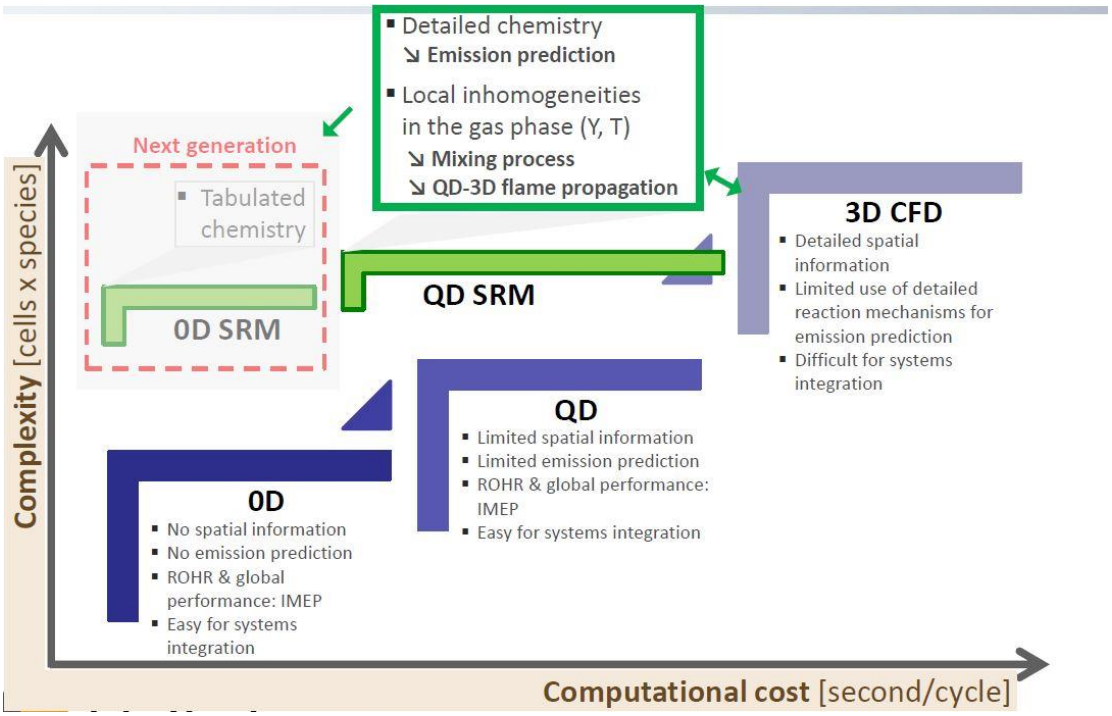

Figure 6: Aspects of internal combustion engine modelling in SRM [55]

3D CFD cold flow data are used to extrapolate the SI-SRM parameter to simulate the combustion process at different operating points.

5. Comparison of laminar flame speed results with LOREresearch and with Flame Speed Generator Tool

Following the validation of the different mechanisms, it was decided to use the LOGE mechanism that is more complex than the other two mechanism used (*Table3, chapter 4*), with the results obtained at the Polytechnic of Turin with the other two mechanisms.

Before showing the results obtained for pure fuel and for the blends that we want to investigate, it is necessary to show how these two programmes work:

- LOGEresearch (FPF) (*figure 18*):

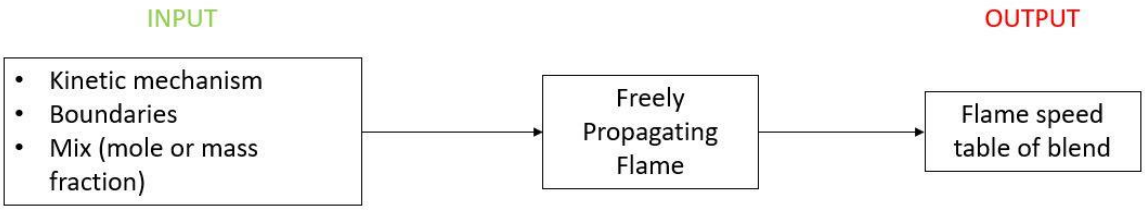

Figure 18: Simplified scheme of how LOGE research works

It has as input the mechanism used, the blend (or the pure fuel) that we want to study and the boundaries to consider (pressure, temperature, equivalence ratio, EGR). It is possible to modify also other parameter like the *transport model, the solver setting* (time steps, step size, tolerance and so on) and *the gridding settings* (grid points, discretization size).

- Flame Speed Generator Tool (FSG) (*figure 19*):

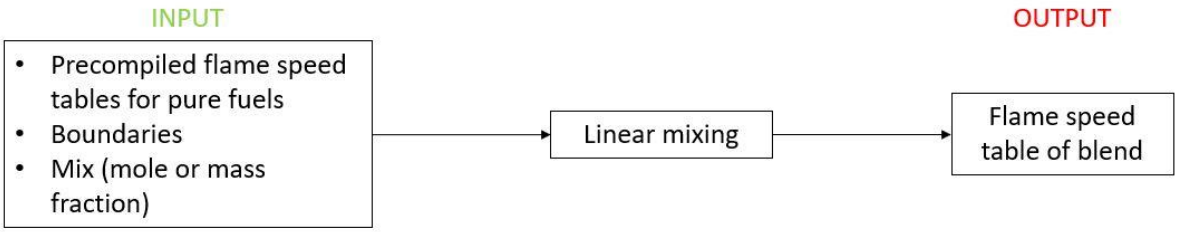

Figure 19: Simplified scheme of how Flame Speed Generator works

It has as input the Flame Speed Table for each component, and a txt file in which to enter the blend (mass or mole fraction) and the boundaries. It compiles the Flame speed tables

based on precompiled flame speed tables for pure components obtained with LOGEresearch using the LOGEfuel Natural Gas reaction scheme v2.0. The main difference is that the first method creates the surrogate first and then calculates its flame speed table; the second methods creates first the flame speed table for each pure fuel and uses linear mixing to obtain the flame speed table for a surrogate. Another difference concerns the time they take to create the Flame Speed Table, because with Flame Speed Generator it is much faster than LOGE research.

For that reason, we want to compare the results obtained with both the programmes.

5.1. Boundaries

In the next table (*Table 4*) the boundaries used for both software are summarized.

	Range	Steps
Temperature	300-1200K	50 K
Pressure	1- 200 bar	Variable
Equivalence Ratio	0.5-1.5	0.1
EGR	0-30%	10%

Table 4: Boundaries considered in LOGE research and in Flame Speed Generator Tool

The boundaries chosen for both software are the same in order to obtain comparable results.

5.2. Pure fuels

5.2.1. Laminar Flame speed vs Temperature

Observing the equation (24), it is possible to see that Laminar Flame Speed is related to the temperature by an exponential correlation, so it means that the higher the temperature, the greater the increase of the laminar flame speed is.

- Methane (CH_4) (*Figure 20);*

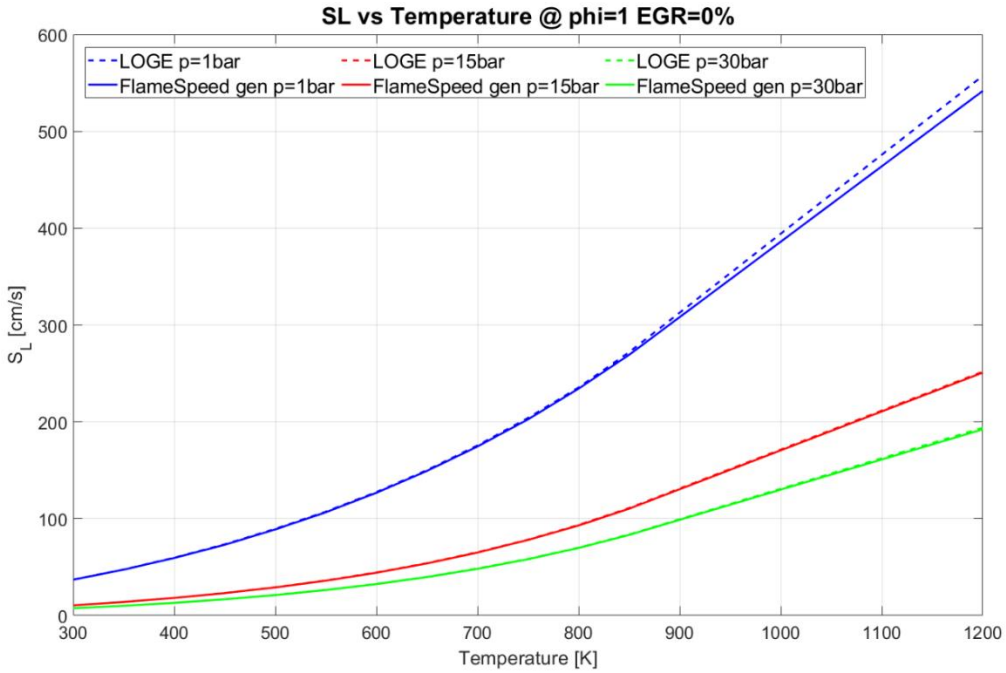

Figure 20: Comparison results of LOGE mechanism and of Flame Speed generator for methane in function of Temperature @ p=1bar,15bar,30bar EGR=0% and phi=1

- Ethane (C_2H_6) (*Figure 21 in Appendix);*

- Propane (C_3H_8) (*Figure 22 in Appendix*);

- Iso-Butane (I-C_4H_{10}) (Figure 23*);*

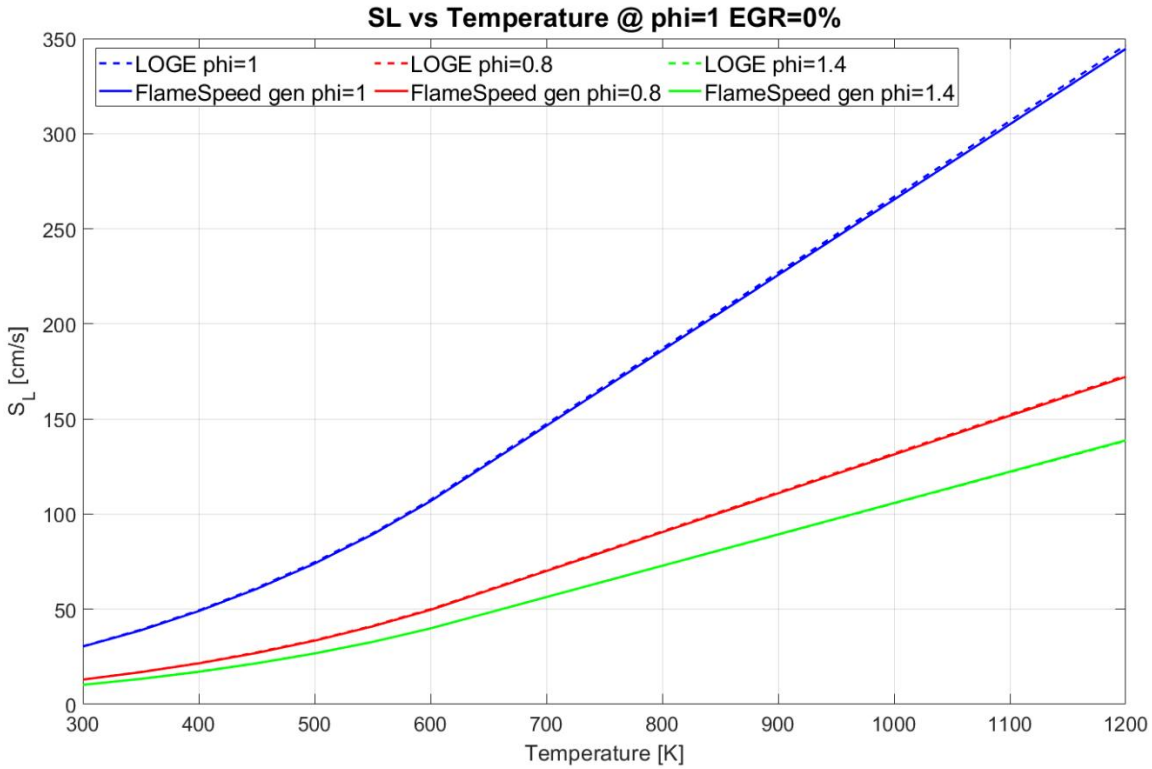

Figure 23: Comparison results of LOGE mechanism and of Flame Speed generator for iso-butane in function of Temperature @ p=1bar,15bar,30bar EGR=0% and phi=1

- Hydrogen (H_2)

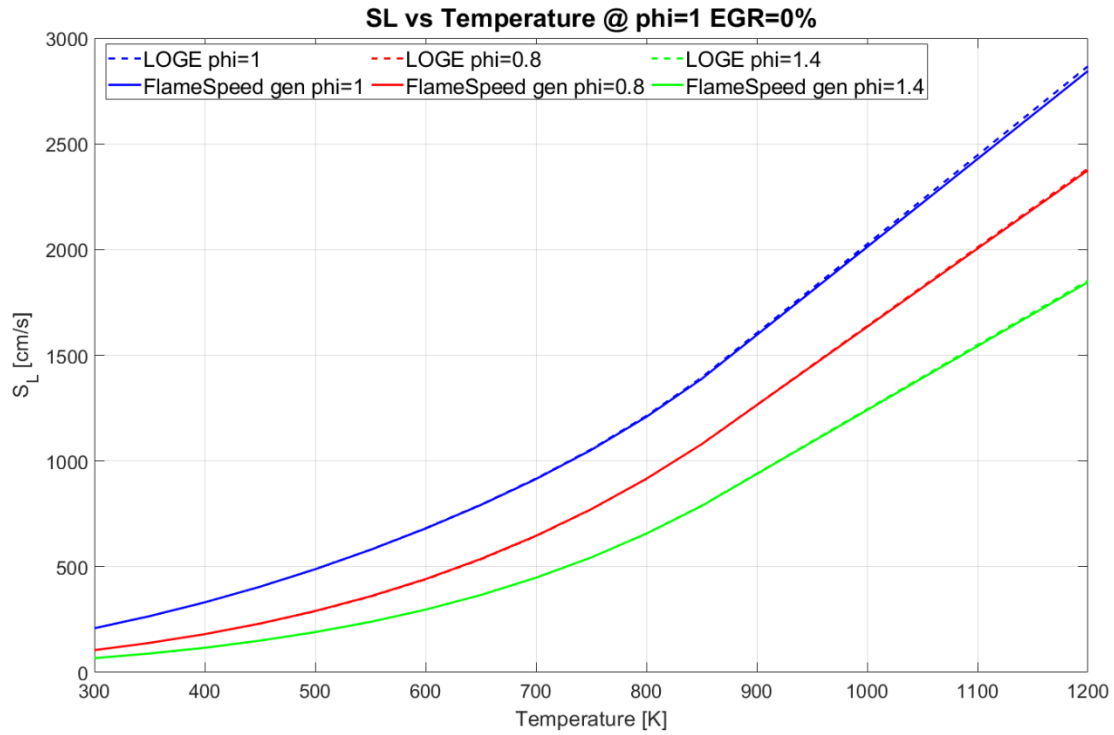

Figure 24: Comparison results of LOGE mechanism and of Flame Speed generator for hydrogen in function of Temperature @ p=1bar,15bar,30bar EGR=0% and phi=1

5.2.2. Laminar Flame speed vs Equivalence Ratio

According to the equation (23), the equivalence ratio has an impact on the laminar flame speed. Here an equivalence ratio range between 0.5 and 1.5 has been considered. For all the fuels considered, and for all the pressure conditions, the peak of the laminar flame speed is obtained for slightly rich blends (phi = 1.1). Here, it has been considered three different values of pressure.

- Methane (CH_4) (*Figure 25);*

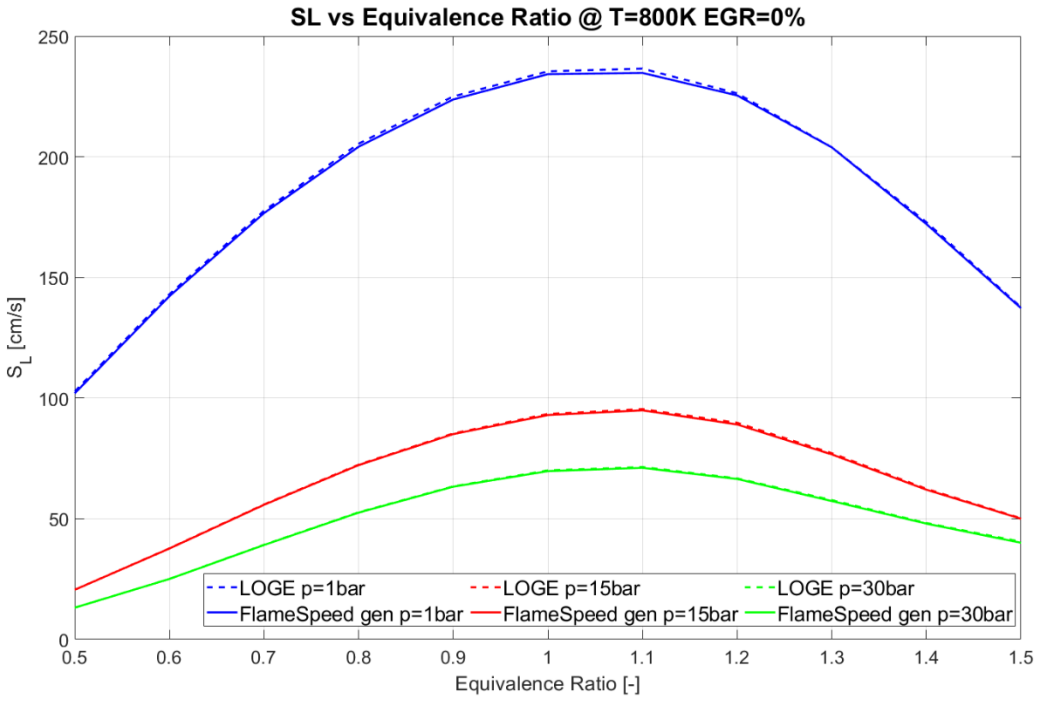

Figure 25: Comparison results of LOGE mechanism and of Flame Speed generator for methane in function of Equivalence Ratio @ p=1bar,15bar,30bar EGR=0% and T=800K

- Ethane (C_2H_6) (*Figure 26 in Appendix);*

- Propane (C_3H_8) (*Figure 27 in Appendix*);

- Iso-Butane (I-C_4H_{10}) (*Figure 28);*

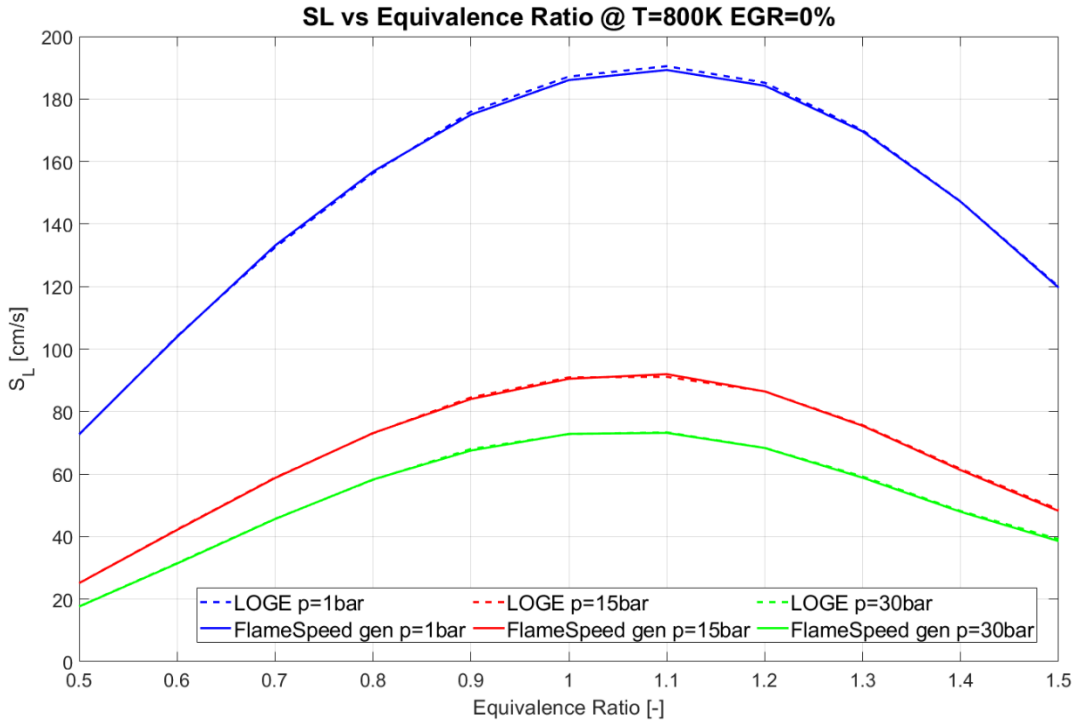

Figure 28: Comparison results of LOGE mechanism and of Flame Speed generator for iso-butane in function of Equivalence Ratio @ p=1bar,15bar,30bar EGR=0% and T=800K

- Hydrogen (H_2) (*Figure 29);*

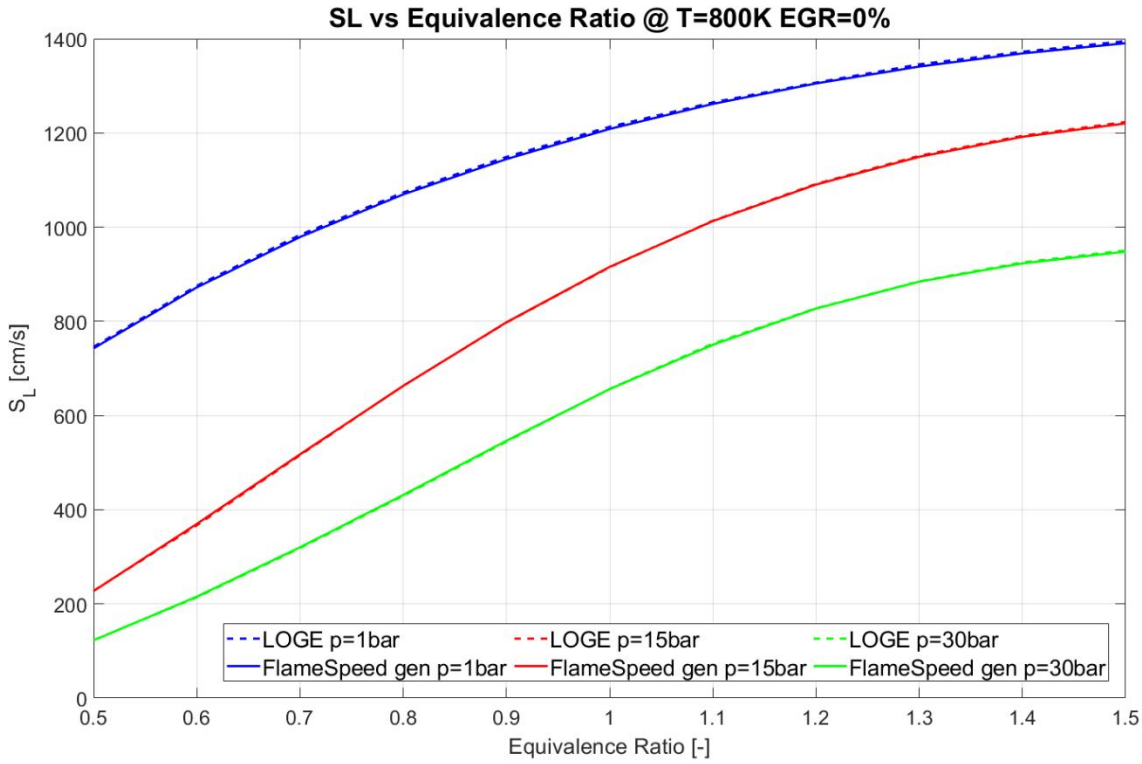

Figure 29: Comparison results of LOGE mechanism and of Flame Speed generator for hydrogen in function of Equivalence Ratio @ p=1bar,15bar,30bar EGR=0% and T=800K

5.2.3. Laminar Flame speed vs Pressure

In this section the influence of pressure on laminar flame speed was analysed and different values of Equivalence Ratio have been considered to study the behaviour of the fuel also at lean and rich conditions. It is possible to note that a higher pressure leads to a reduction of the laminar flame speed, and a downward translation of the curves.

- Methane (CH_4) (*Figure 30*);

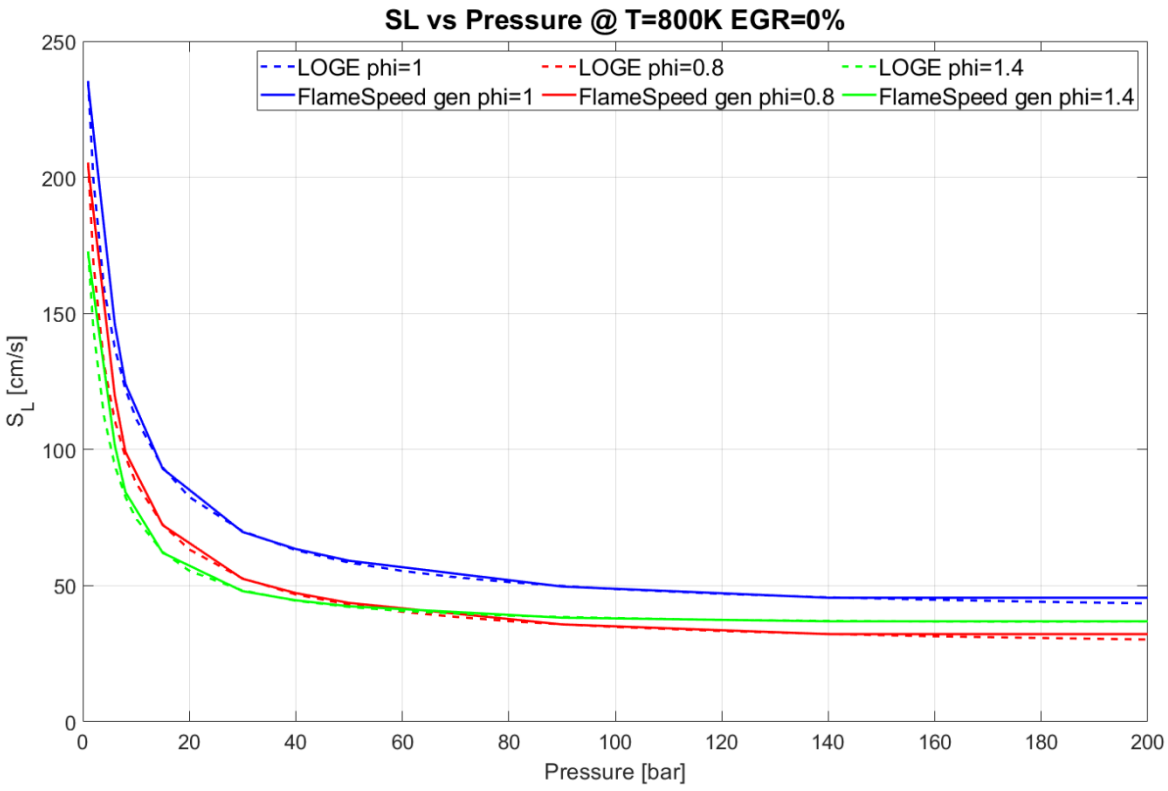

Figure 30: Comparison results of LOGE mechanism and of Flame Speed generator for methane in function of Pressure @ phi=1,0.8,1.4, EGR=0% and T=800K

- Ethane (C_2H_6) (*Figure 31 in Appendix*);

- Propane (C_3H_8) (*Figure 32 in Appendix*);

- Iso-Butane (I-C_4H_{10}) (*Figure 33*);

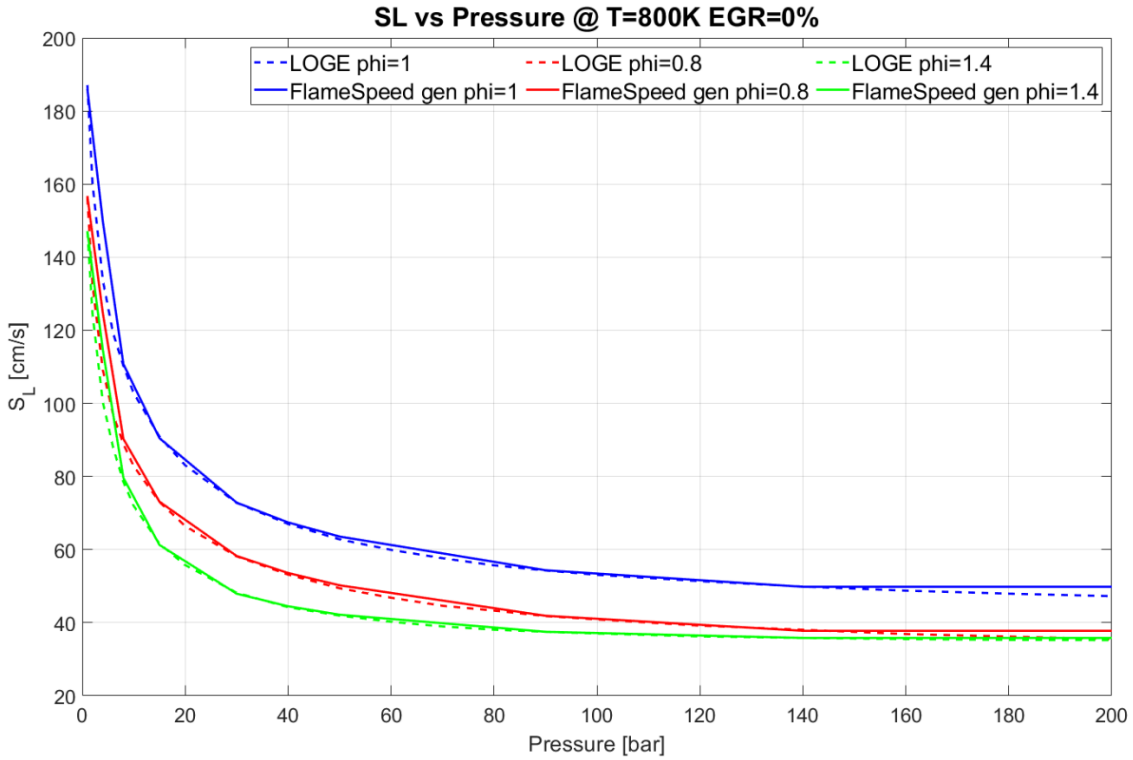

Figure 33: Comparison results of LOGE mechanism and of Flame Speed generator for iso-butane in function of Pressure @ phi=1,0.8,1.4, EGR=0% and T=800K

- Hydrogen (H_2) (*Figure 34*);

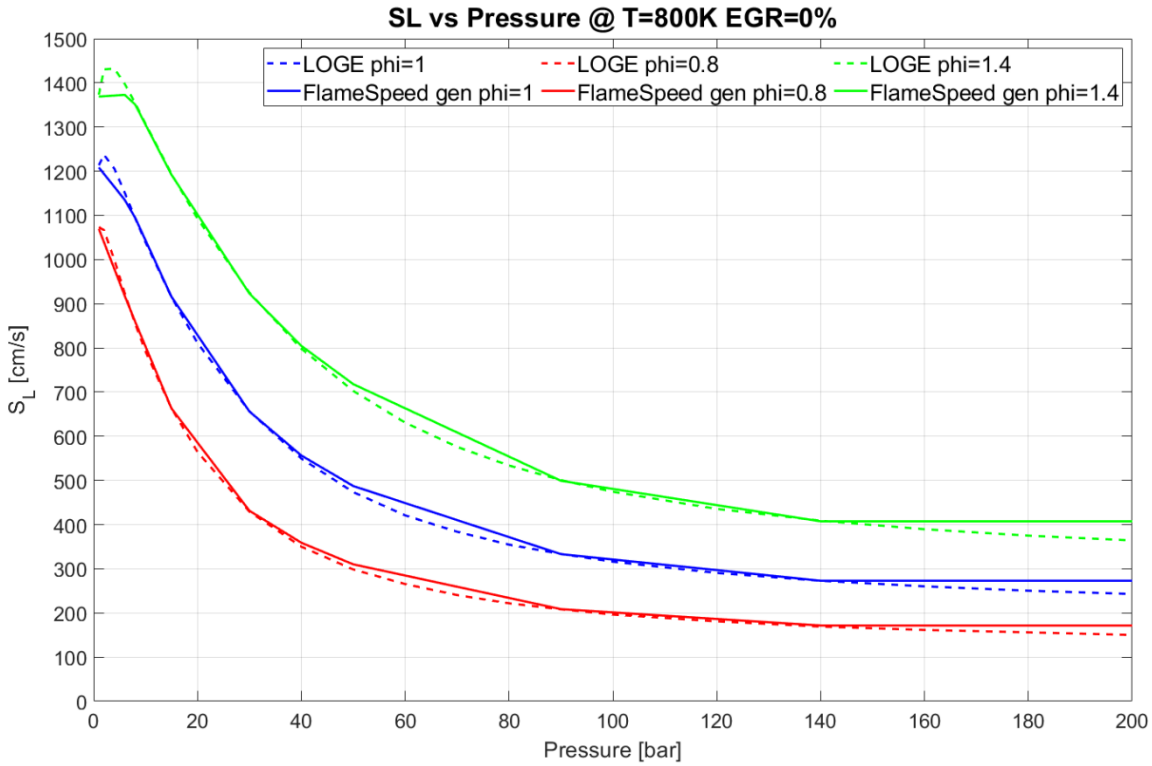

Figure 33: Comparison results of LOGE mechanism and of Flame Speed generator for hydrogen in function of Pressure @ phi=1,0.8,1.4, EGR=0% and T=800K

5.2.4. Laminar Flame speed vs EGR

In this section the effect of the dilution on laminar flame speed was discussed. An assumption was made about the EGR composition and a simplified EGR with only N_2 was used; CO_2, H_2O were neglected because they have a much slower burning velocity than NO_2. The addiction of EGR makes the charge less reactive and during the combustion it will be reached lower pressure, temperature and a lower flame propagation. That is happened because the laminar flame speed is related to EGR with an exponential correlation and, with high level of dilution, the curves tend to converge at the same point.

- Methane (CH_4) (*Figure 35);*

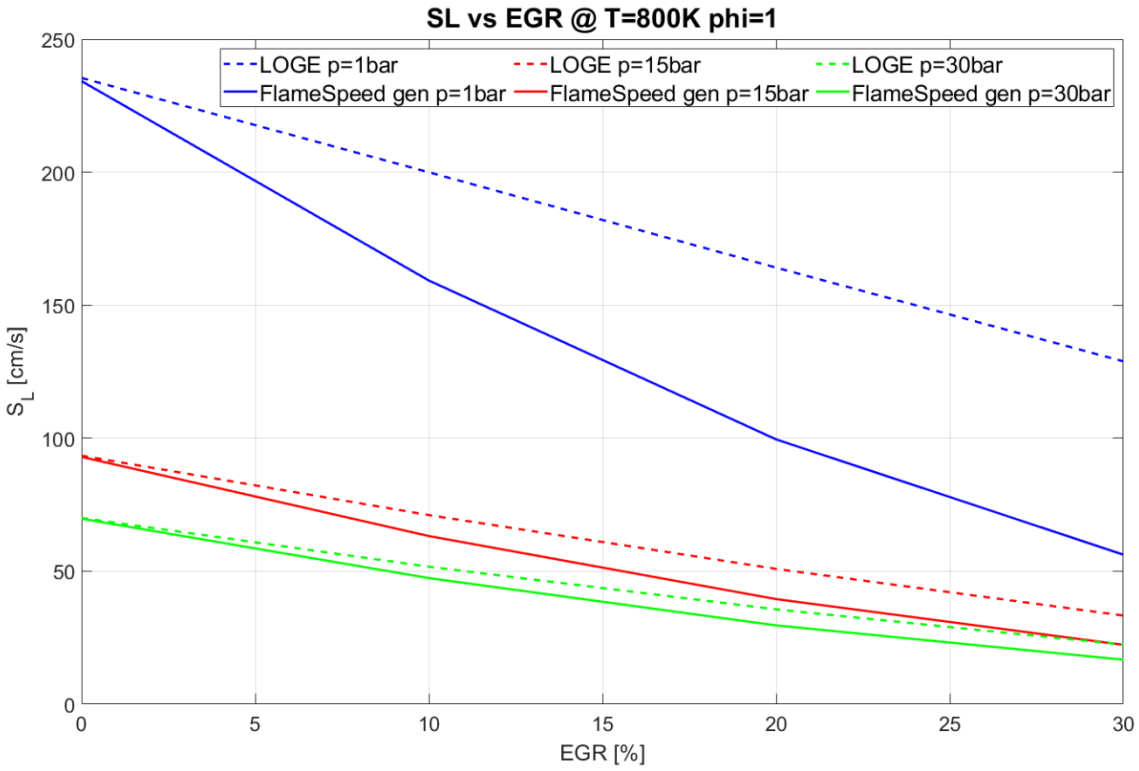

Figure 35: Comparison results of LOGE mechanism and of Flame Speed generator for methane in function of EGR @ p=1,15,30bar, phi=1 and T=800K

- Ethane (C_2H_6) (*Figure 36 in Appendix);*

- Propane (C_3H_8) *(Figure 37 in Appendix*);

- Iso-Butane (I-C_4H_{10}) (*Figure 38);*

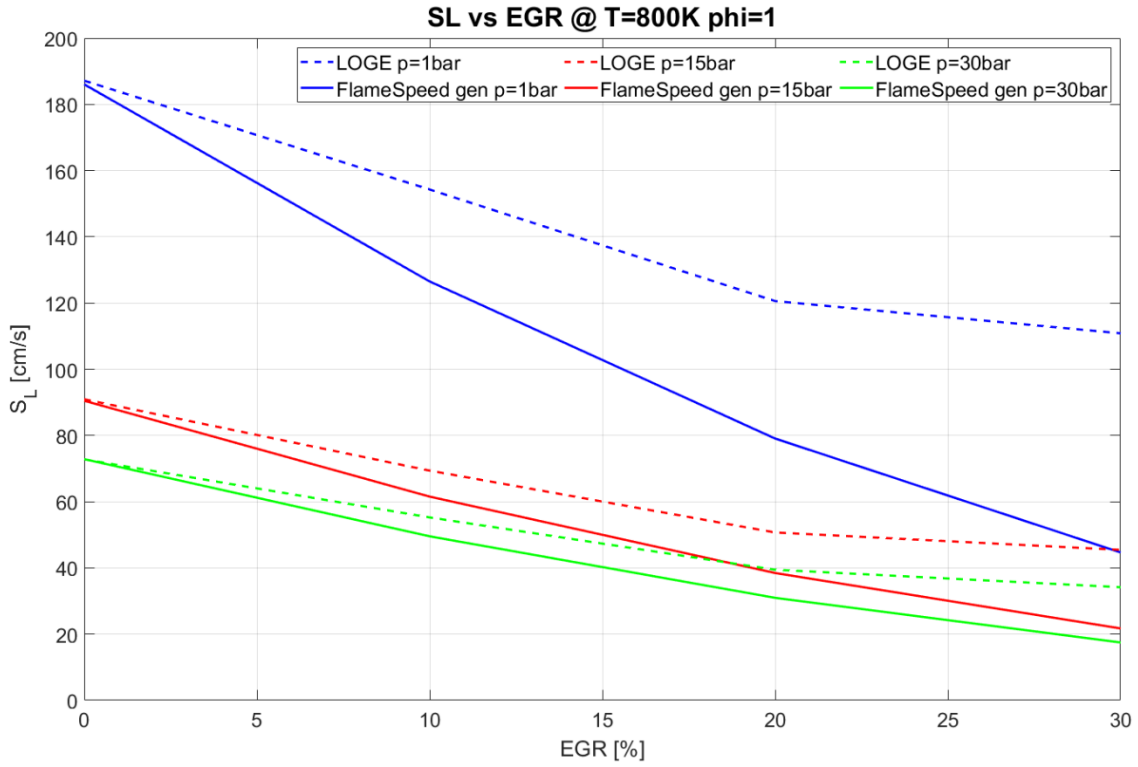

Figure 38: Comparison results of LOGE mechanism and of Flame Speed generator for iso-butane in function of EGR @ p=1,15,30bar, phi=1 and T=800K

- Hydrogen (H_2) (*Figure 39);*

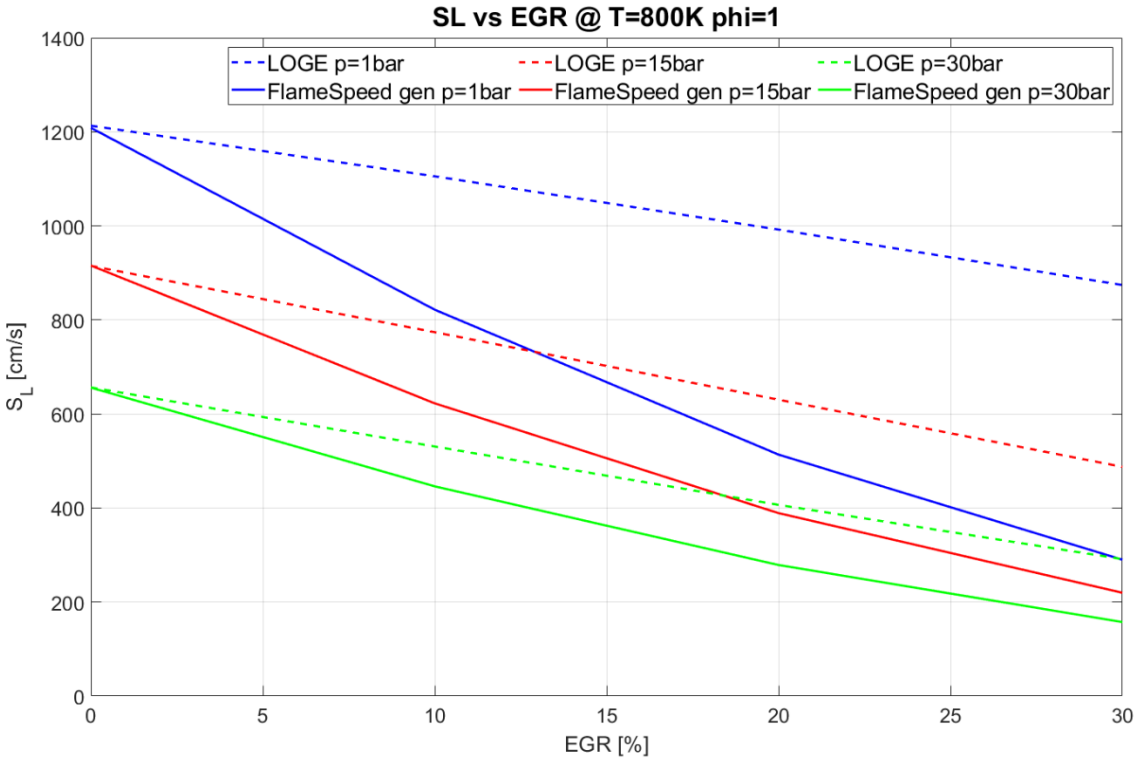

Figure 39: Comparison results of LOGE mechanism and of Flame Speed generator for hydrogen in function of EGR @ p=1,15,30bar, phi=1 and T=800K

5.3. Blends

Once the comparison between pure fuels has been made, it is possible to make the same also for the blends that we want to study:

- NG: 94,4% CH_4 + 4,7% C_2H_6 + 0,9% C_3H_8
- HCNG15: 85% CH_4 + 15% H_2
- HCNG25: 75% CH_4 + 25% H_2
- 8713: 87% CH_4 + 13% C_2H_6
- Mix I-C4H10: 94,2% CH_4 + 4,7% C_2H_6 + 0,82% I-C_4H_{10}

In this case, the results obtained will also be compared with the results obtained at the Polytechnic of Turin thanks to the aid of DARS and the first for blends were obtained with GRI mechanism v3.0 and the last one with USC_II mechanism.

5.3.1. Laminar Flame speed vs Temperature

In the following figures (40, 41, 42, 43, 44) the trends of the flame speed as a function of temperature are shown:

- NG

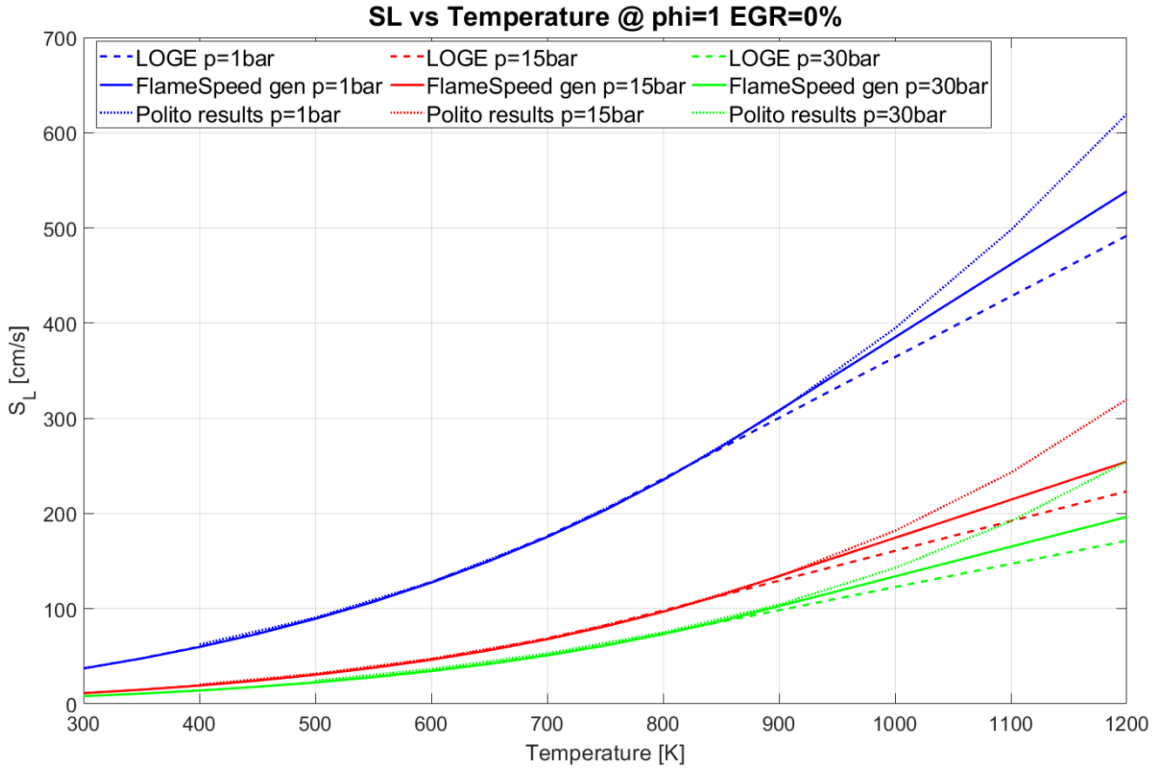

Figure 40: Comparison results of LOGE mechanism, of Flame Speed generator and of Polytechnic for NG in function of Temperature @ p=1bar,15bar,30bar EGR=0% and phi=1

- HCNG15

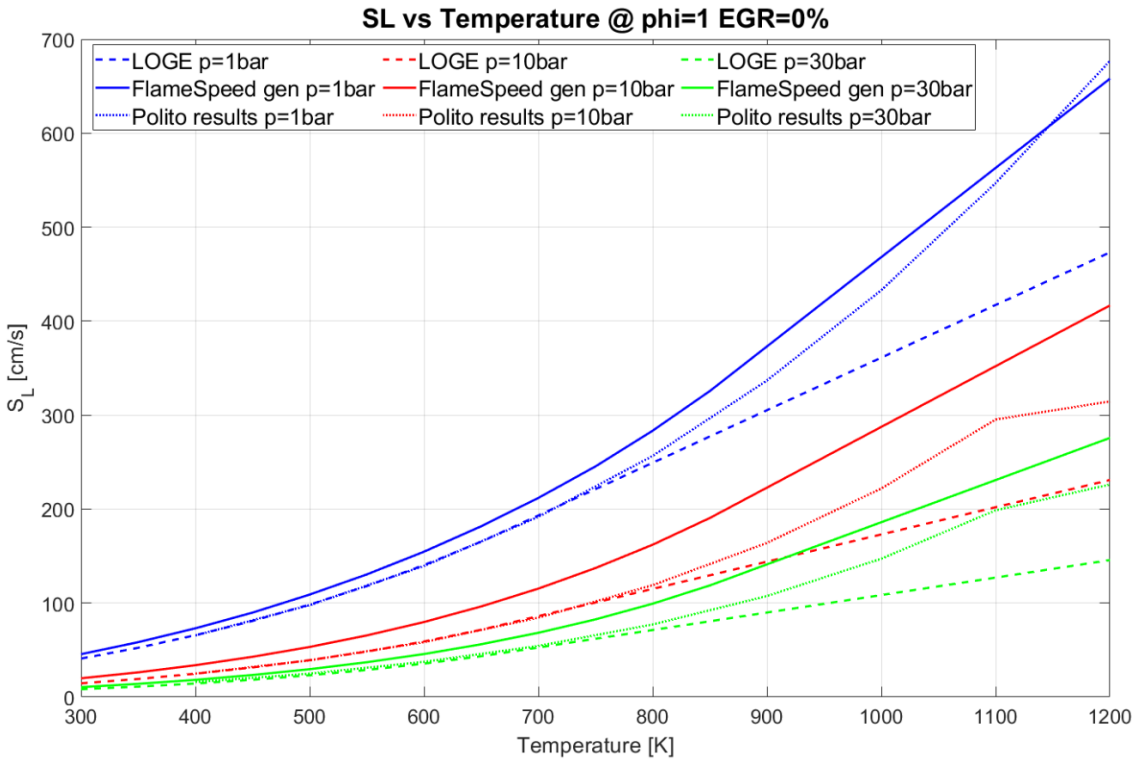

Figure 41: Comparison results of LOGE, of Flame Speed generator and of Polytechnic for HCNG15 in function of Temperature @ p=1bar,10bar,30bar EGR=0% and phi=1

- HCNG25

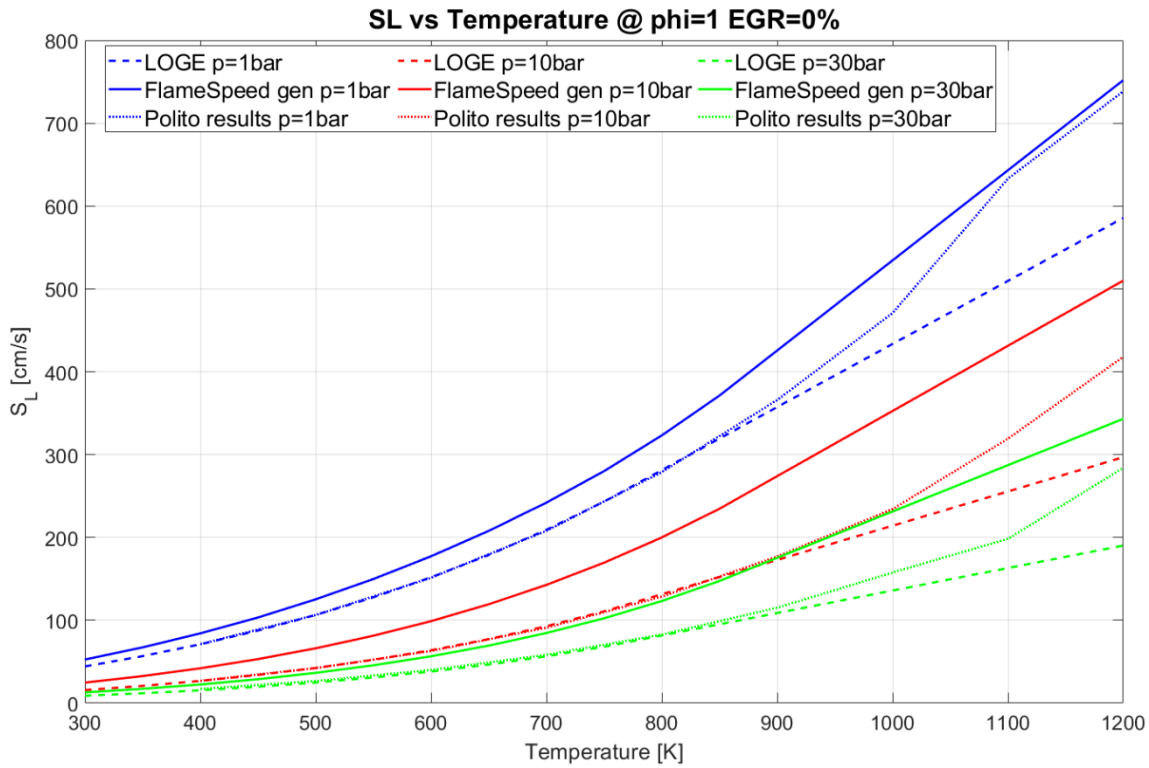

Figure 42: Comparison results of LOGE mechanism, of Flame Speed generator and of Polytechnic for HCNG25 in function of Temperature @ p=1bar,10bar,30bar EGR=0% and phi=1

- 8713

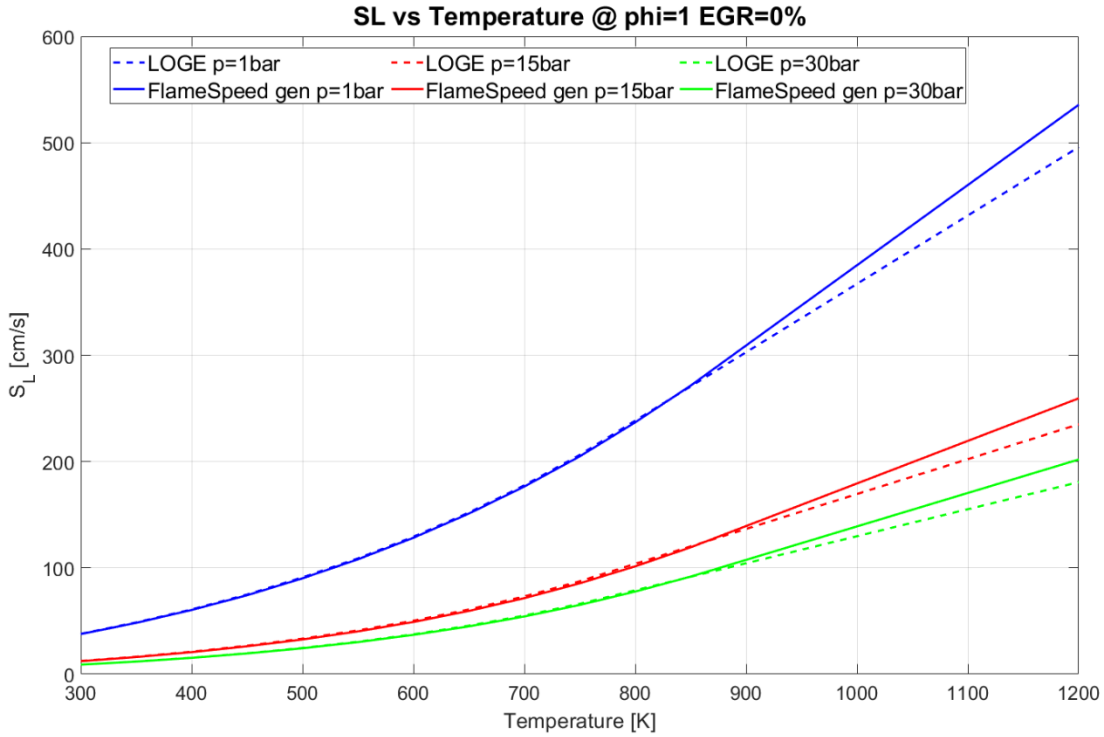

Figure 43: Comparison results of LOGE mechanism, of Flame Speed generator and of Polytechnic for 8713 in function of Temperature @ p=1bar,15bar,30bar EGR=0% and phi=1

- Mix I-C4H10

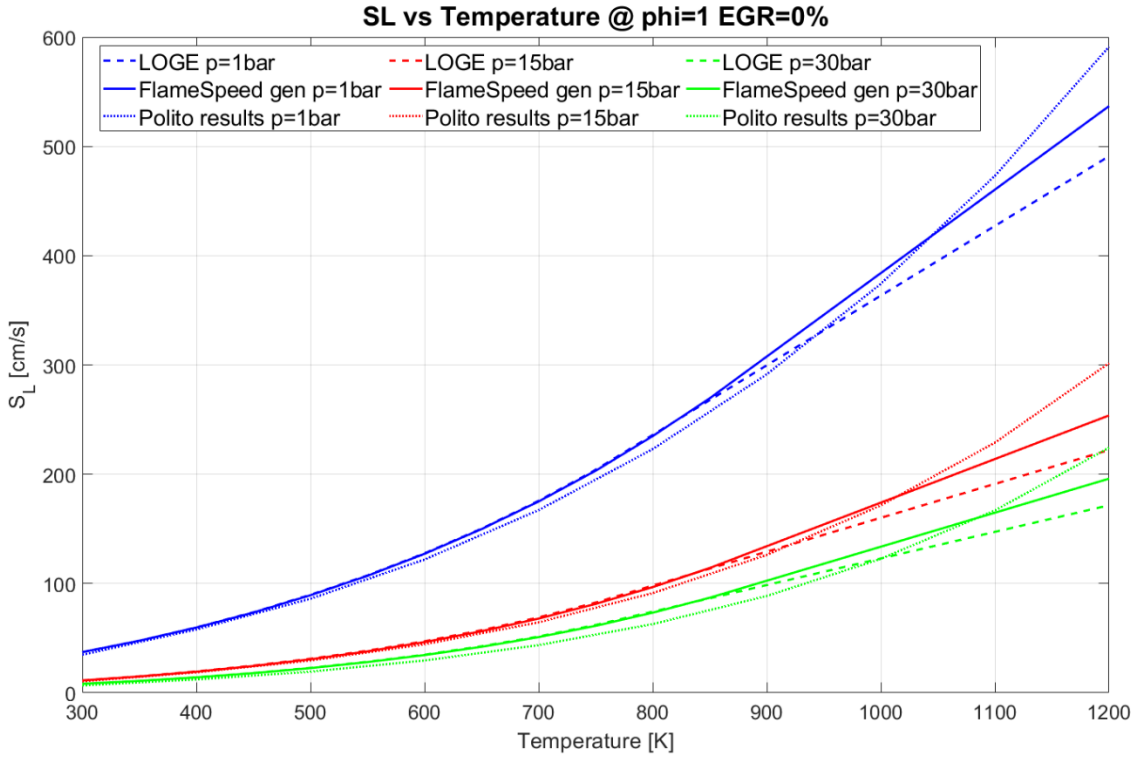

Figure 44: Comparison results of LOGE mechanism, of Flame Speed generator and of Polytechnic for Mix I-C4H10 in function of Temperature @ p=1bar,15bar,30bar EGR=0% and phi=1

5.3.2. Laminar Flame speed vs Equivalence Ratio

In the following figures (45, 46, 47, 48, 49) the trends of the flame speed as a function of Equivalence Ratio are shown:

- NG

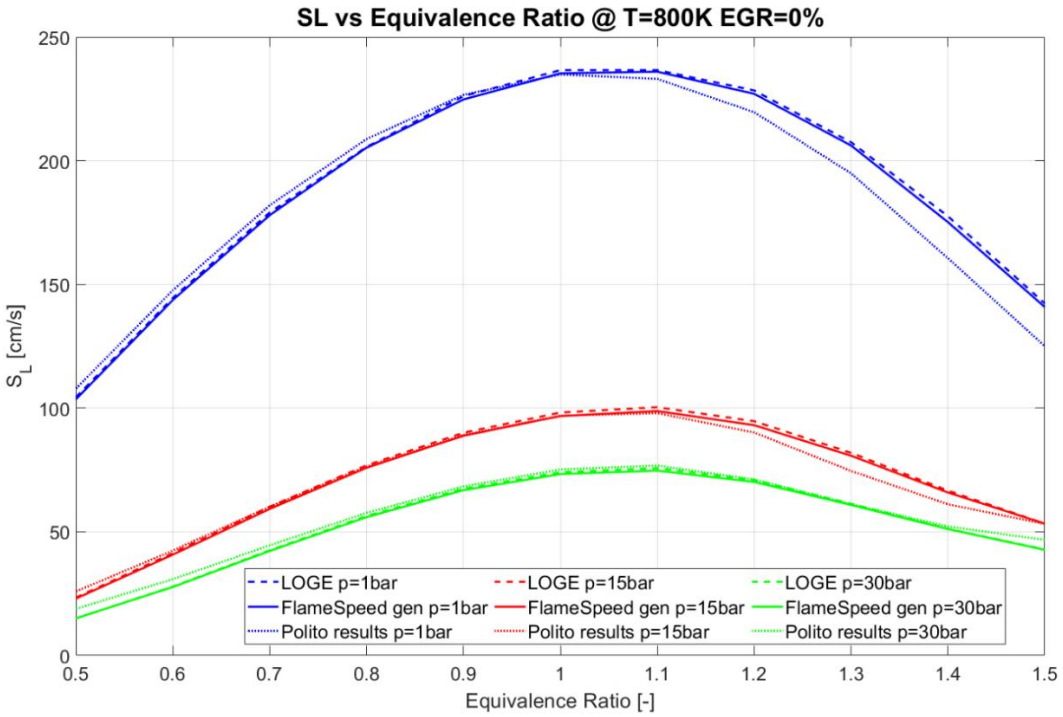

Figure 45: Comparison results of LOGE mechanism, of Flame Speed generator and of Polytechnic for NG in function of Equivalence Ratio @ p=1bar,15bar,30bar EGR=0% and T=800K

- HCNG15

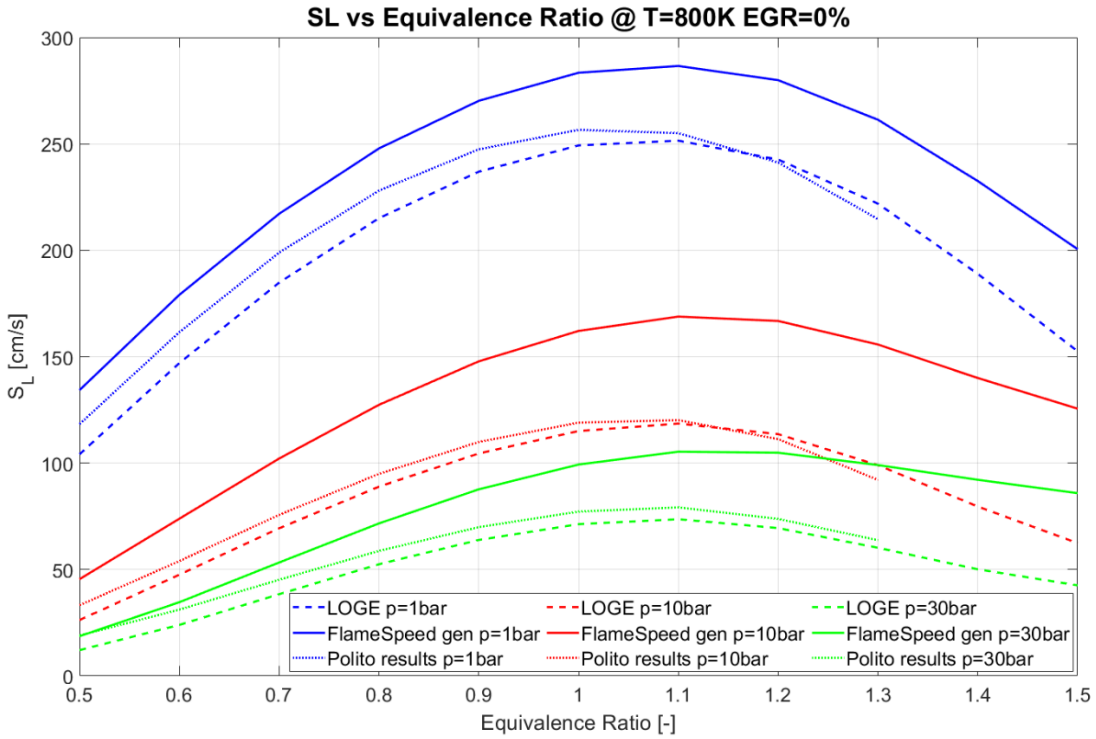

Figure 46: Comparison results of LOGE mechanism, of Flame Speed generator and of Polytechnic for HCNG15 in function of Equivalence Ratio @ p=1bar,10bar,30bar EGR=0% and T=800K

- HCNG25

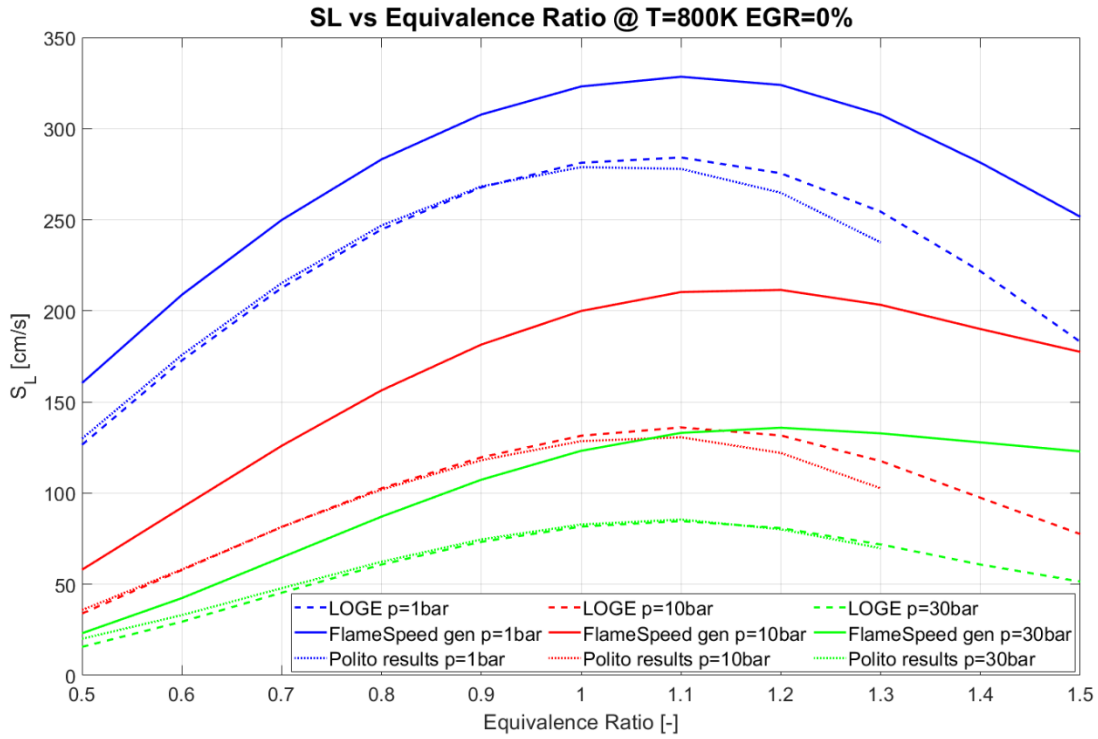

Figure 47: Comparison results of LOGE mechanism, of Flame Speed generator and of Polytechnic for HCNG25 in function of Equivalence Ratio @ p=1bar,10bar,30bar EGR=0% and T=800K

- 8713

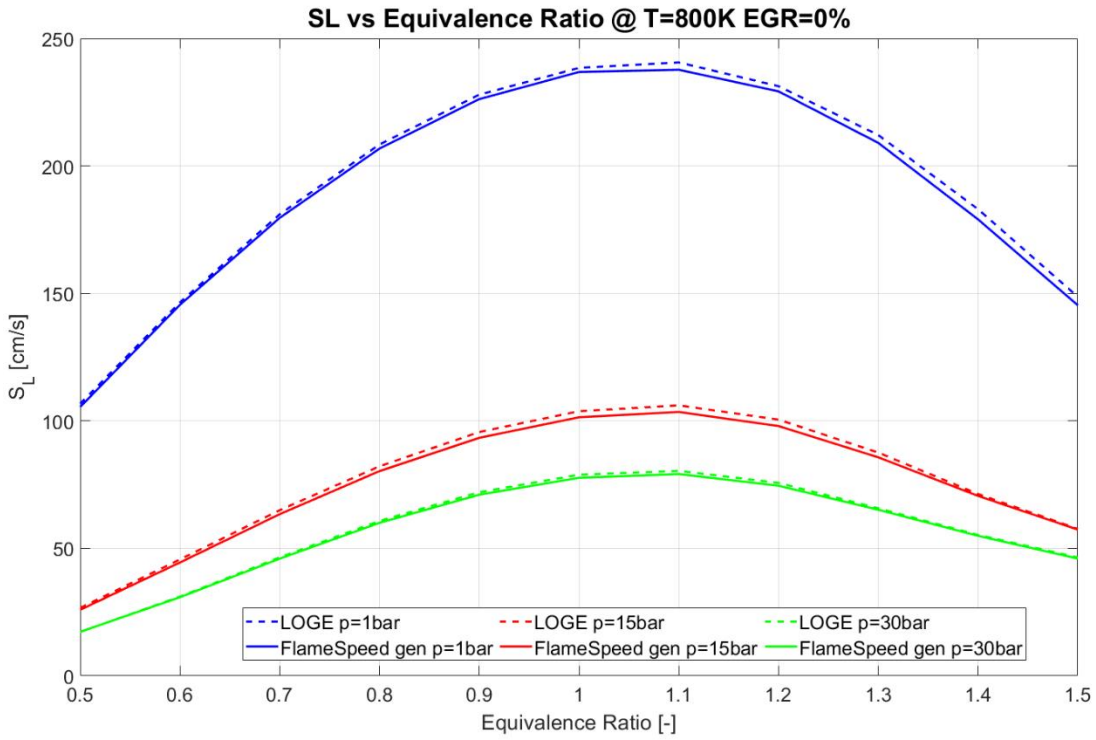

Figure 48: Comparison results of LOGE mechanism, of Flame Speed generator and of Polytechnic for 8713 in function of Equivalence Ratio @ p=1bar,15bar,30bar EGR=0% and T=800K

- Mix I-C4H10

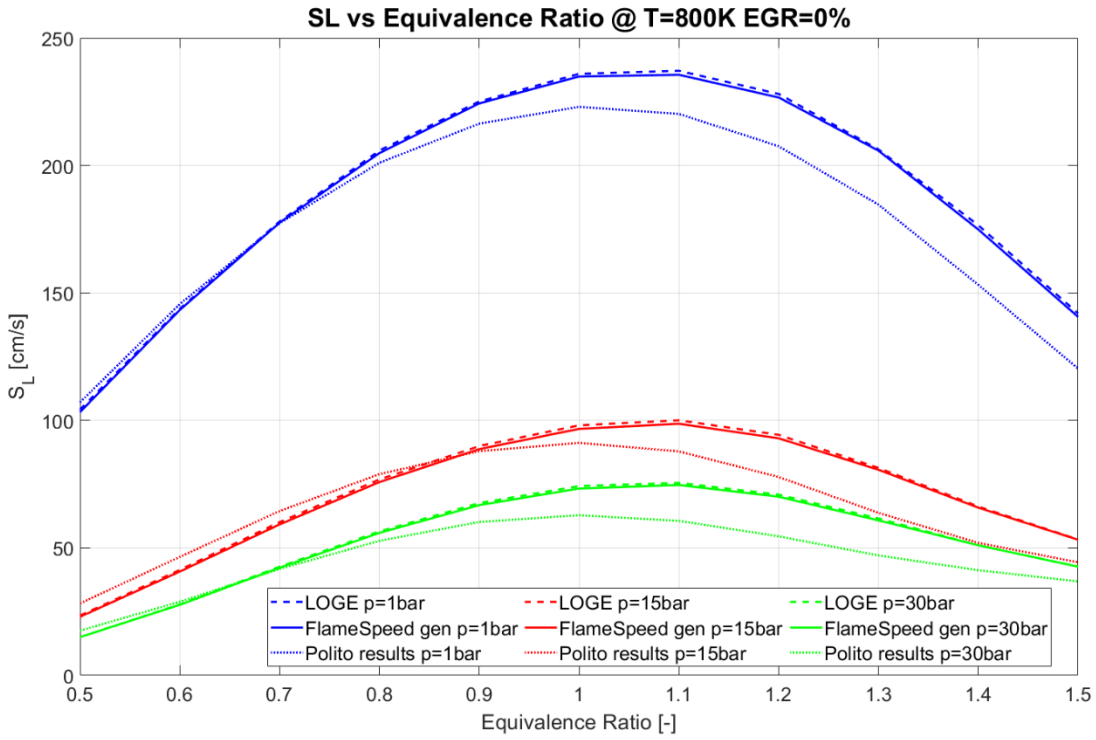

Figure 49: Comparison results of LOGE mechanism, of Flame Speed generator and of Polytechnic for Mix I-C4H10 in function of Equivalence Ratio @ p=1bar,15bar,30bar EGR=0% and T=800K

5.3.3. Laminar Flame speed vs Pressure

In the following figures (50, 51, 52, 53, 54) the trends of the flame speed as a function of Pressure are shown:

- NG

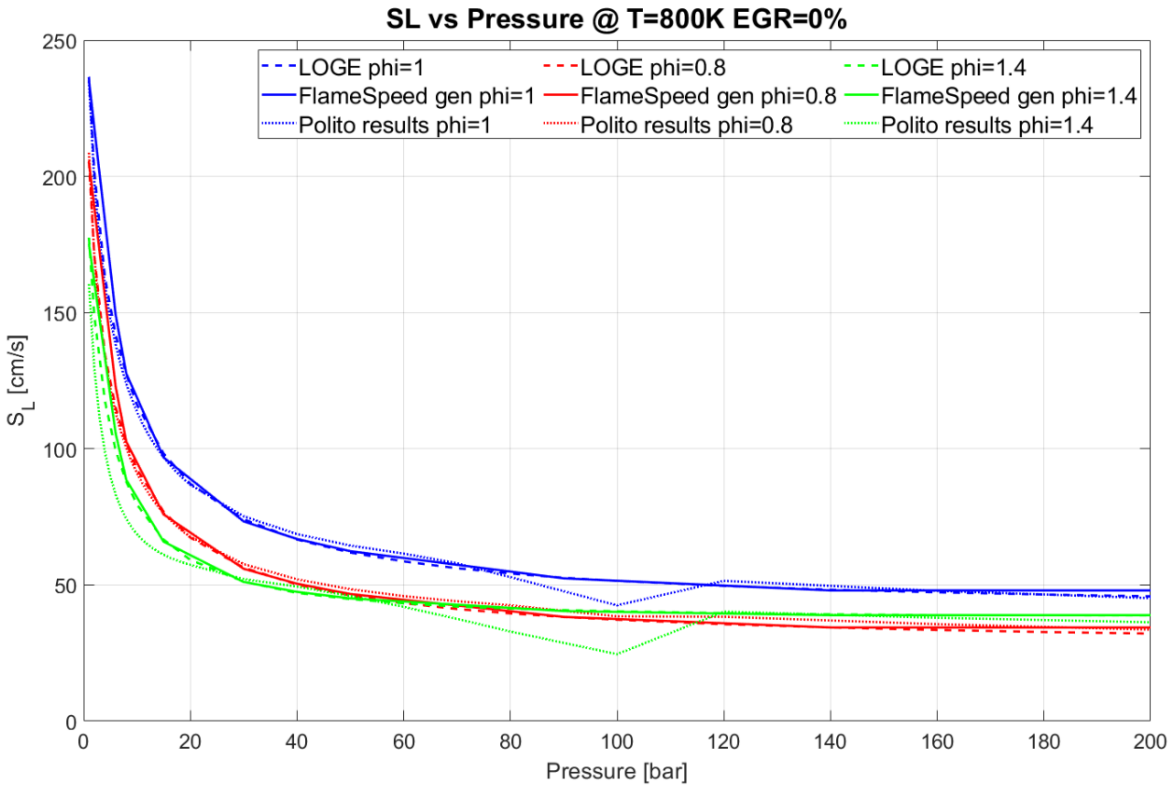

Figure 40: Comparison results of LOGE mechanism, of Flame Speed generator and of Polytechnic for NG in function of Pressure @ phi=1,0.8,1.4 EGR=0% and T=800K

- HCNG15

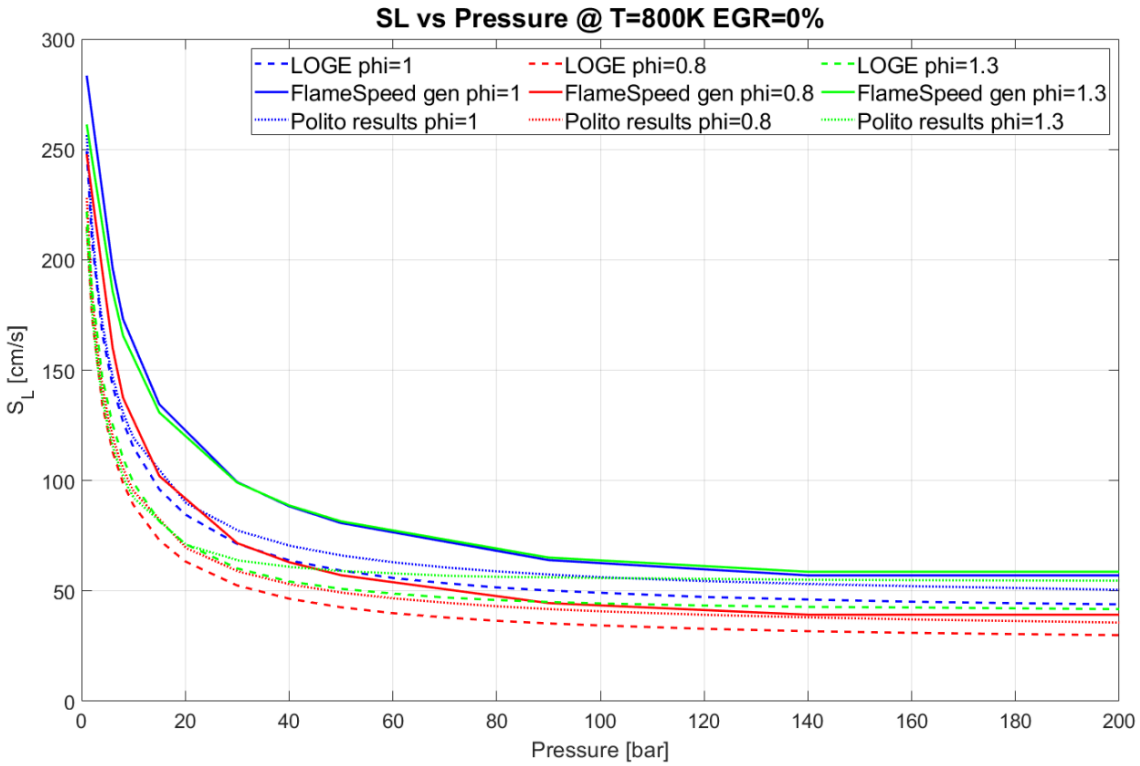

Figure 51: Comparison results of LOGE mechanism, of Flame Speed generator and of Polytechnic for HCNG15 in function of Pressure @ phi=1,0.8,1.3 EGR=0% and T=800K

- HCNG25

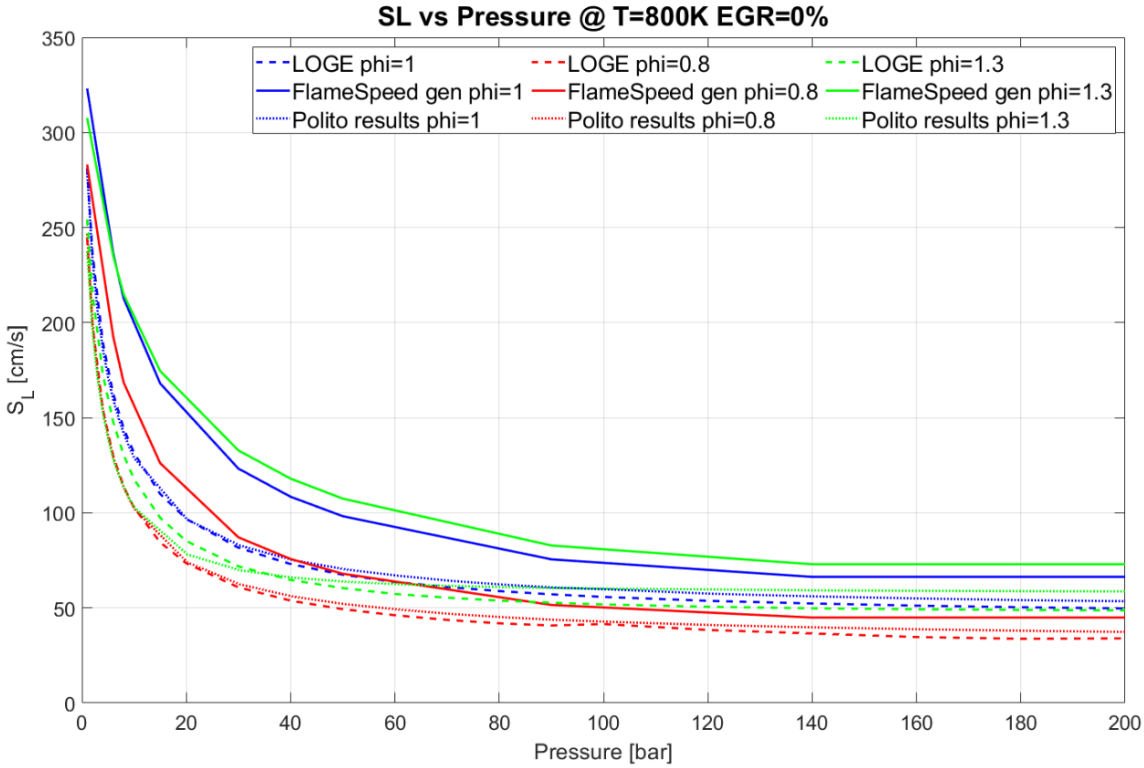

Figure 52: Comparison results of LOGE mechanism, of Flame Speed generator and of Polytechnic for HCNG25 in function of Pressure @ phi=1,0.8,1.3 EGR=0% and T=800K

- 8713

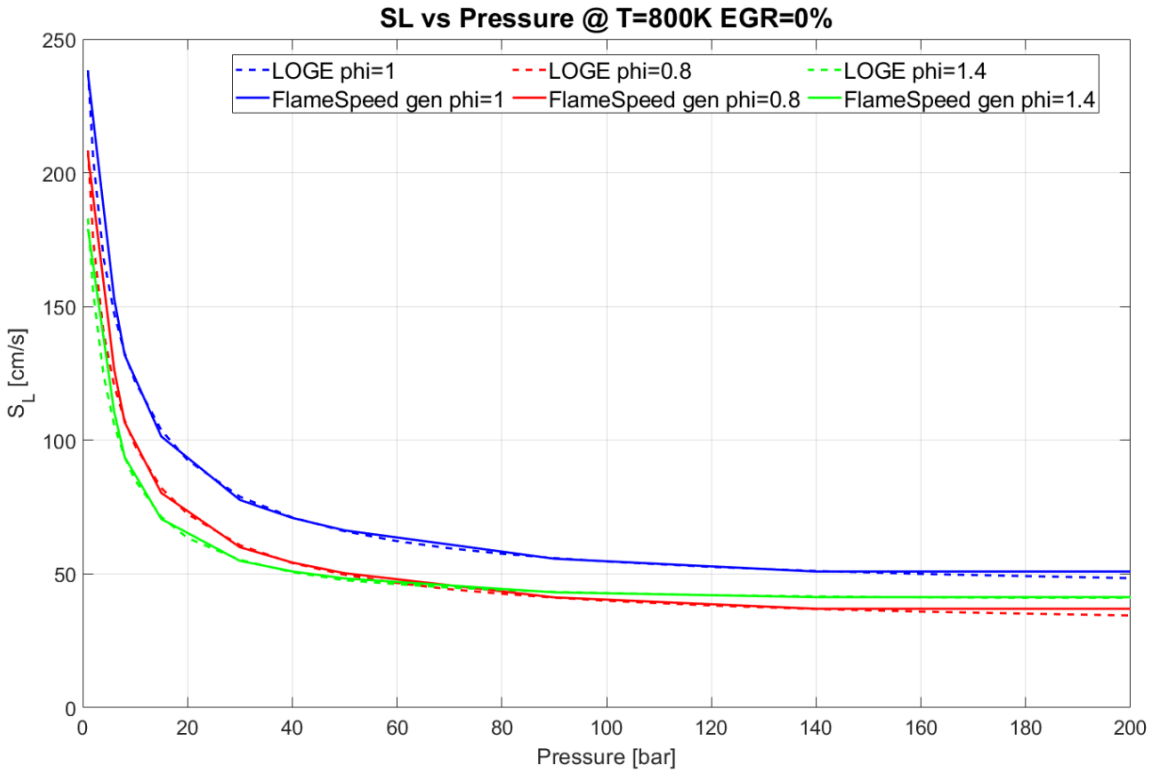

Figure 53: Comparison results of LOGE mechanism and of Flame Speed generator for 8713 in function of Pressure @ phi=1,0.8,1.4 EGR=0% and T=800K

- Mix I-C4H10

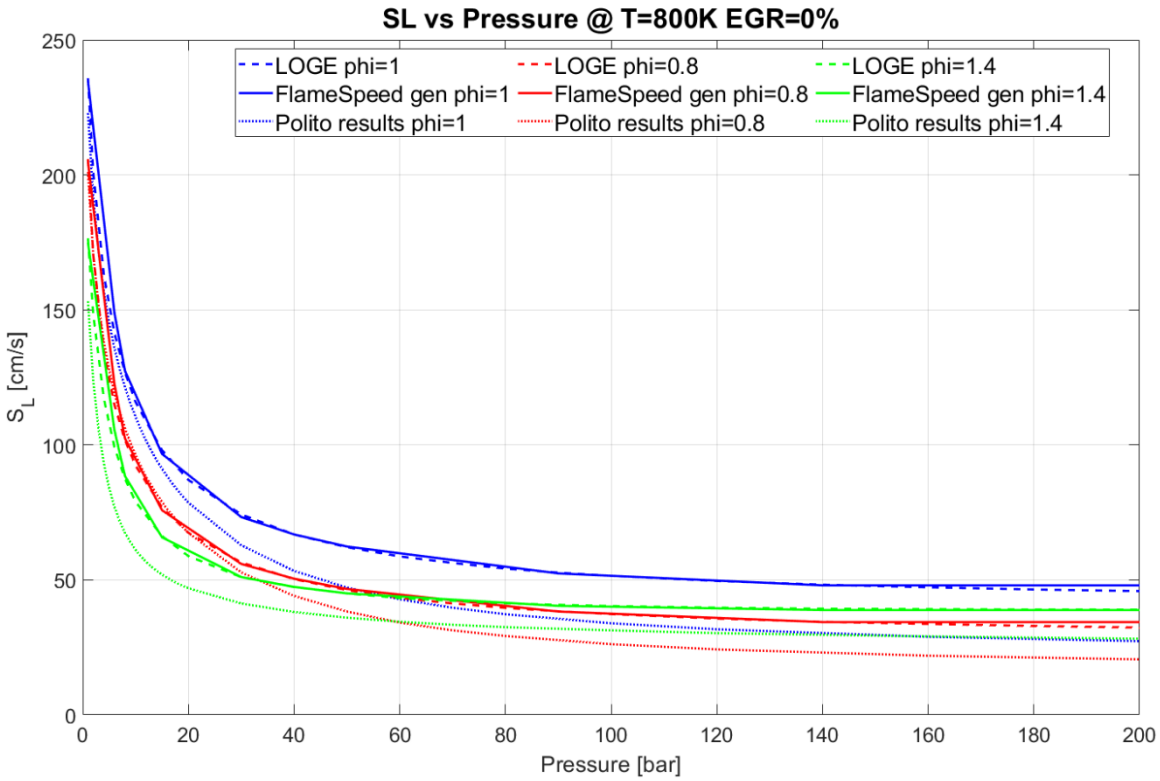

Figure 54: Comparison results of LOGE mechanism, of Flame Speed generator and of Polytechnic for Mix I-C4H10 in function of Pressure @ phi=1,0.8,1.4 EGR=0% and T=800K

5.3.4. Laminar Flame speed vs EGR

In the following figures (55, 56, 57, 58, 59) the trends of the flame speed as a function of EGR are shown:

- NG

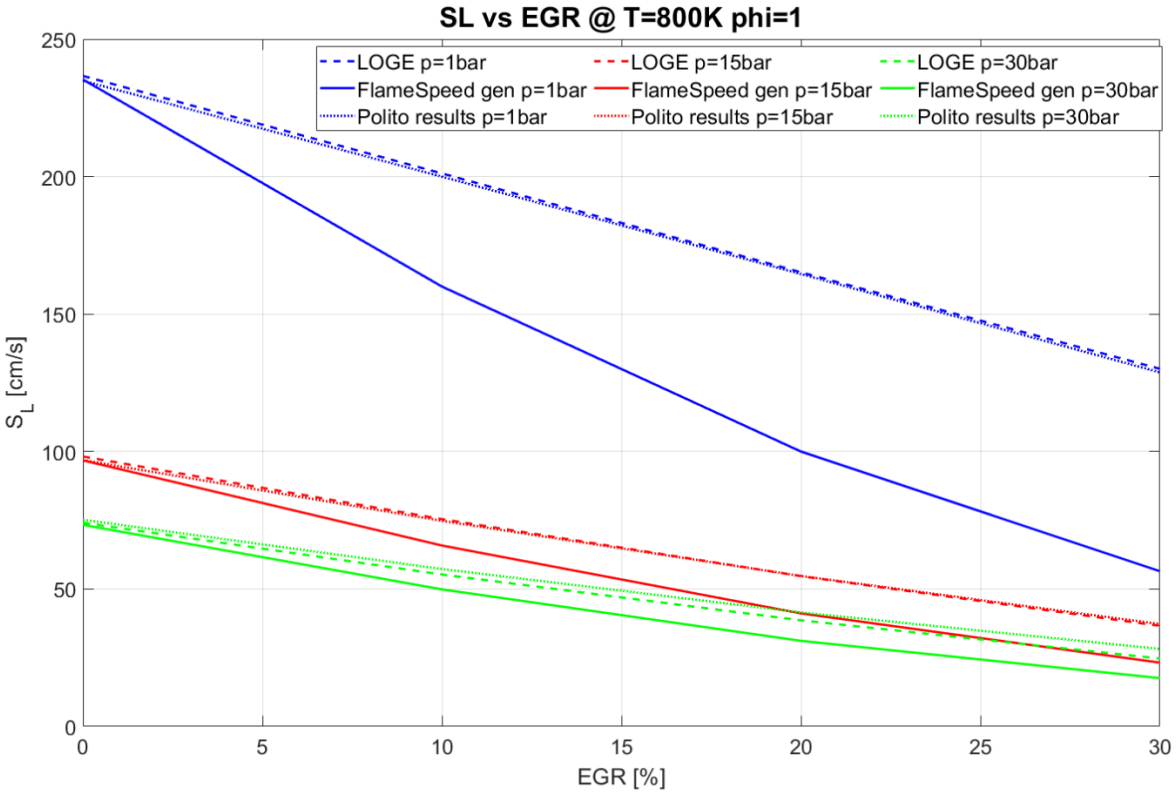

Figure 55: Comparison results of LOGE mechanism, of Flame Speed generator and of Polytechnic for NG in function of EGR @ p=1,15,30bar, phi=1 and T=800K

- HCNG15

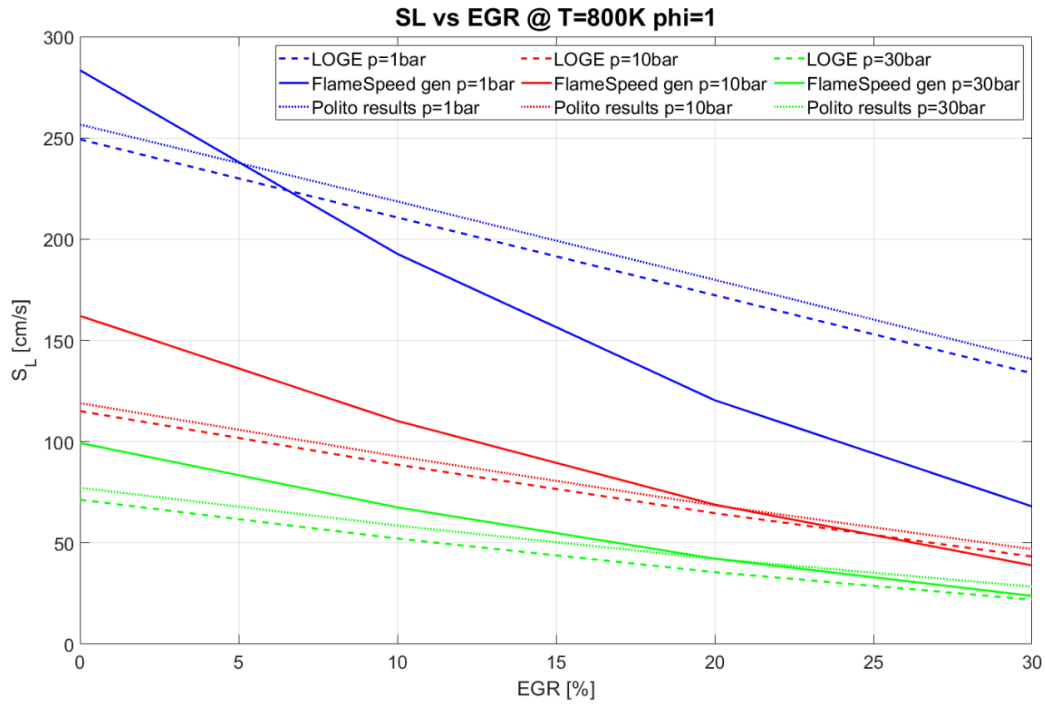

Figure 56: Comparison results of LOGE mechanism, of Flame Speed generator and of Polytechnic for HCNG15 in function of EGR @ p=1,10,30bar, phi=1 and T=800K

- HCNG25

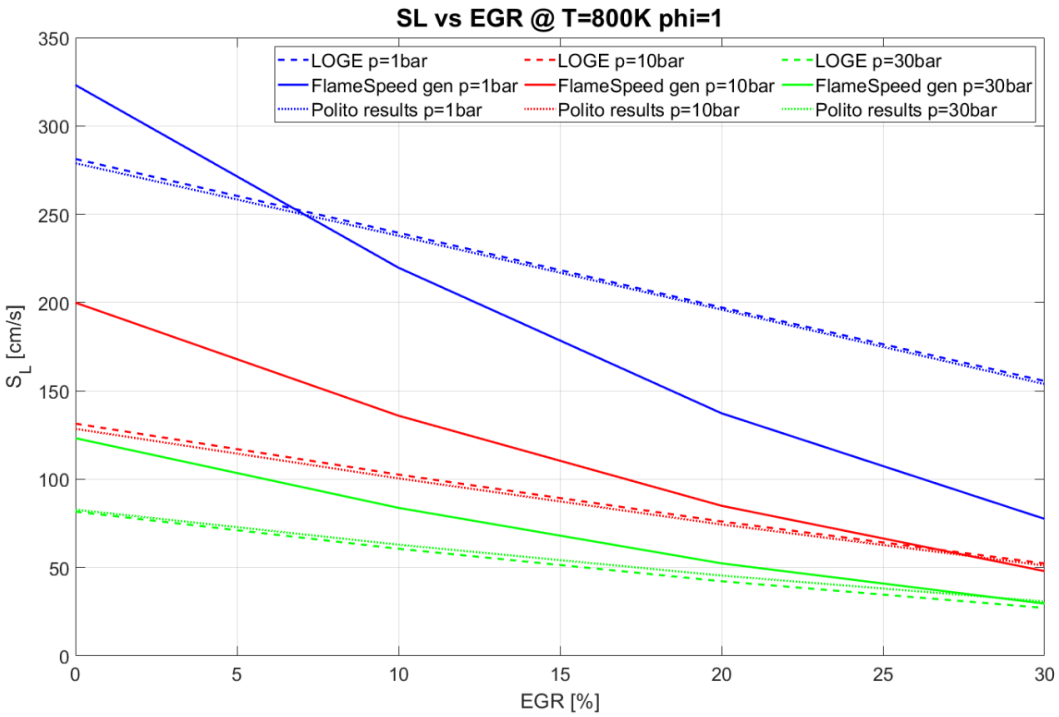

Figure 55: Comparison results of LOGE mechanism, of Flame Speed generator and of Polytechnic for HCNG25 in function of EGR @ p=1,10,30bar, phi=1 and T=800K

- 8713

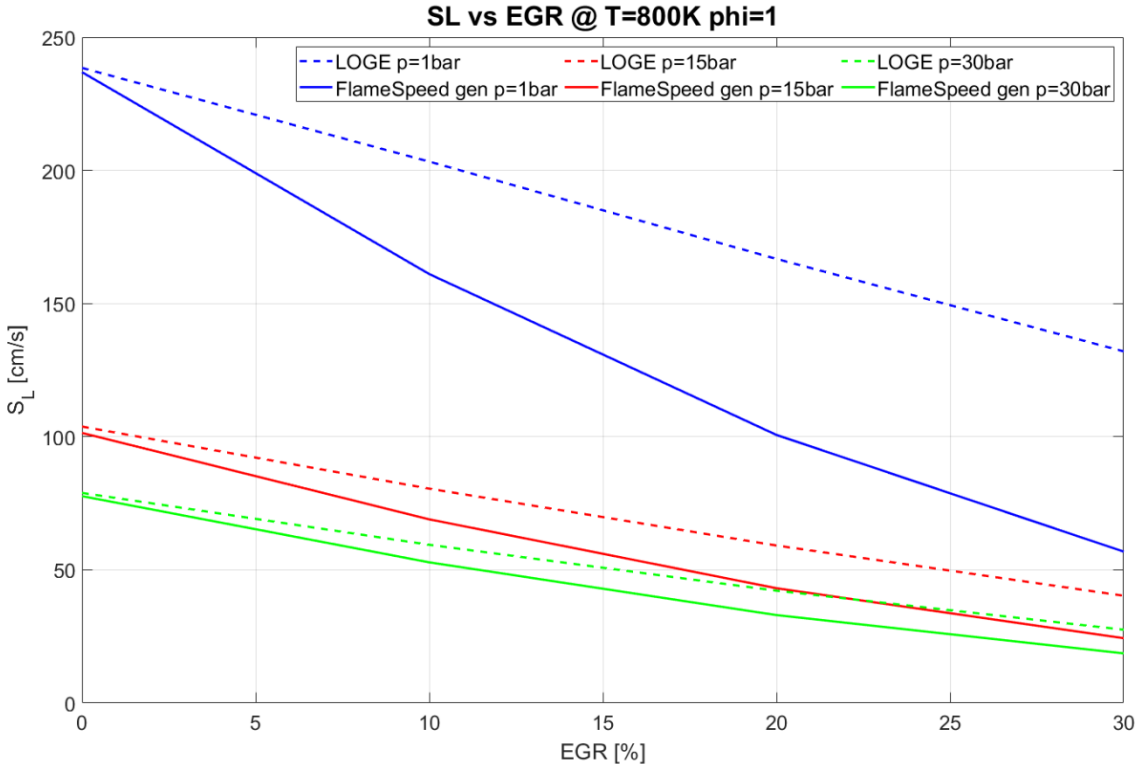

Figure 56: Comparison results of LOGE mechanism, of Flame Speed generator and of Polytechnic for 8713 in function of EGR @ p=1,15,30bar, phi=1 and T=800K

- Mix I-C4H10

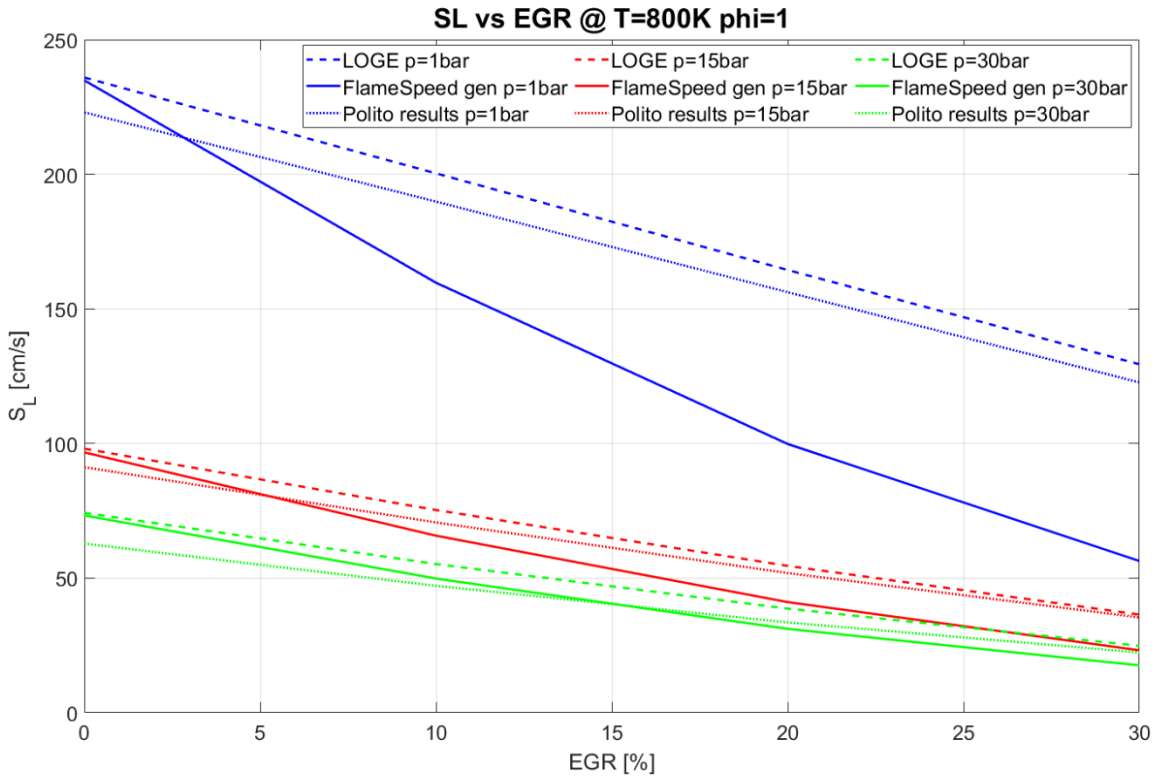

From the results obtained it is clear that, as regards the results obtained with LOGEresearch and with DARS, they are very close for each blend and for each condition studied. While, regarding the results obtained with Flame Speed Generator Tool, they are close to the other results only for blends that don't contain hydrogen and with a null dilution; the reason why the results obtained with Flame Speed Generator Tool with the blends with hydrogen don't fit with results obtained with LOGEresearch and DARS is because the linear mixing of pure component used in this tool is not appropriate for blends with hydrogen which behaves different from other components. As regard the results obtained with Flame Speed Generator Tool with EGR, the results are different because the EGR is a linear fit based on laminar flame speed calculations with a detailed mechanism.

6. CFD Analysis

6.1. Model

The simulations have been made on a 1.4 liter compressed engine, with a pent-roof chamber, four valves per cylinder and a centrally located spark plug. The engine main specifications are listed in *Table 5,* while in *Figure 60* and *Figure 61* two views of the simulated engine are shown:

Stroke	84.0 mm
Bore	72.0 mm
Displacement	1367 cm^3
Compression Ratio	9.8
Cylinder number	4
Type	Spark Ignition
n	2000 rpm

Table 5: Test engine characteristics

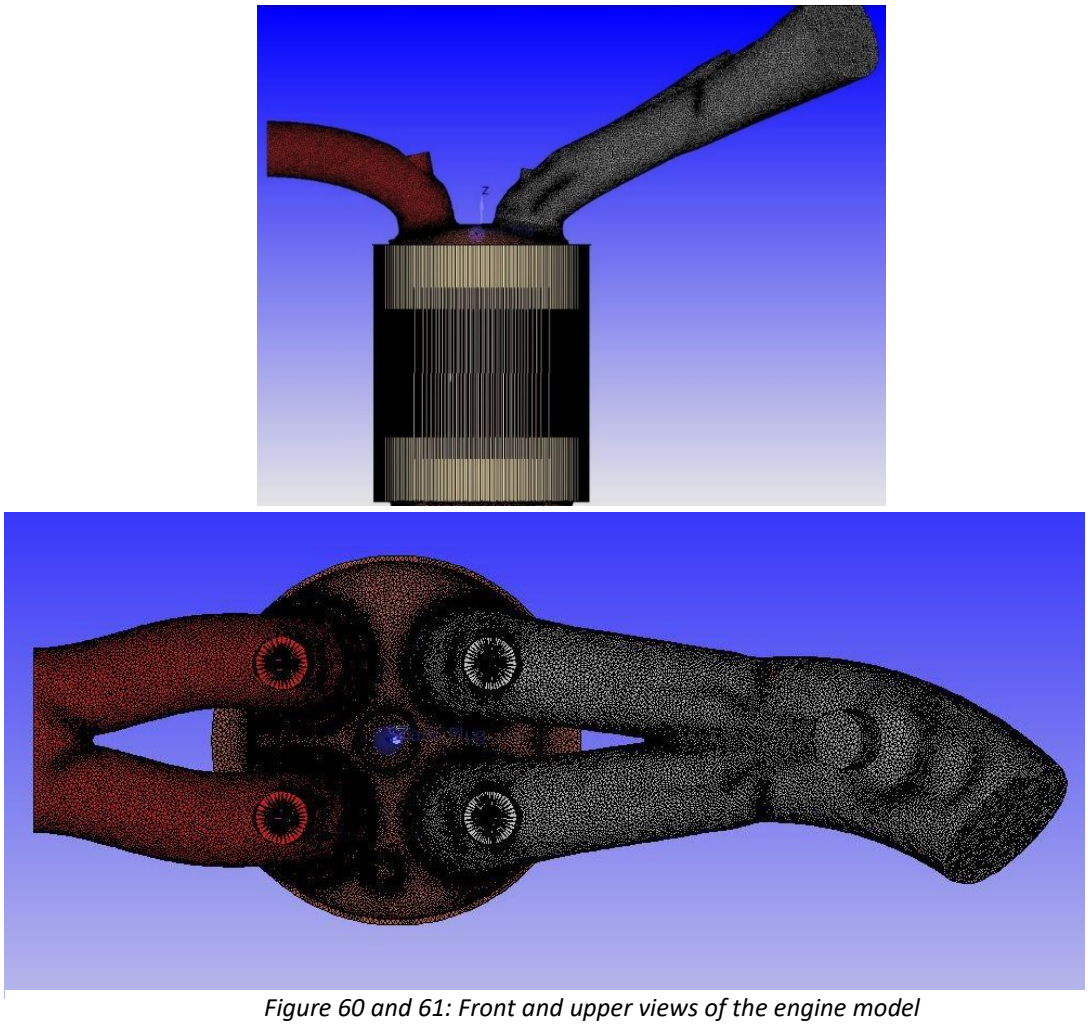

Figure 60 and 61: Front and upper views of the engine model

6.1.1. Features and setup

The combustion model used in this setup is the *ECFM* model, mentioned in chapter 6.3. and the Turbulence model is the RNG *k-ε model*, mentioned in chapter 6.2. Concerning to the setup of the Polytechnic of Turin, the fuel used is pure methane (CH_4) and its Flame Table was generated by DARS with GRI mechanism. In the next table (*Table 6*) the boundaries are indicated:

	Range	Steps
Temperature	300 ÷ 1600K	100 K
Pressure	1 ÷ 200 bar	Variable
Equivalence Ratio	0 ÷ 5	0.1
EGR	0-100%	10%

Table 6: Boundaries considered in DARS

6.1.2. Results

Here the results obtained with Converge are shown (*Figure 62*,63,64,65):

- Pressure [bar] (*Figure 62*):

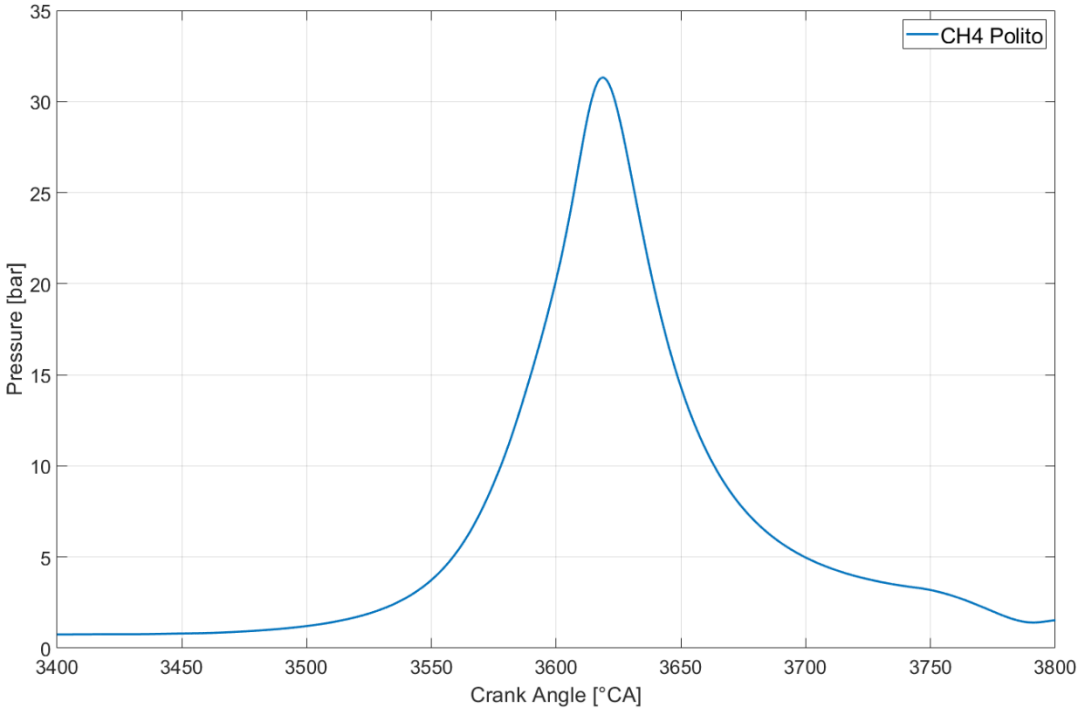

Figure 62: Profile of pressure obtained for pure methane from the Polytechnic of Turin

- Heat Release Rate [J/°CA] (*Figure 63*):

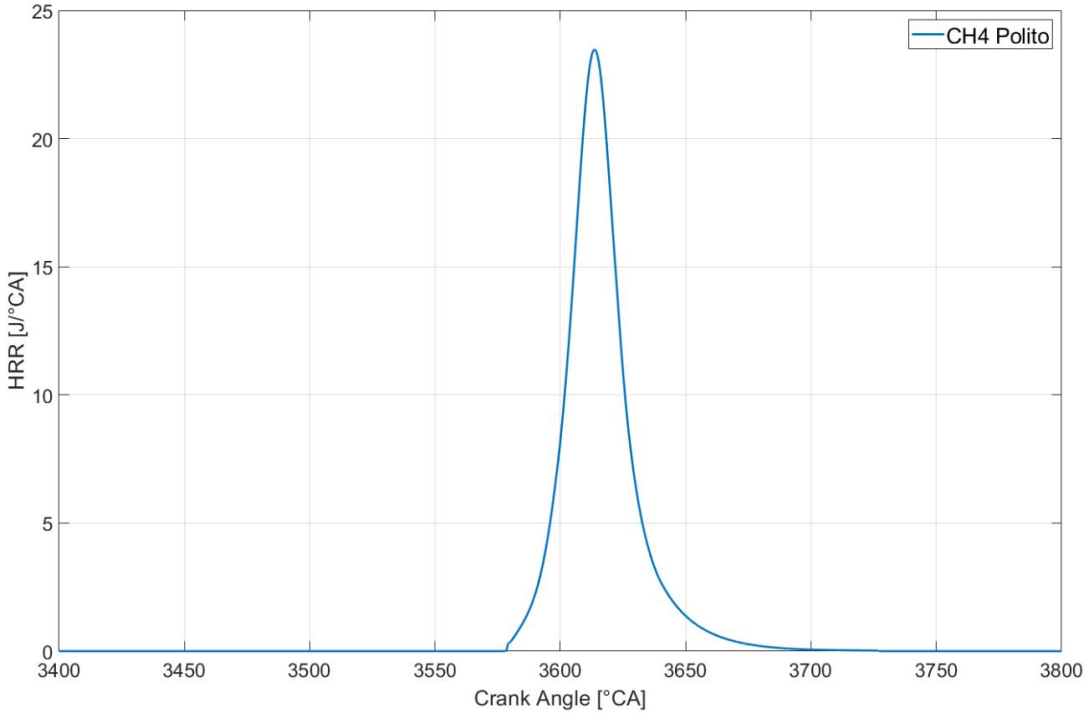

Figure 63: Profile of Heat Release Rate obtained for pure methane from the Polytechnic of Turin

The reason why there is no heat release in the unburned zone, is it because the reaction scheme used is without low-temperature chemistry. This means that the reaction is underestimating the auto-ignition tendency of the fuels, which is good to study the flame speed and avoid additional combustion due to auto-ignition in the unburned zone.

- Mass Fraction Burned (*Figure 64*):

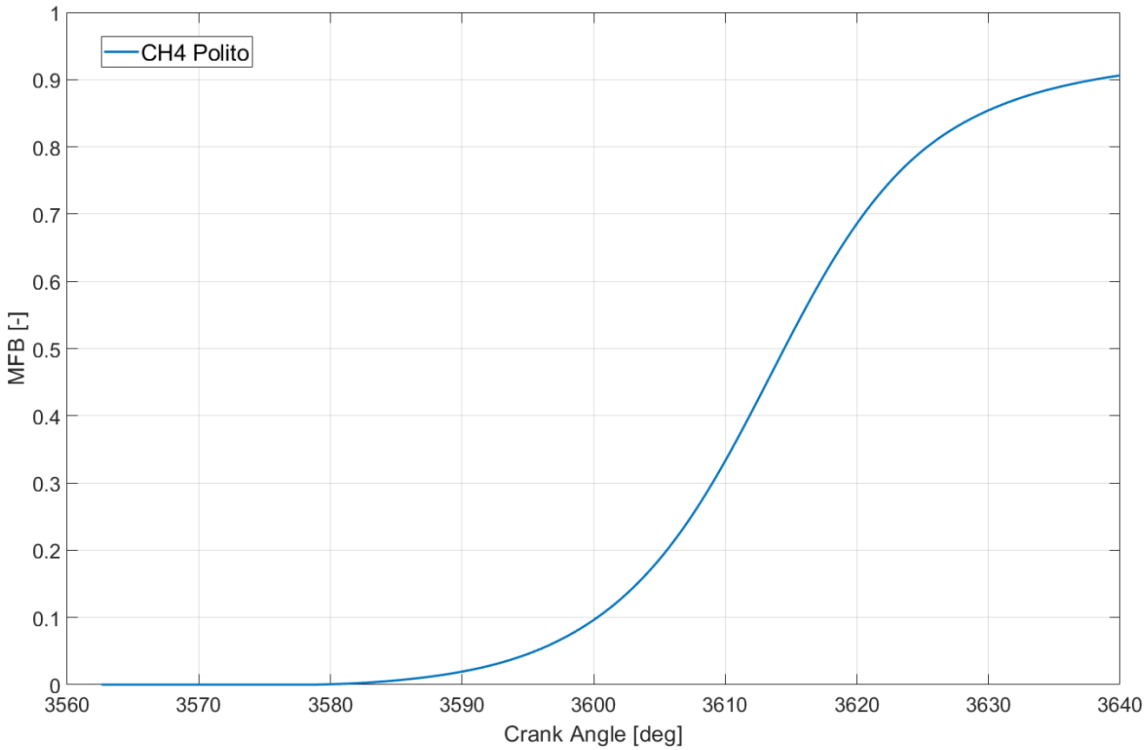

Figure 65: Profile of MFB obtained for pure methane from the Polytechnic of Turin

- Integrated Heat Release [J] (*Figure 66*):

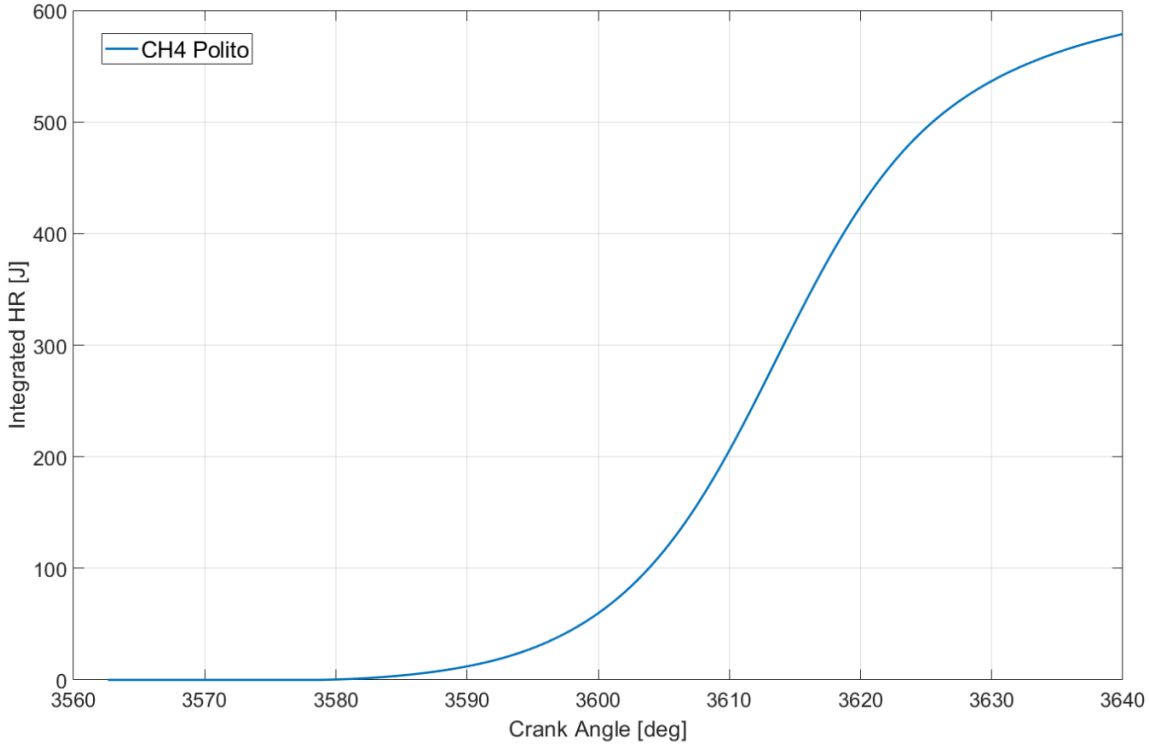

Figure 66: Profile of Integrated Heat Release obtained for pure methane from the Polytechnic of Turin

The x axis the Crank Angle starts from 3060°CA because it was considered the 11th cycle and the results are plotted from 300°CA because we are not interested in the results before that crank angle. The spark advance (SA) chosen for this case was equal to 26° BTDC, that corresponds to a Crank Angle of 3578° CA.

6.2. Results obtained for Blends

6.2.1. Without calibration

Here below are shown all the results obtained for the five blends introduced in chapter 7.3. These results were obtained first without the calibration of the Spark Advance and they were compared to the results shown in chapter 8.1 for pure Methane (black line).

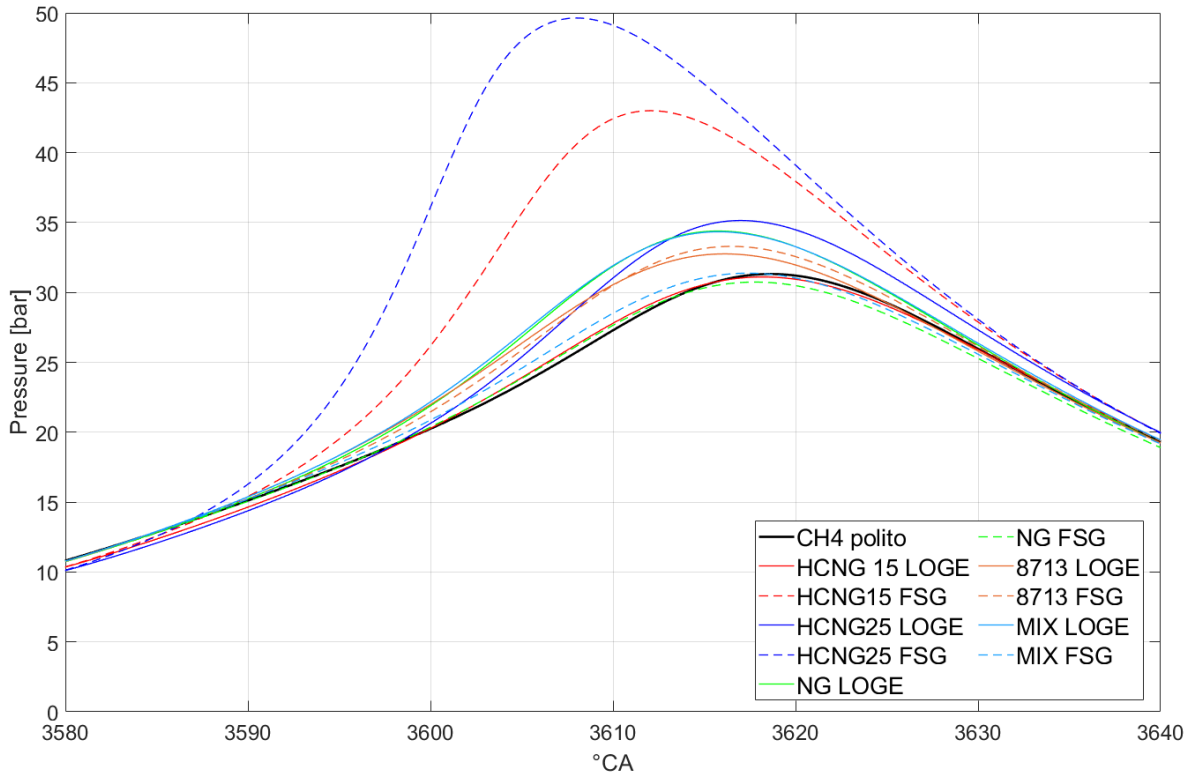

Figure 67: Profile of pressure obtained for blends without SA calibration, compared to the pressure of pure Methane

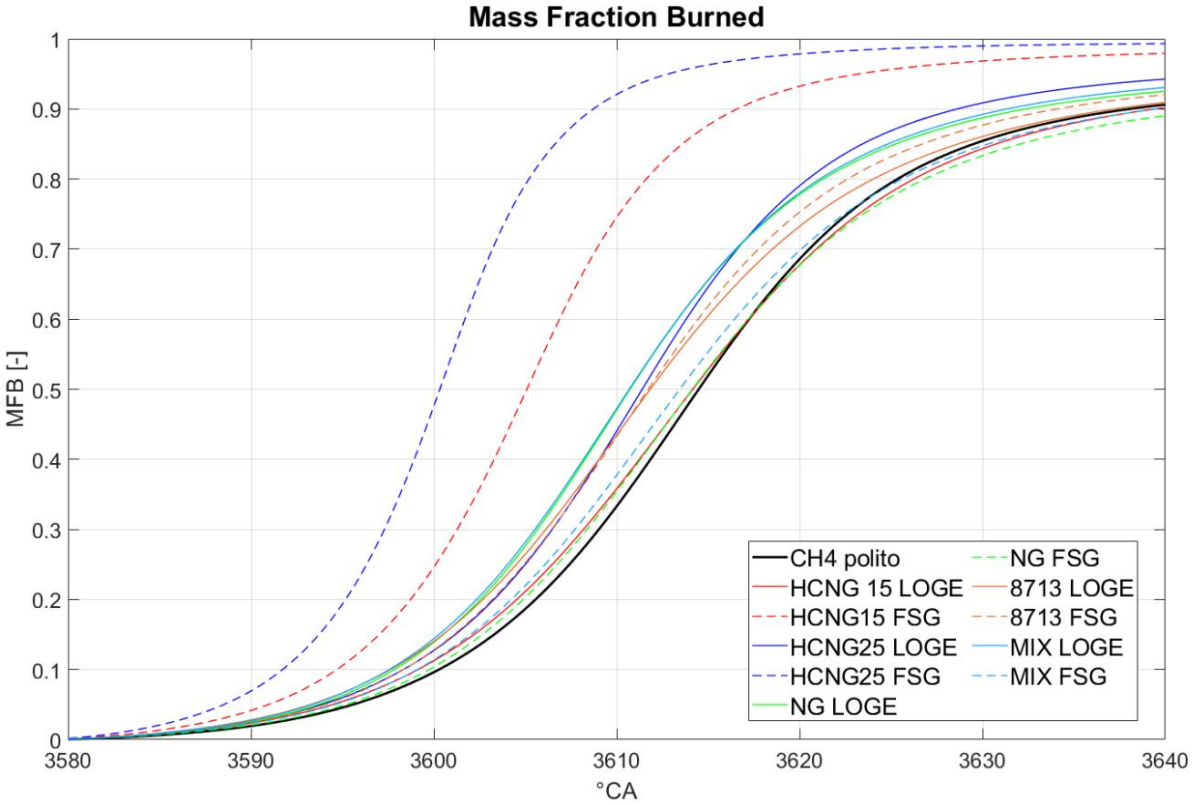

Figure 67: Profile of MFB obtained for blends without SA calibration, compared to the MFB of pure Methane

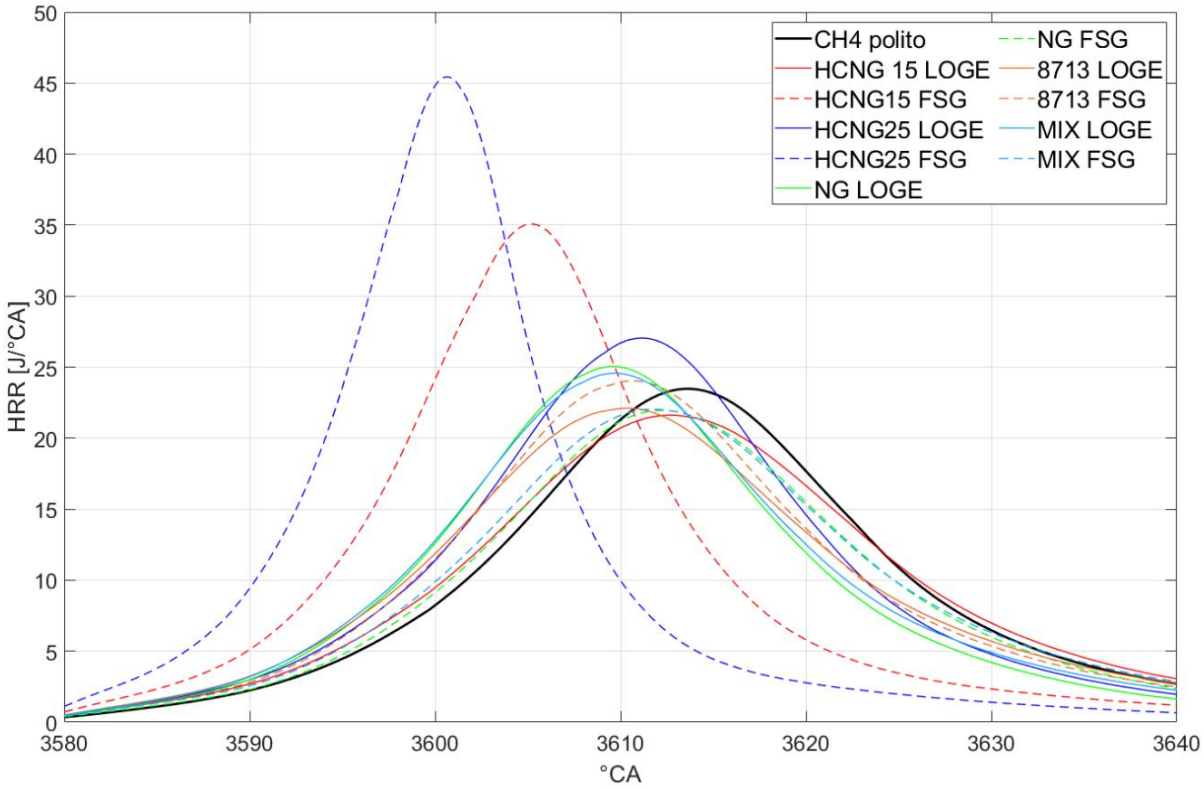

Figure 68: Profile of HRR obtained for blends without SA calibration, compared to the HRR of pure Methane

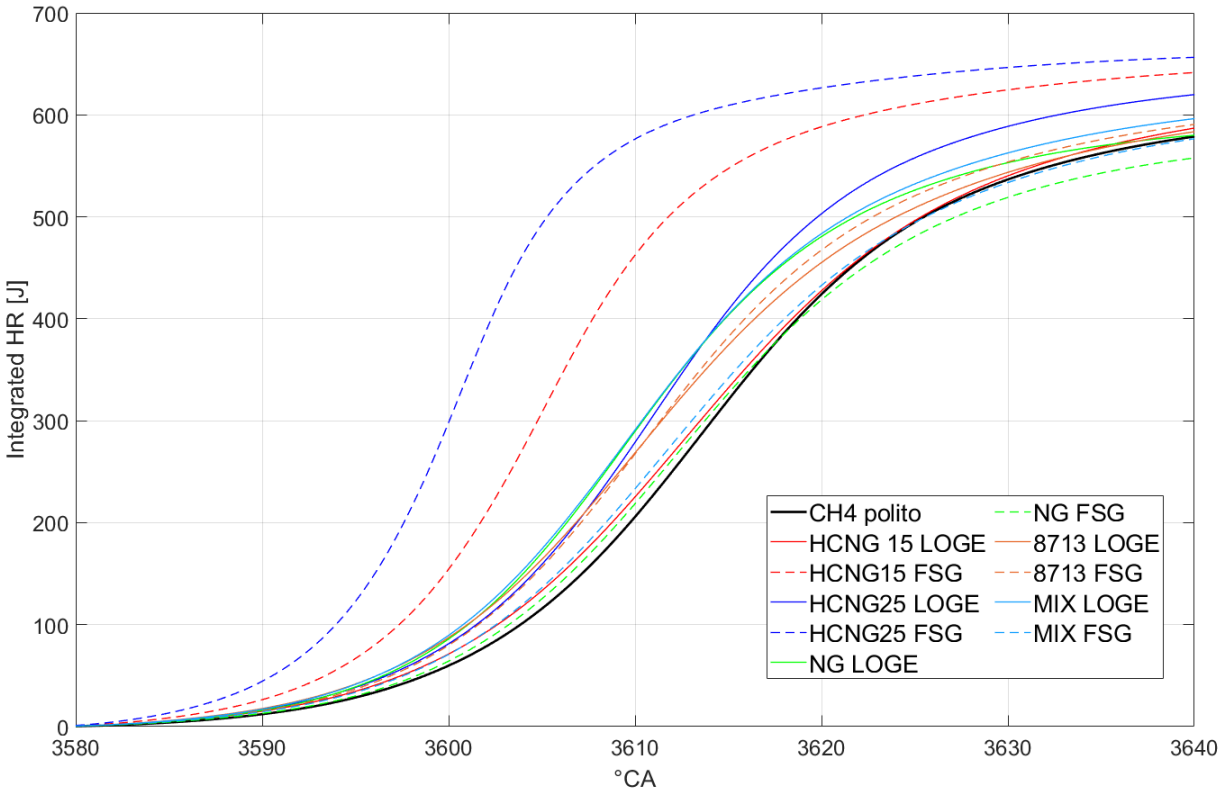

Figure70: Profile of Integrated HRR obtained for blends without SA calibration, compared to the Integrated HRR of pure Methane

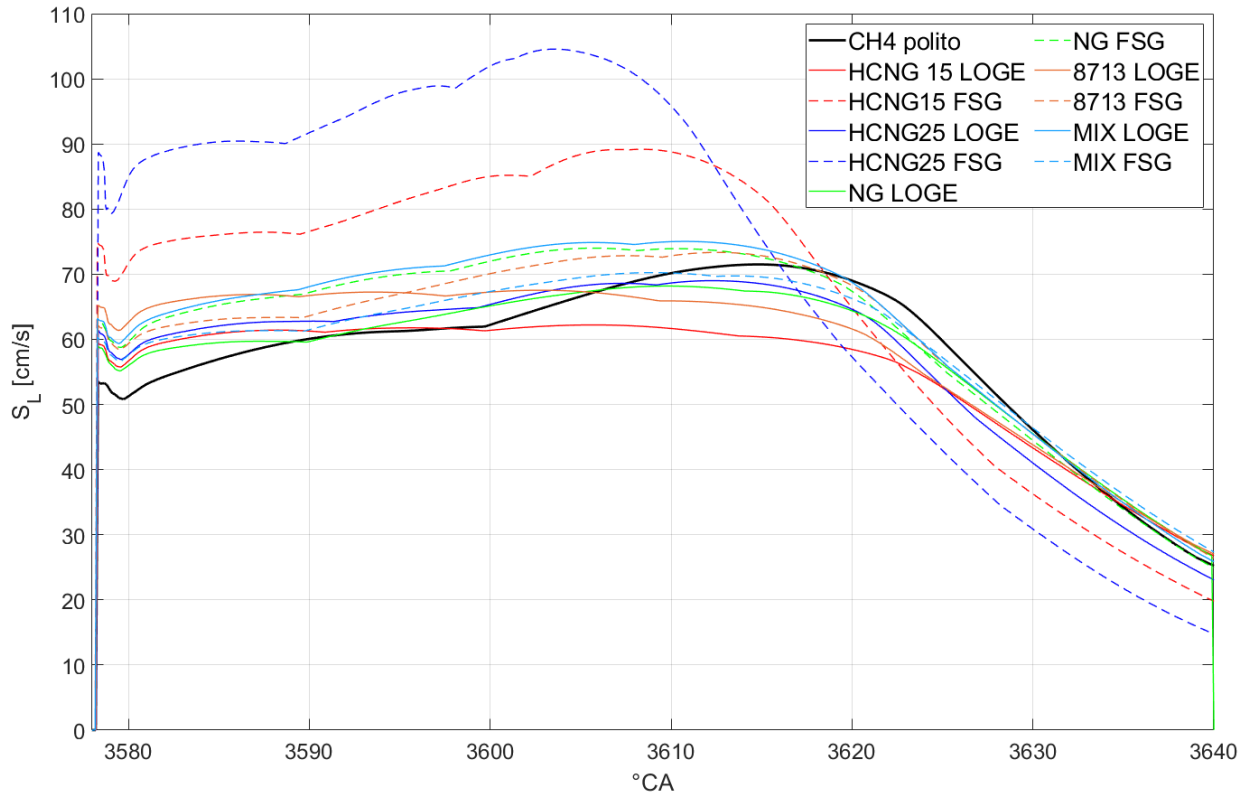

Figure 71: Profile of flame speed obtained for blends without SA calibration, compared to the flame speed of pure Methane

In the following table (*Table 7*) are shown the values of Spark Advance, Crank Angle where MFB50 is reached (CA50), the maximum pressure reached and its Crank Angle.

FUEL	SA [°CA BTDC]	CA50	Pmax [bar]	CA_Pmax	|ΔCA50|
CH4 (Ref. Fuel)	26	3614.52	31.32	3618.60	
HCNG15 FPF	26	3614.14	31.11	3618.22	0.38
HCNG15 FSG	26	3605.11	43.00	3612.07	9.41
HCNG25 FPF	26	3611.38	35.14	3617.02	3.14
HCNG25 FSG	26	3600.31	49.63	3607.99	14.21
NG FPF	26	3610.73	34.39	3615.77	3.79
NG FSG	26	3614.09	30.74	3617.81	0.42
8713 FPF	26	3611.87	32.76	3616.07	2.64
8713 FSG	26	3611.67	33.29	3616.47	2.85
MIX FPF	26	3613.46	31.38	3617.42	1.06
MIX FSG	26	3610.67	34.34	3615.83	3.84

Table 7: Main results obtained from CFD simulations without calibration

The last column of Table 7 "$|\Delta CA50|$" corresponds to the absolute value of the difference between the Crank Angle where the MFB50 is reached for methane and the one for the blend. It was decided that if this value exceeds the inferior and superior thresholds of ±0.5 Crank Angle, it is necessary to perform a calibration of the Spark Advance. This is shown in the following bar chart (*Figure 72*). For simplicity, it was chosen 3600 °CA as 0 °CA.

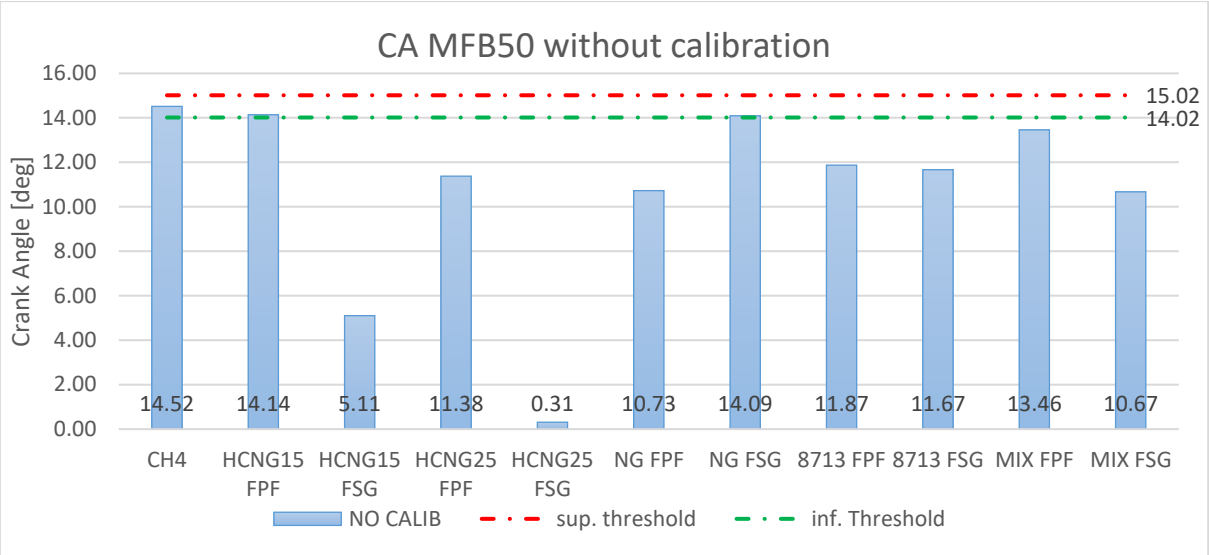

Figure 72: Value of MFB50 for each blend without calibration

From this bar plot, we note that only two blends don't need to be calibrated, HCNG15 FPF and NG FSG. While, as regards the other blends, these require a Spark Advance calibration.

6.2.2. Calibration

As shown in the previous figure (*Figure 71*), to guarantee a reasonable *ΔCA50,* eight of the ten blends, need to be calibrated.

After several tries, the results obtained from the calibration are shown in in the following plots (*Figure 73,74,75,76,77)*

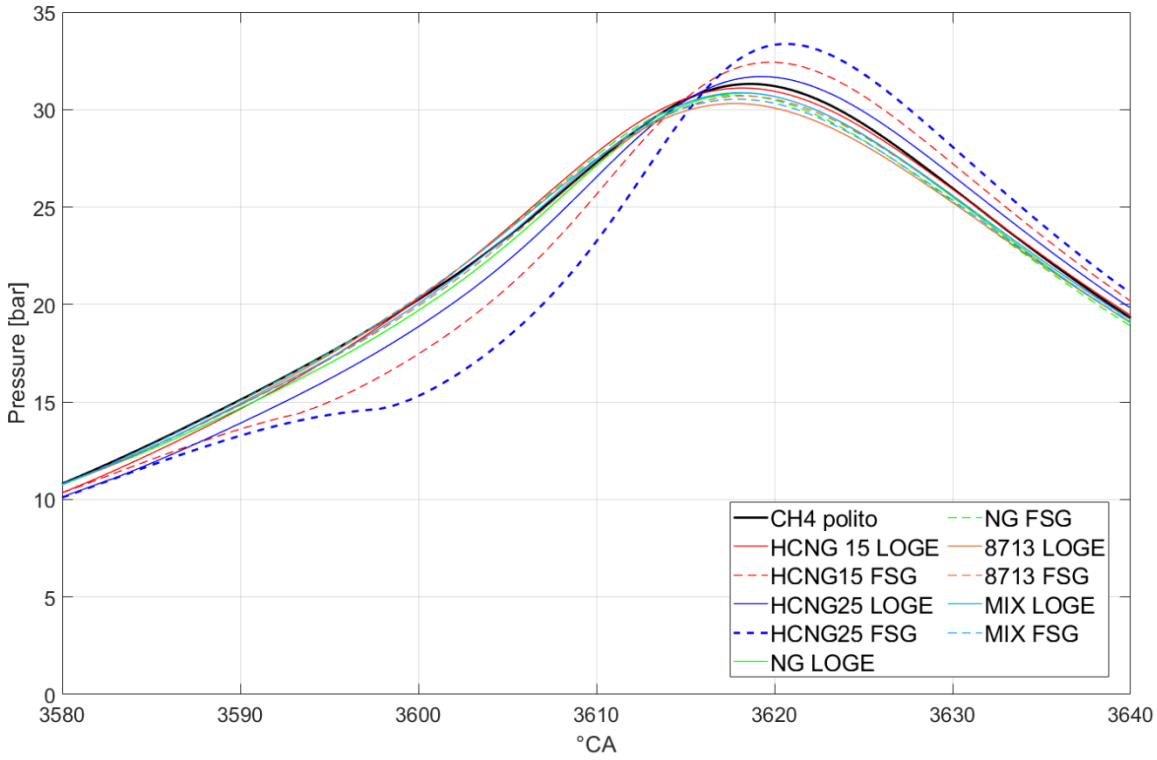

Figure 73: Profile of pressure obtained for blends with SA calibration, compared to the pressure of pure Methane

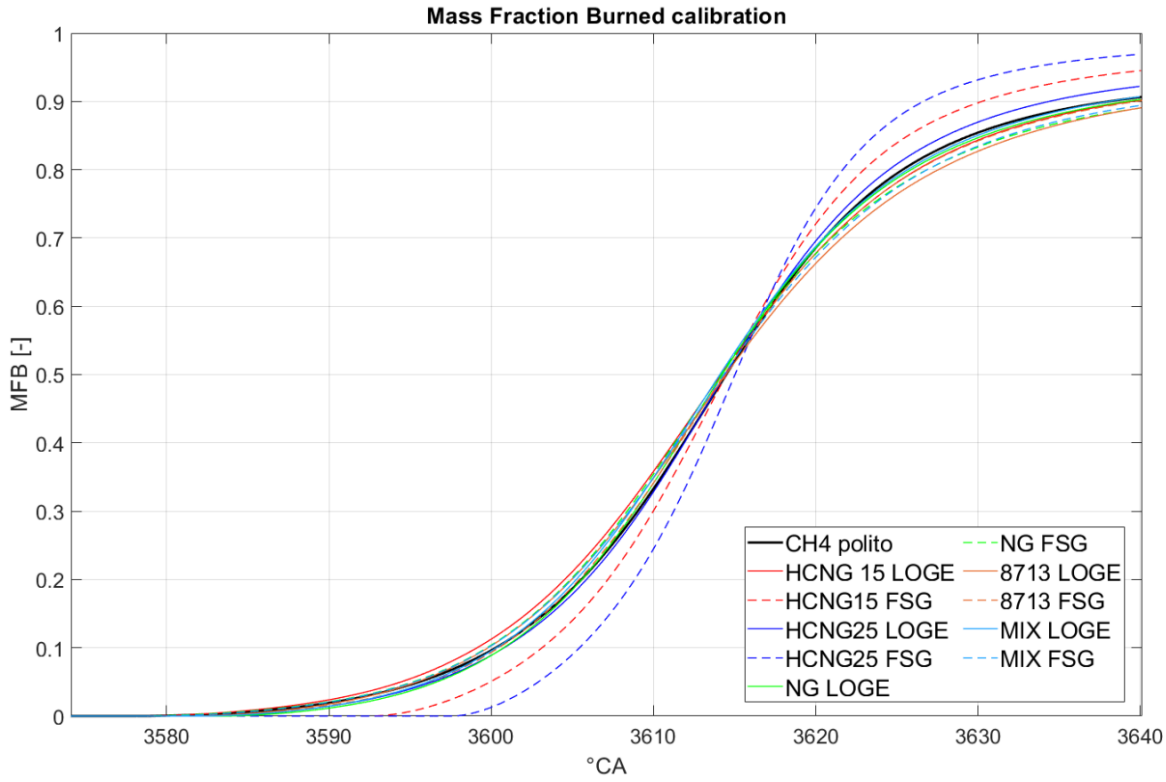

Figure 74: Profile of MFB obtained for blends with SA calibration, compared to the MFB of pure Methane

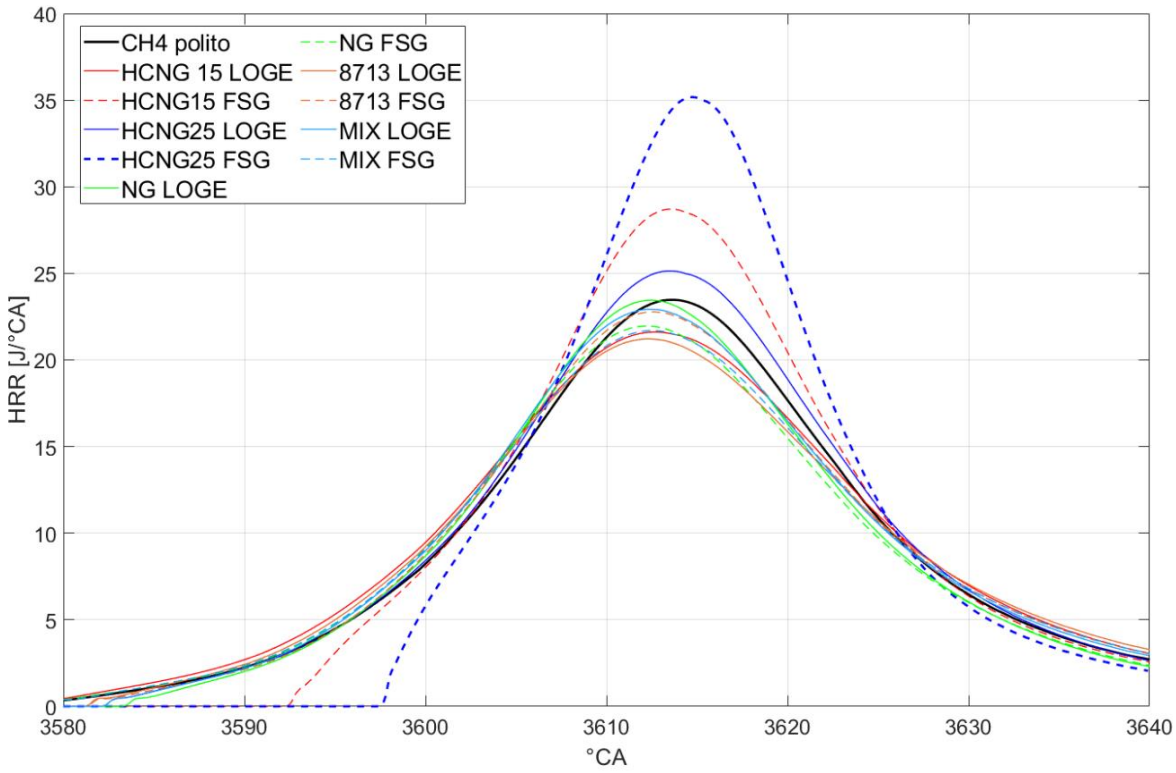

Figure 75: Profile of HRR obtained for blends with SA calibration, compared to the HRR of pure Methane

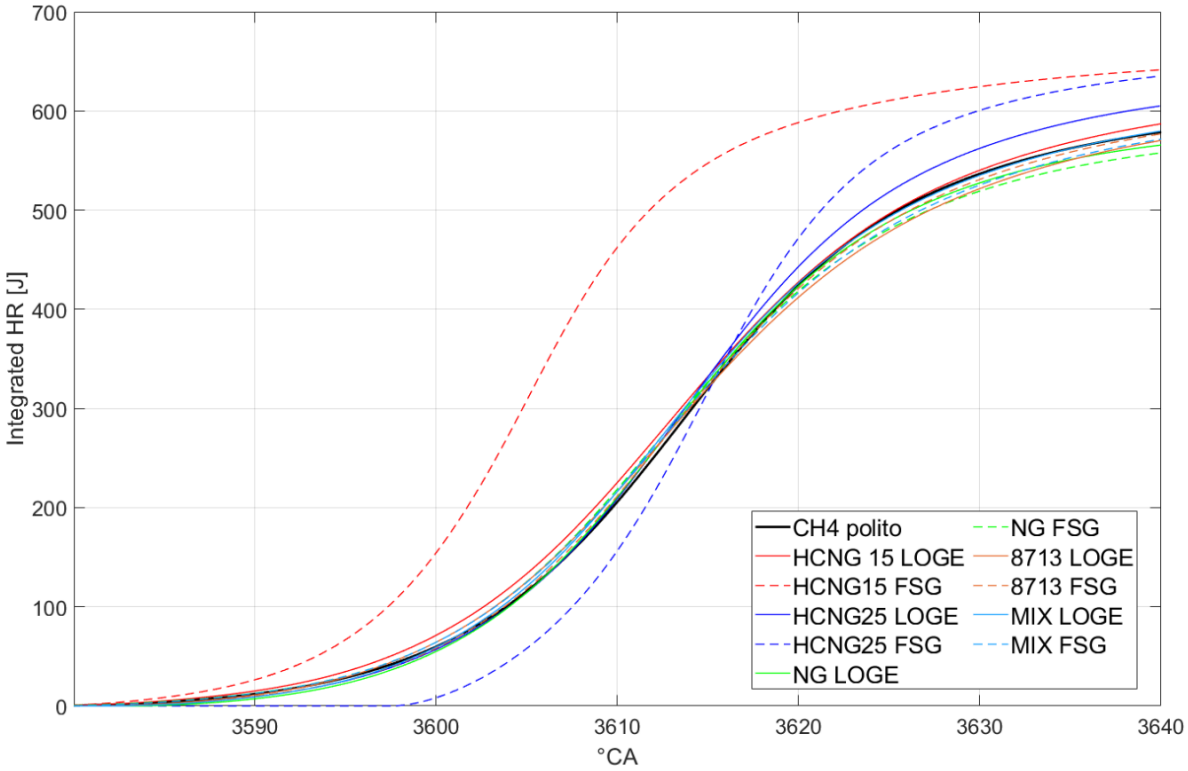

Figure 76: Profile of Integrated HRR obtained for blends with SA calibration, compared to the Integrated HRR of pure Methane

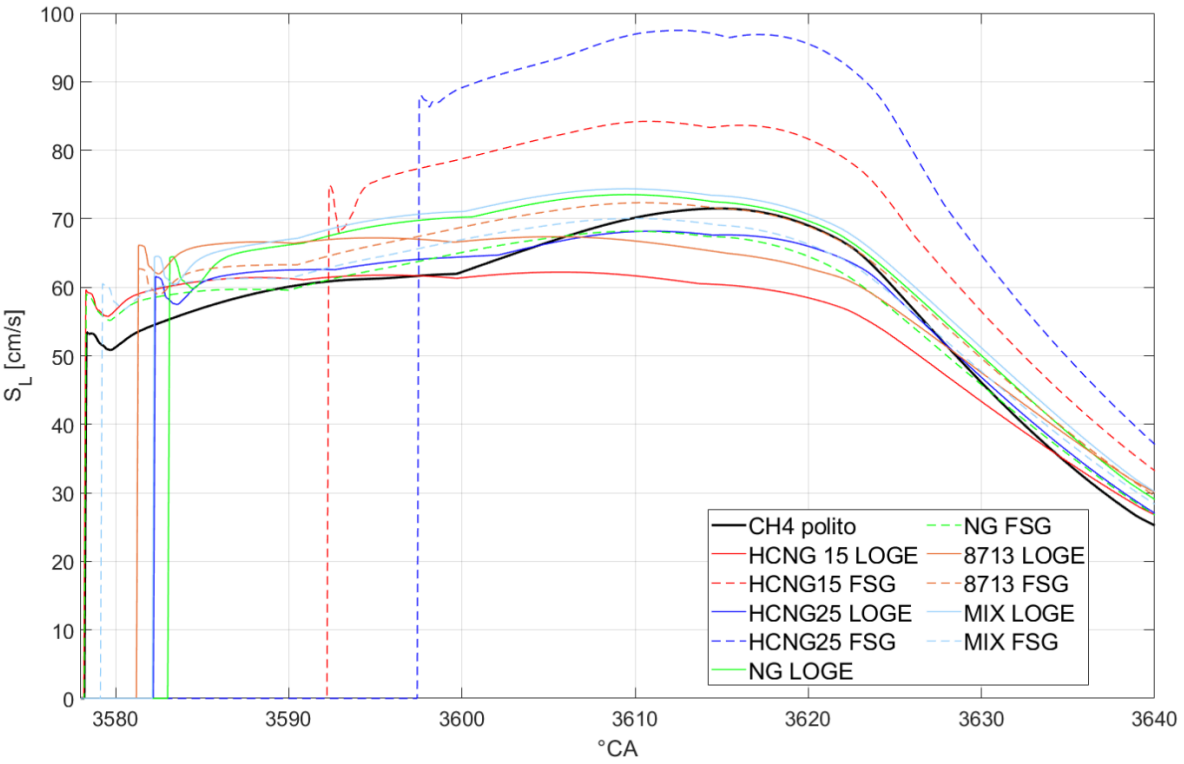

Figure 77: Profile of flame speed obtained for blends with SA calibration, compared to the flame speed of pure Methane

In this new table (*Table 8*) are shown the new values of Spark Advance chosen for the calibration and the new values of CA50, Pmax and its Crank Angle.

FUEL	SA [°CA BTDC]	CA50	Pmax [bar]	CA_Pmax	|ΔCA50|
CH4 (Ref. Fuel)	26	3614.52	31.32	3618.60	
HCNG15 FPF	26	3614.14	31.11	3618.22	0.38
HCNG15 FSG	12	3614.47	32.43	3619.75	0.05
HCNG25 FPF	22	3614.38	31.69	3619.30	0.14
HCNG25 FSG	6.8	3615.07	33.37	3620.59	0.55
NG FPF	21	3614.21	30.85	3618.17	0.31
NG FSG	26	3614.09	30.74	3617.81	0.43
8713 FPF	23	3614.51	30.31	3617.75	0.00
8713 FSG	23	3614.31	30.70	3618.27	0.21
MIX FPF	22	3614.03	30.87	3618.11	0.48
MIX FSG	25	3614.30	30.53	3617.90	0.22

Table 8: Main results obtained from CFD simulations with calibration

the bar chart in *Figure 78* shows that the MFB50 are contained within the chosen thresholds:

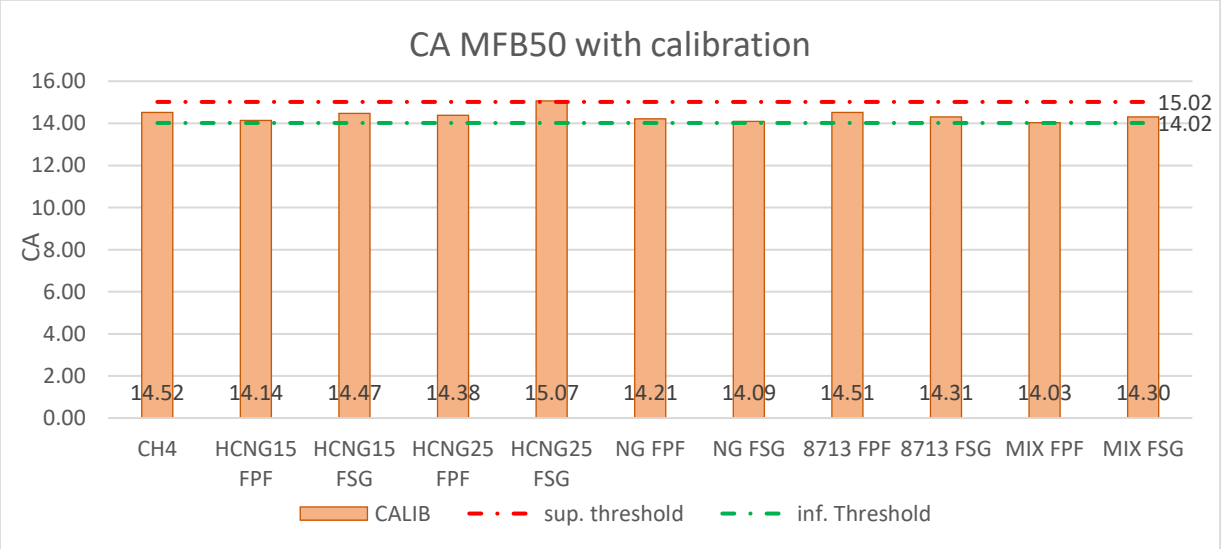

Figure 78: Value of MFB50 for each blend with calibration

The only exception was made for the blend HCNG15 FSG because that value of *ΔCA50* was the best obtained from all the tries of calibration.

7. SI – SRM Analysis

As said in Chapter 6, the reason why we want to compare the results of SRM with the results of CONVERGE is because the first one has a lower computational cost compared to the one of CONVERGE. SRM models are run in stand-alone mode with *Essa.exe* that is an executable of LOGEengine. To set the simulation SRM needs several inputs, the most important are *IgnUserSet* that contains information about engine data (stroke, bore, CR, rpm), reactor model and run time option and *GasComposition* that contains the initial gas mixture and the initial pressure and temperature. All these data are taken from 3D CFD simulation output. Moreover, it is necessary to make a parametrization of the mixing time [56] (τ, which is a measure of mixing or turbulence intensity) for the SI-SRM (τ_{SRM}); ideally, the turbulence mixing time can be taken from 3D CFD calculations τ_{CFD} (k/ε ratio); that is possible considering C_ϕ (64):

$$\tau_{SRM} = C_\phi \tau_{CFD} \quad (64)$$

In the next graphs are shown the results obtained for pure methane compared to CFD results from Polito (*79, 80*) and the results obtained for NG (81, 82). All the results obtained for other blends are shown in the Appendix (83, 84, 85, 86, 87, 88, 89, 90).

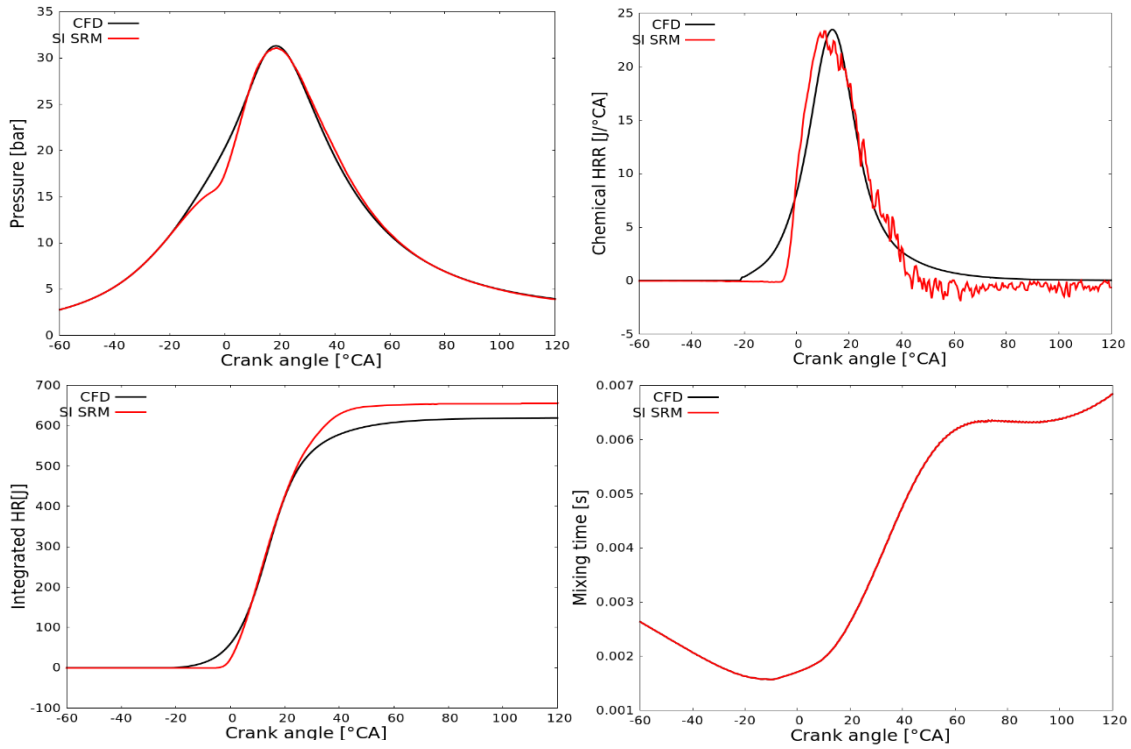

Figure 79: Pressure, Heat Release Rate, Integrated HR and mixing time obtained for both CFD and SRM for pure methane (Polito case)

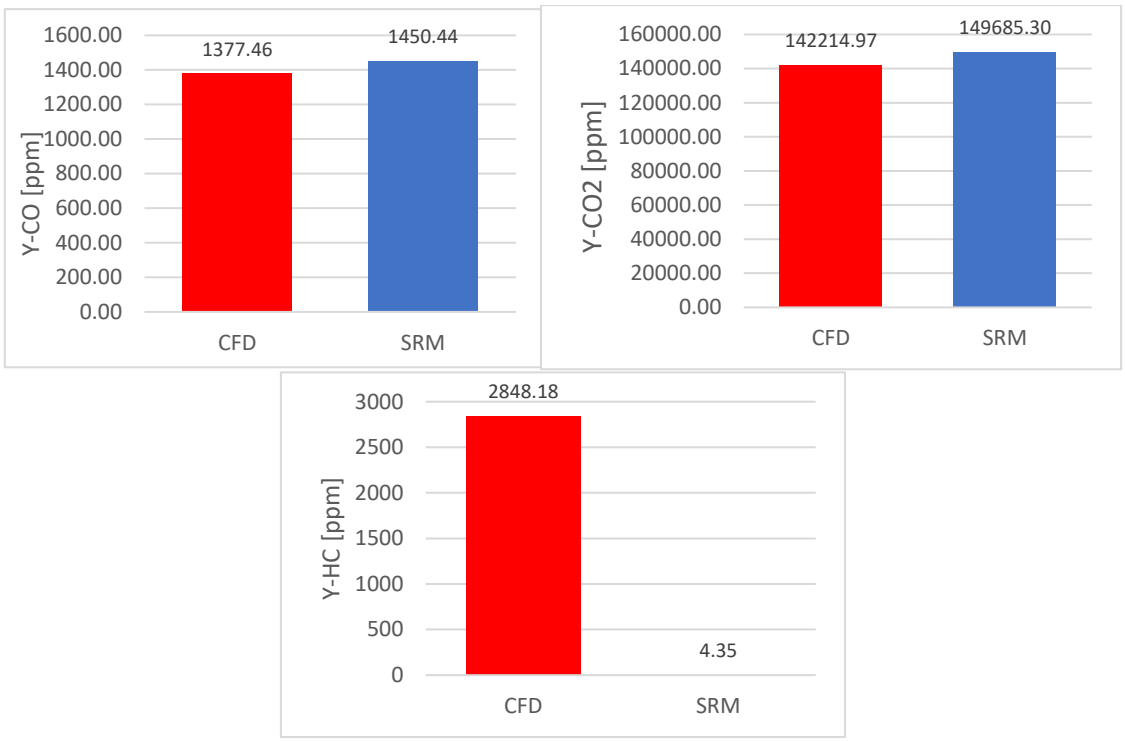

Figure 80: CO, CO2 and HC emissions obtained for both CFD and SRM for pure methane (Polito case)

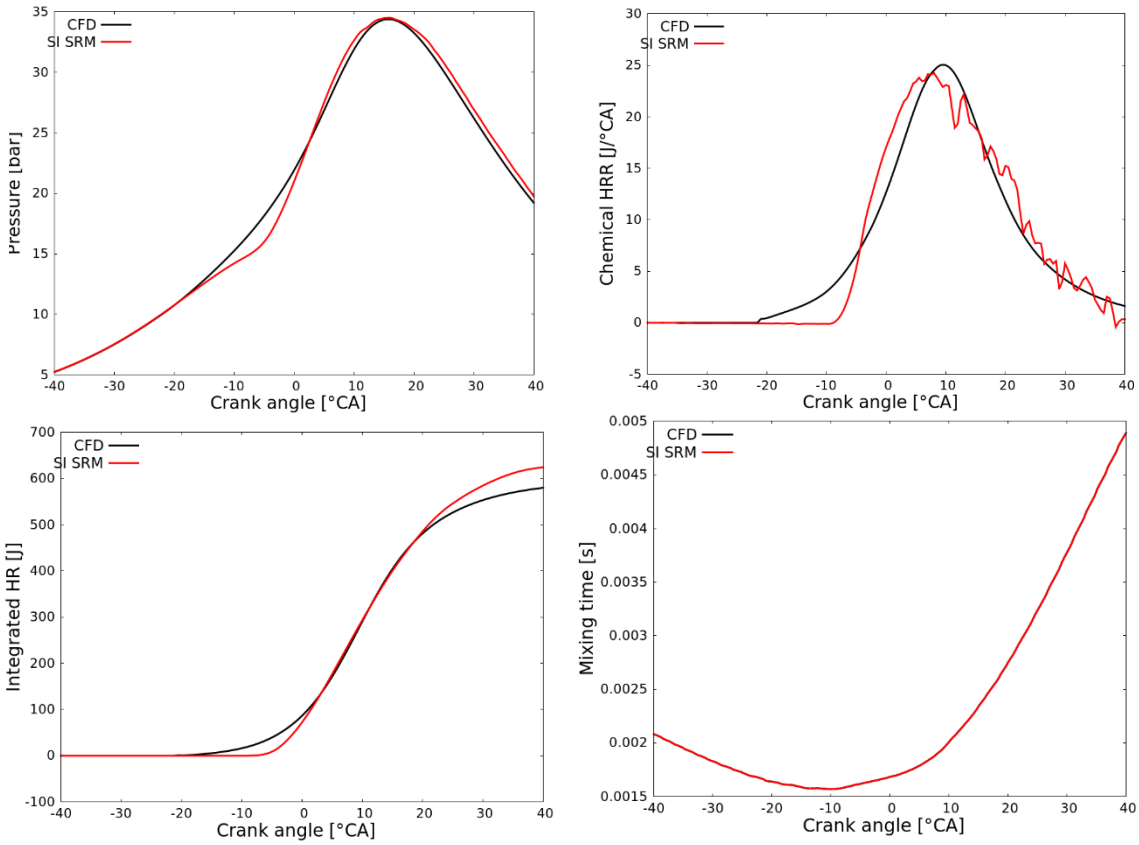

Figure 81: Pressure, Heat Release Rate, Integrated HR and mixing time obtained for both CFD and SRM for NG

Figure 82: CO, CO2 and HC emissions obtained for both CFD and SRM for NG

In the next table (*Table 9*) are shown the values of Spark Advance and C_ϕ used in SRM simulations for each blend:

	SA [°CA BTDC]	C_ϕ [-]
CH4 polito	7.5	6.1
NG	9	6.1
HCNG15	6	6.1
HCNG25	5.5	5.6
8713	8.5	6.5
MIX	9	6.5

Table 9: SA and tau factor used in SI SRM simulations

8. CONCLUSIONS

The aim of this work was to compare different methodologies to create laminar flame speed tables of varying blends. Two different kinetic mechanisms have been used, *GRI* and *LOGE mechanisms;* the second one is more complex than the first one and contains a higher number of reactions. Moreover, two different methods are used; the first one creates the surrogate first and then calculates its flame speed table, the second method consists in creating first the flame speed table for each pure fuel and uses linear mixing in order to obtain the flame speed table for a surrogate. Both methods use *LOGE mechanism.* The two methods were compared because the second one has a significantly lower computational cost than the first. Then, to understand the behaviour of these blends, the generated and validated flame speed tables are applied to 3D CFD engine simulations for further validations. The cases have been calibrated for each blend, to the same MFB50 of the reference case (*Chapter 6*). In a last step, additional investigations have been made with the help of 0D SRM engine simulation for each blend and their results were compared with the results obtained with the 3D CFD simulations.

A validation of the kinetic mechanism has been carried out for each pure fuel present in the blends (*Chapter 4*). After the validation, the predicted laminar flame speeds have been compared at different conditions: standard engine conditions, lean, rich and diluted combustion. The results obtained in *Chapter 5* show that for all blends that don't contain hydrogen, the flame speeds obtained are very close to each other. However, for the result obtained with blends that contain hydrogen, only flame speeds obtained with the first method are close to the results obtained with *GRI mechanism*. The flame speed obtained with the second method have a different trend because the linear mixing used in this tool is appropriate for blends that don't contain hydrogen. This problem occurs because hydrogen has a different behaviour from other fuels. The same was found in mixtures containing EGR, because the EGR is a linear fit based on laminar flame speed calculations with a detailed mechanism. However, two different version of the same reaction schemes have been used for the different methods.

The results obtained from 3D CFD simulations show that, as discussed before, blends containing hydrogen obtained with the second method show a different behaviour from all other blends both before and after calibration.

The results obtained from 0D SRM simulations show that, with appropriate calibrations of coefficients, the results are close to those obtained with 3D CFD simulations.

In future work, an investigation of the impact of discretization of the table on the combustion prediction, should be carried out. Also, a more accurate study of flame speed tables obtained with the second method should be done for blends with addiction of hydrogen or EGR, to try to reduce the gap with the first method. Furthermore, also a better calibration of parameters of SRM setup should be done in order to try to obtain results closer to those obtained with 3D CFD simulation and to make a more accurate study also at different engine conditions.

APPENDIX

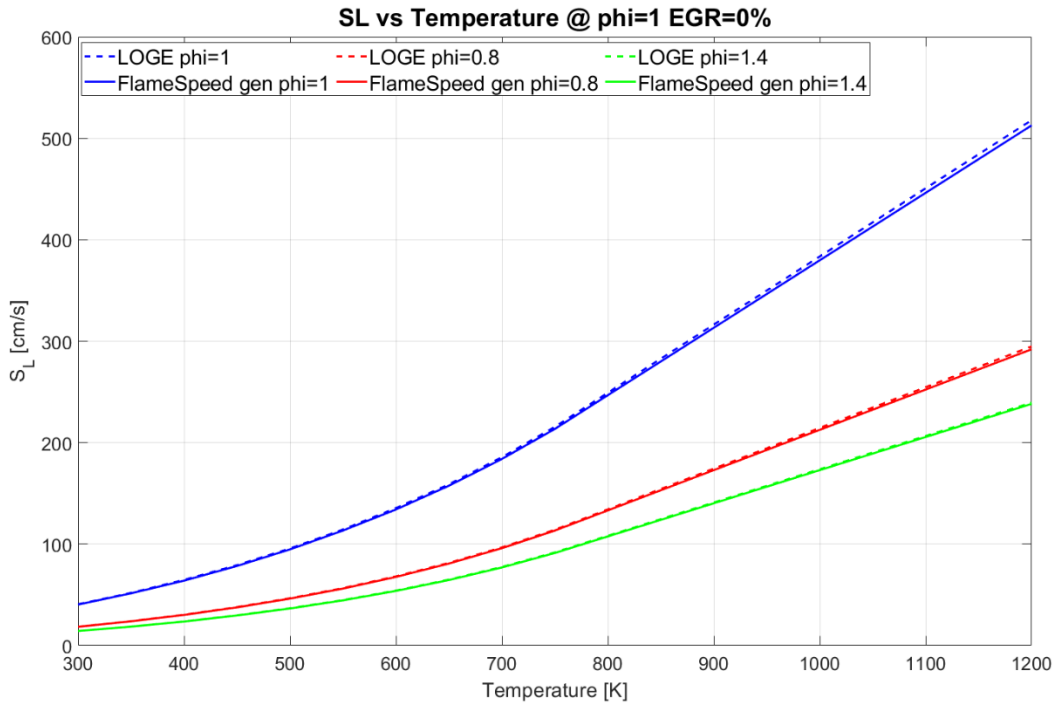

Figure 21: Comparison results of LOGE mechanism and of Flame Speed generator for ethane in function of Temperature @ p=1bar,15bar,30bar EGR=0% and phi=1

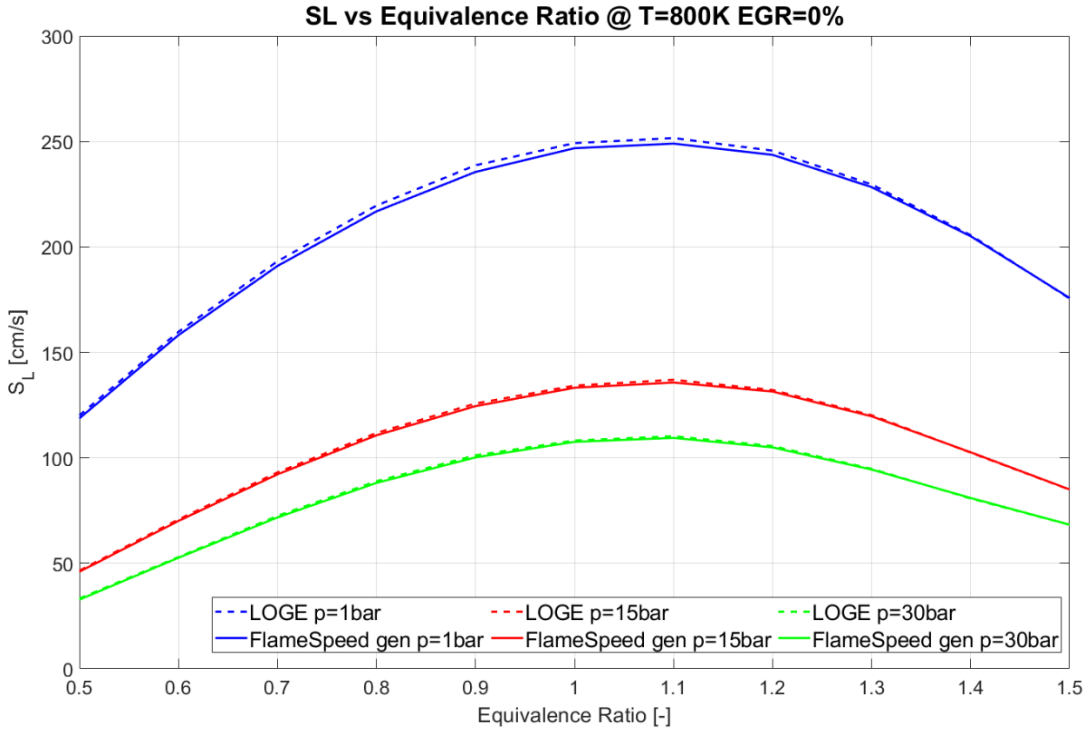

Figure 26: Comparison results of LOGE mechanism and of Flame Speed generator for ethane in function of Equivalence Ratio @ p=1bar,15bar,30bar EGR=0% and T=800K

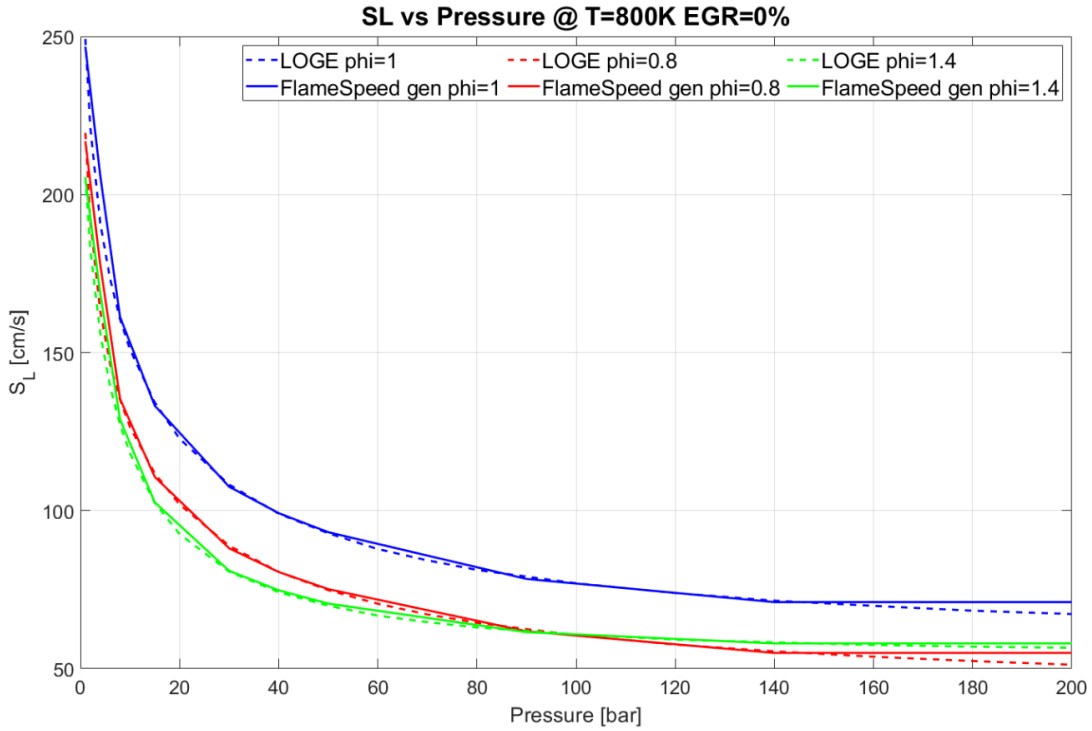

Figure 91: Comparison results of LOGE mechanism and of Flame Speed generator for ethane in function of Pressure @ phi=1,0.8,1.4, EGR=0% and T=800K

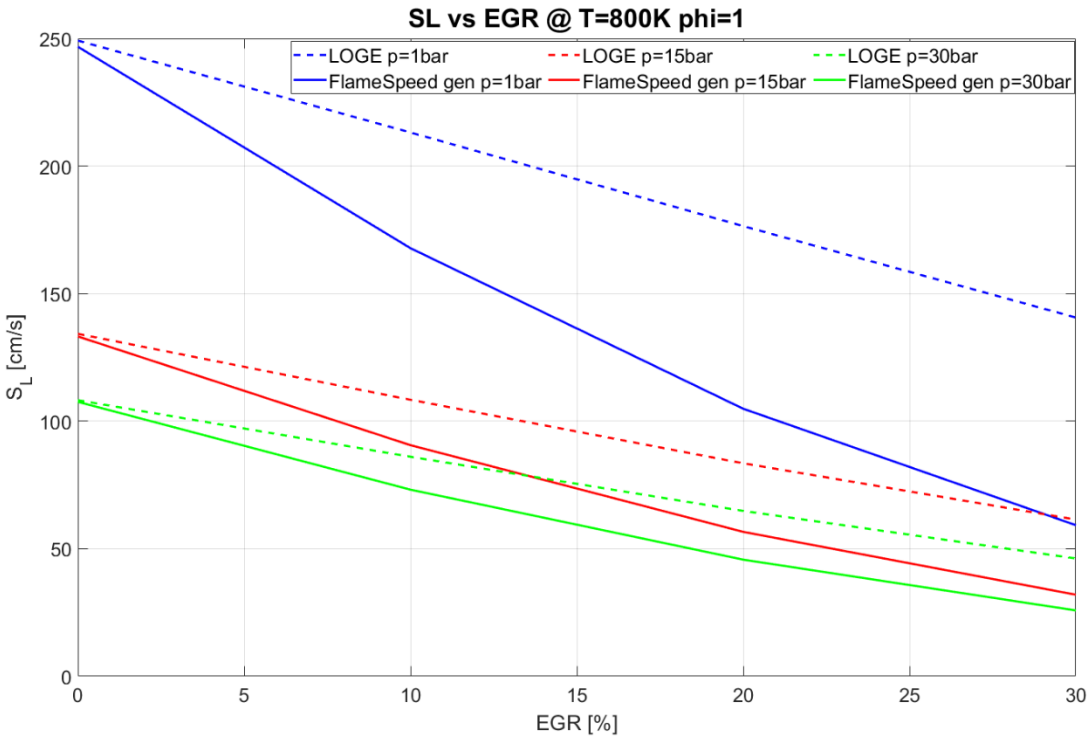

Figure 36: Comparison results of LOGE mechanism and of Flame Speed generator for ethane in function of EGR @ p=1,15,30, phi=1 and T=800K

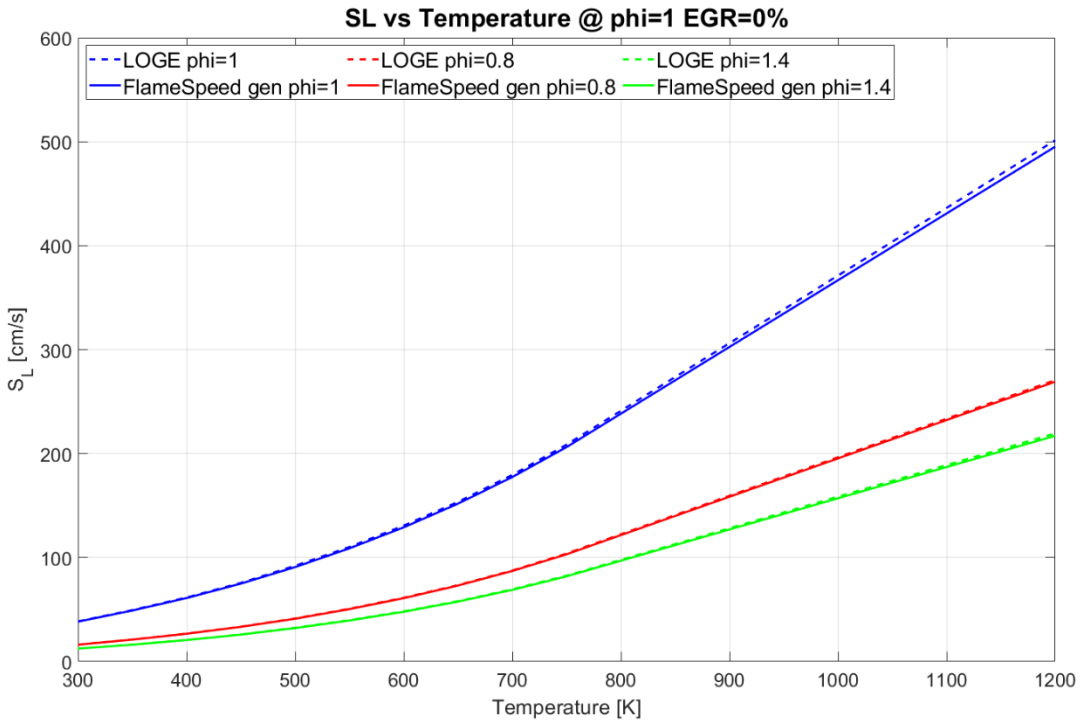

Figure 22: Comparison results of LOGE mechanism and of Flame Speed generator for propane in function of Temperature @ p=1bar,15bar,30bar EGR=0% and phi=1

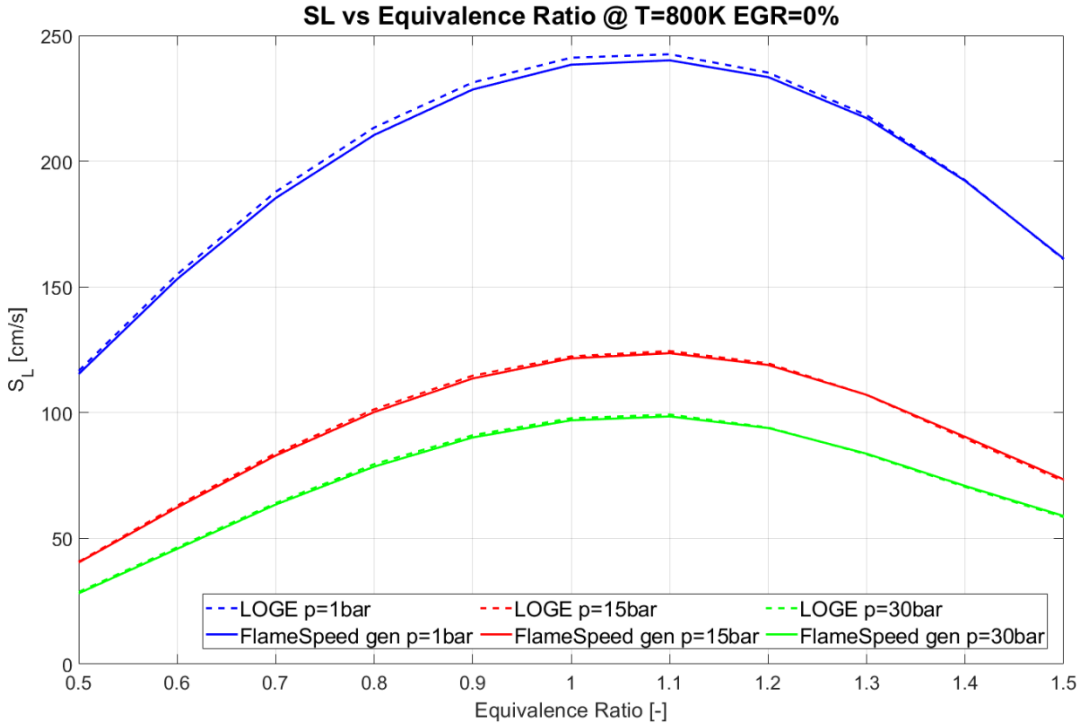

Figure 27: Comparison results of LOGE mechanism and of Flame Speed generator for propane in function of Equivalence Ratio @ p=1bar,15bar,30bar EGR=0% and T=800K

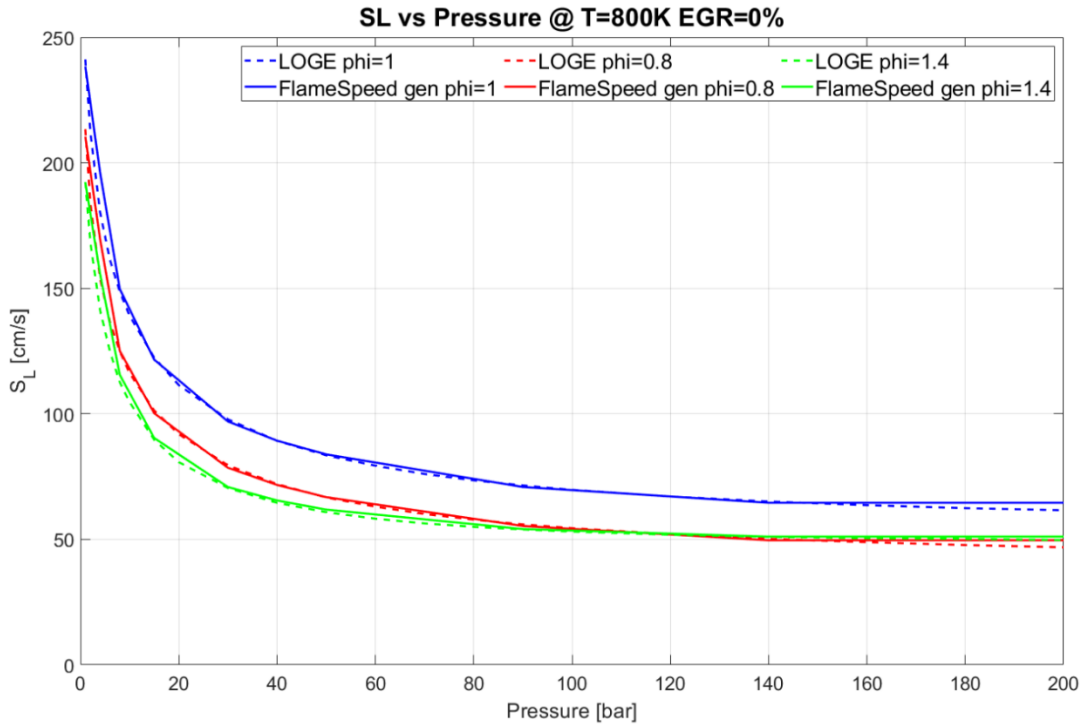

Figure 32: Comparison results of LOGE mechanism and of Flame Speed generator for propane in function of Pressure @ phi=1,0.8,1.4, EGR=0% and T=800K

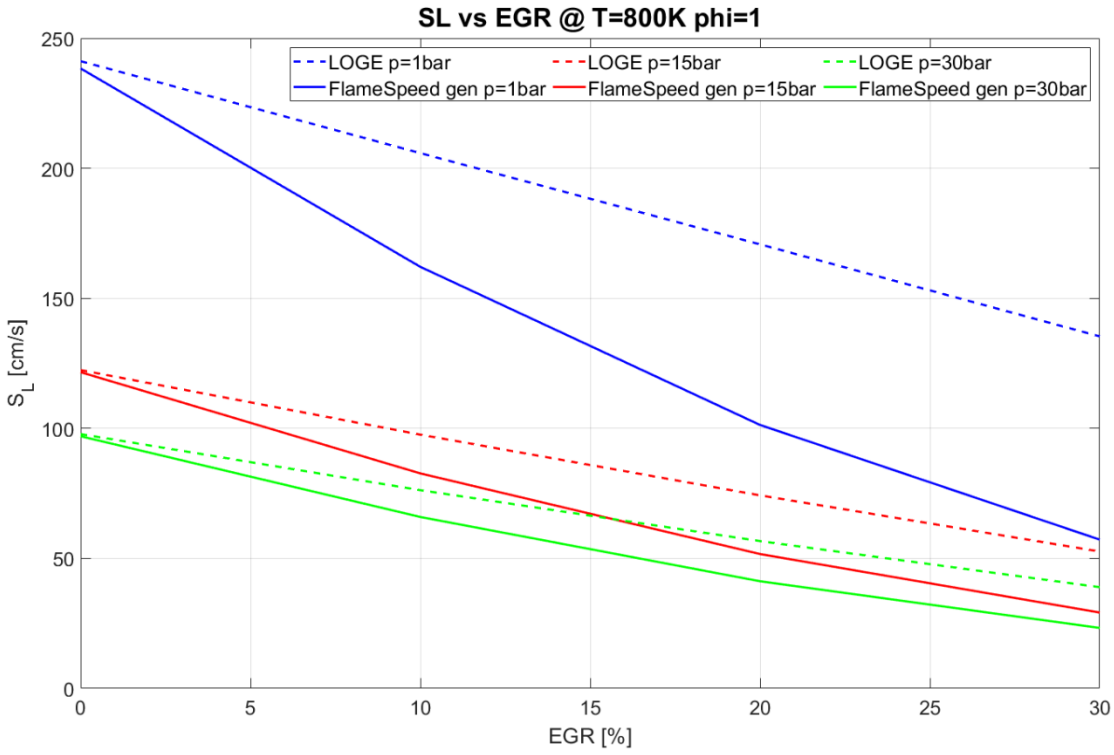

Figure 37: Comparison results of LOGE mechanism and of Flame Speed generator for propane in function of EGR @ p=1,15,30bar, phi=1 and T=800K

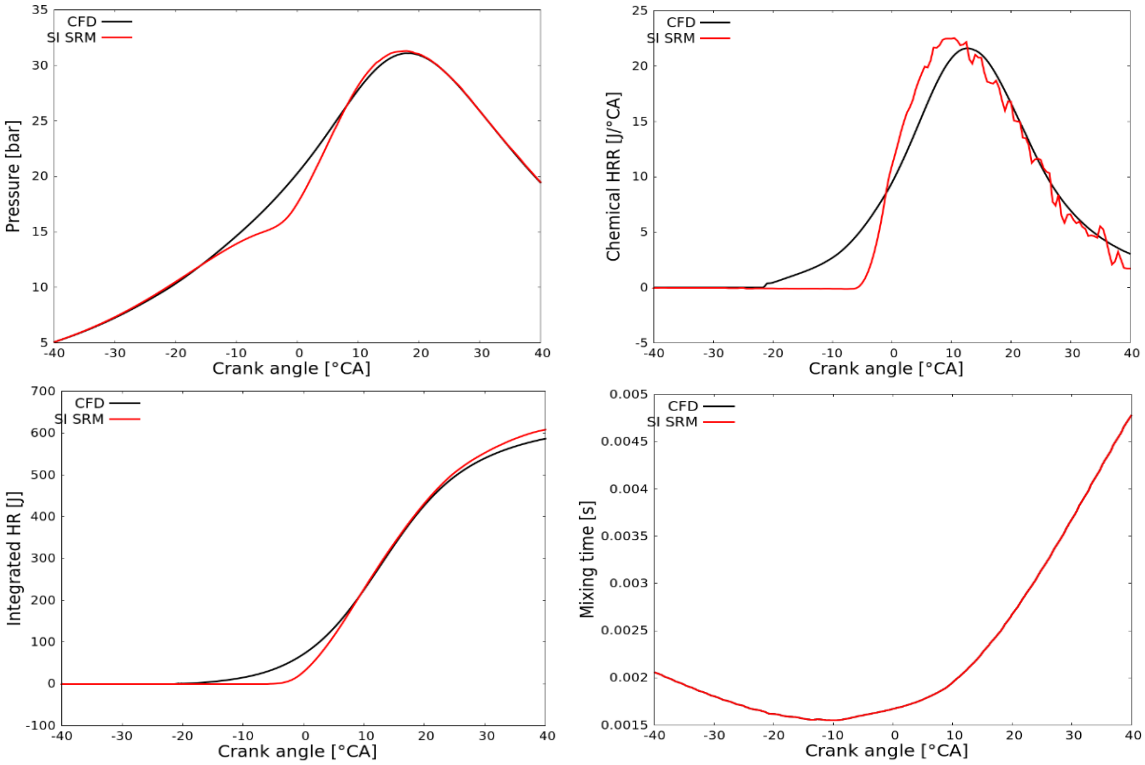

Figure 83: Pressure, Heat Release Rate, Integrated HR and mixing time obtained for both CFD and SRM for HCNG15

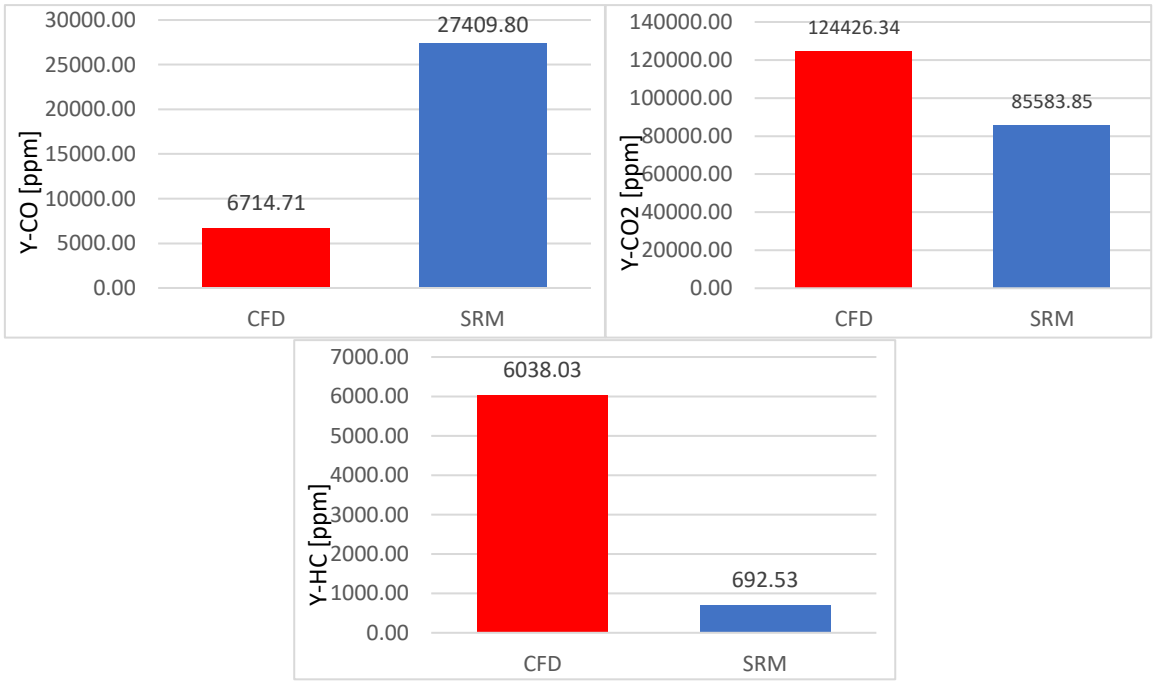

Figure 84: CO, CO2 and HC emissions obtained for both CFD and SRM for HCNG15

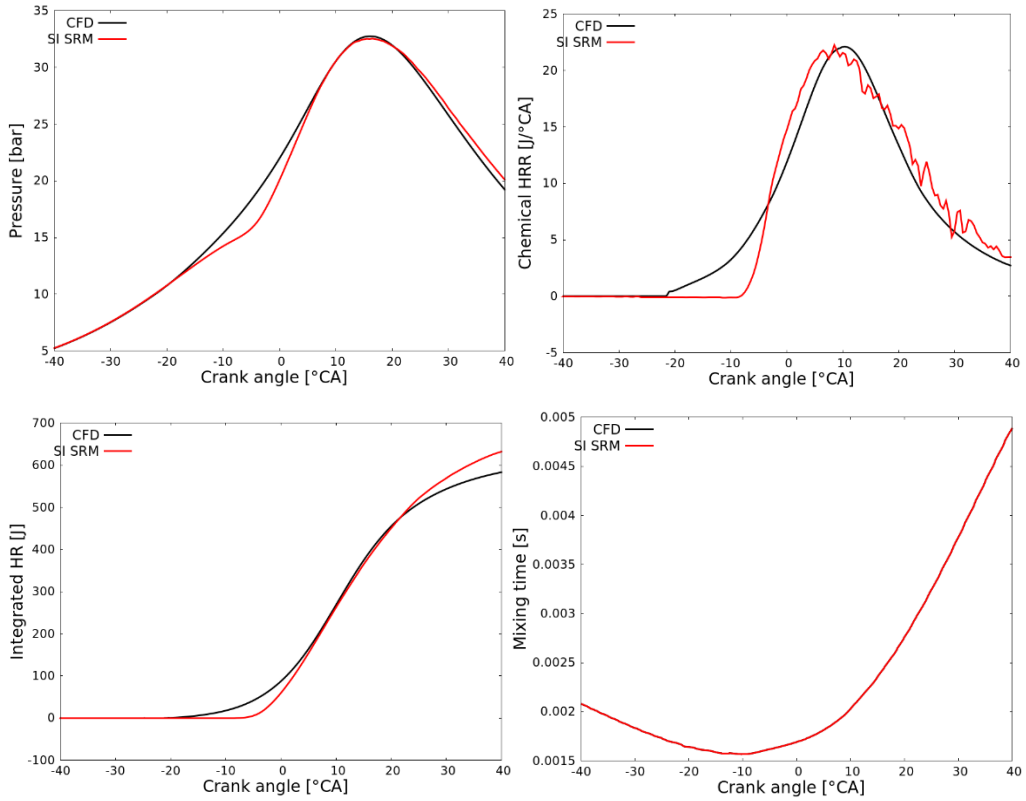

Figure 85: Pressure, Heat Release Rate, Integrated HR and mixing time obtained for both CFD and SRM for 8713

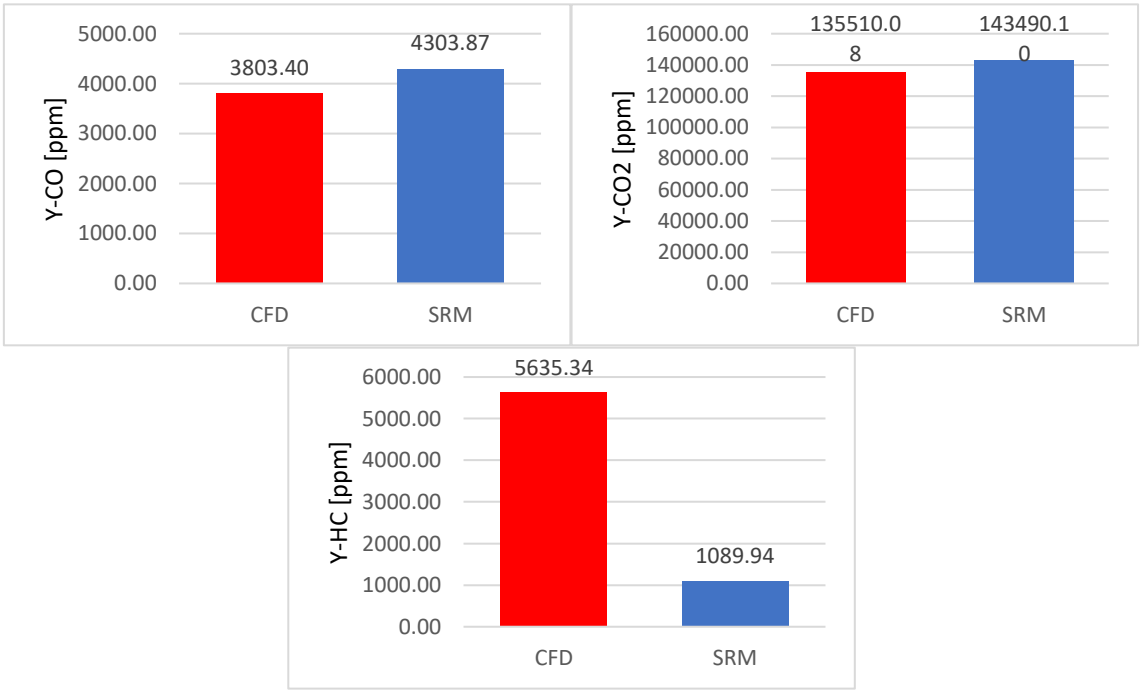

Figure 86: CO, CO2 and HC emissions obtained for both CFD and SRM for 8713

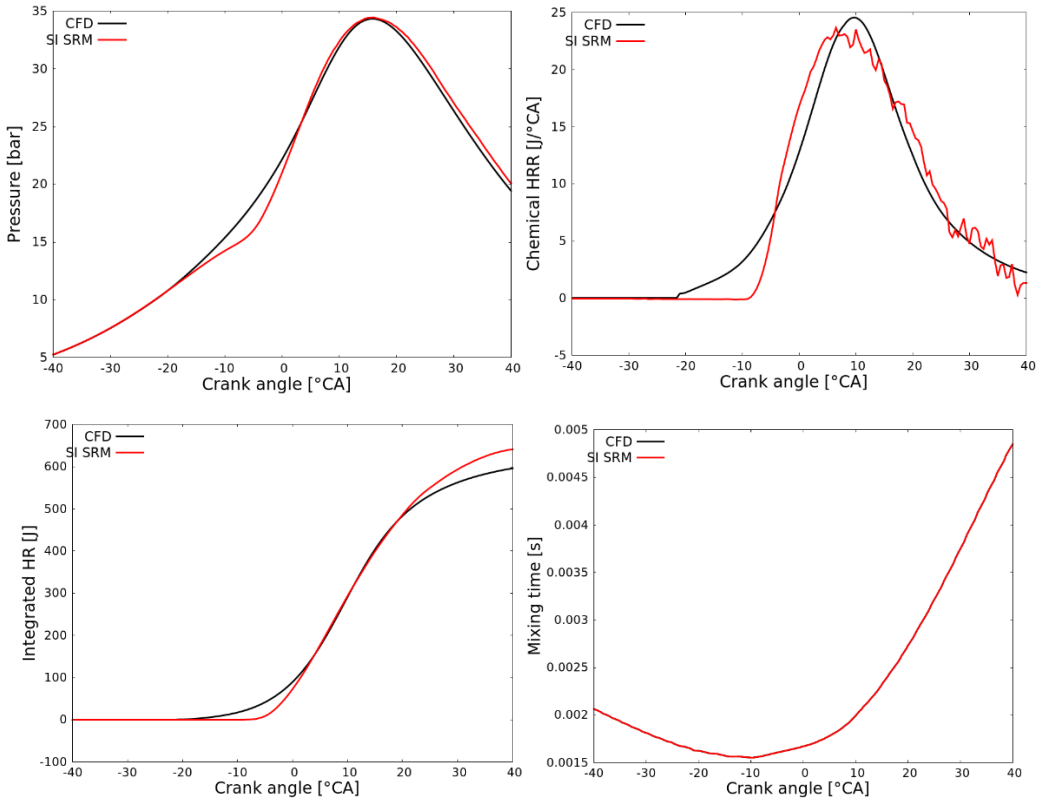

Figure 87: Pressure, Heat Release Rate, Integrated HR and mixing time obtained for both CFD and SRM for MIX

Figure 88: CO, CO2 and HC emissions obtained for both CFD and SRM for MIX

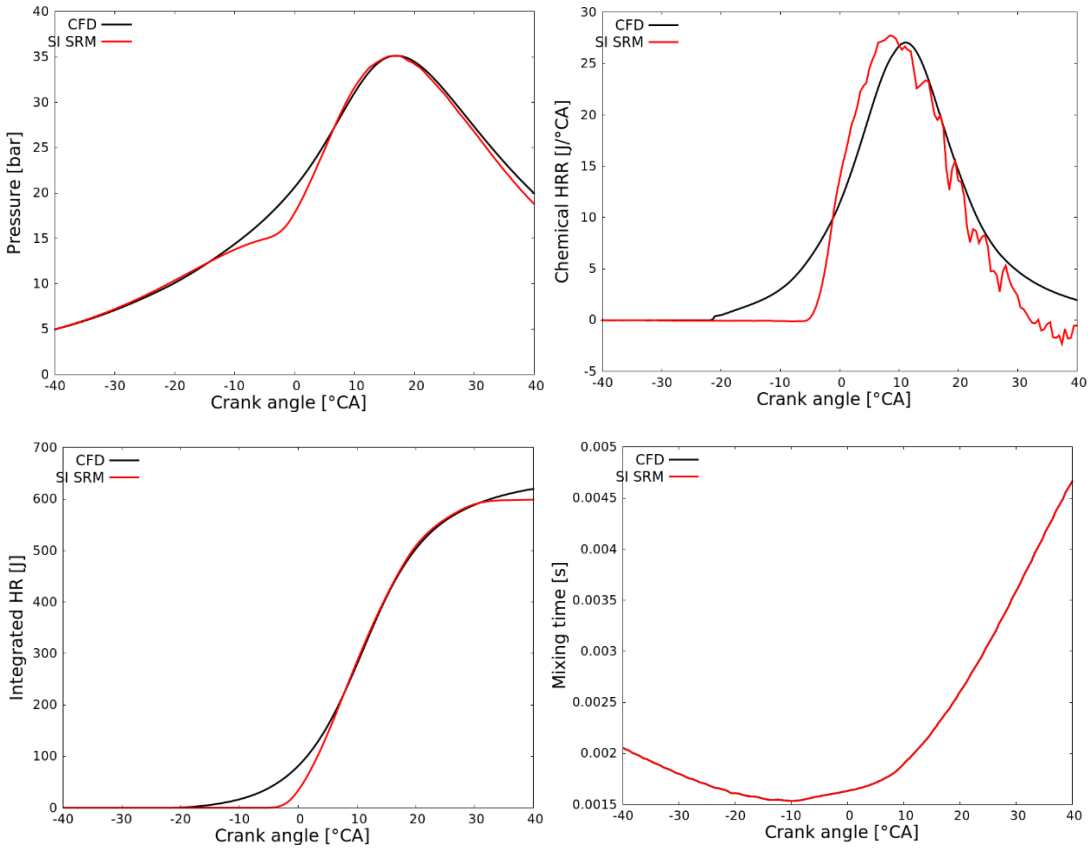

Figure 89: Pressure, Heat Release Rate, Integrated HR and mixing time obtained for both CFD and SRM for HCNG25

Figure 90: CO, CO2 and HC emissions obtained for both CFD and SRM for HCNG25

Bibliography

[1] Lecture notes of Federico Millo, 'Parametri prestazionali'

[2] Vagelopoulos, C.N., and Egolfopoulos,F.N., 'Direct Experimental Determination of Laminar Flame Speeds,' Paper WSS/CI 97S-022, Western States Section/Combustion Institute Meeting, Livermore, CA, 27(1):513:519. 1998.

[3] Vagelopoulos, C.M., Egolfopoulos, F.N. Law, C.K. *Proc. Combust. Inst.* 1994, 25, 1341

[4] Gregory P. Smith, David M. Golden, Michael Frenklach, Nigel W. Moriarty, Boris Eiteneer, Mikhail Goldenberg, C. Thomas Bowman, Ronald K. Hanson, Soonho Song, William C. ardiner, Vitali V. Lissianaski and Zhiwei Qin http://combustion.berkeley.edu/gri-mech/ *GRI-Mech Version 3.0*

[5] Thierry Poinsot, Denis Veynante 'Theoretical and Numerical Combustion, second edition'

[6] Joel H. Ferzieger, Milovan Perić 'Computational Methods for Fluid Dynamics', third edition

[7] Sadrehaghighi, Ideen.(2018).'Turbulence Modeling'

[8] Eric Furbo, 'Evaluation of RANS turbulence models for flow problems with significant impact of boundary layers' December 2010

[9] Irvin Glassman, 'Combustion', third edition December 1996

[10] Xiao Qin and Yiguang Ju. 'Measurements of burning velocities of dimethyl ether and air premixed flames at elevated pressures. Proceedings of the Combustion Institute' 30(1):233–240, 2005.

[11] L. Selle, T. Poinsot, and B. Ferret. Experimental and numerical study of the accuracy of flame-speed measurements for methane/air combustion in a slot burner. Combust. Flame, 158(1):146-154, 2011.

[12] K.J. Bosschaart and L.P.H. de Goey. The laminar burning velocity of flames propagating in mixtures of hydrocarbons and air measured with the heat flux method. Combustion and Flame, 136(3):261-269, 2004.

[13] X.J. Gu, M. Z. Haq, M. Lawes, and R. Woolley. Laminar burning velocity and Marksteins lengths of methane-air mixtures. Combust. Flame, 121(1-2):41-58, 2000

[14] A. Van Maaren, D. S. Thung, and L. P.H. De Goy. Measurement of Flame Temperature and Adiabatic Burning Velocity of Methane/Air Mixtures. Combust. Sci. Technol., 96(4-6):327-344, 1994

[15] Rte Hermanns. Laminar burning velocities of methane hydrogen air mixtures. PhD thesis, 2007

[16] Patricia Dirrenberger, Hervé Le Gall, Roda Bounaceur, Olivier Hebinet, Pierre Alexandre Glaude, Alexander Konnov, and Frédérique Battin-Leclerc. 'Measurements of laminar flame velocity for components of natural gas. Energy and fuels', 25(9):3875-3884, 2011

[17] T. Boushaki, Y. Dhué, L. Selle, B. Ferret, and T. Poinsot. 'Effects of hydrogen and steam addition on laminar burning velocity of methane-air premixed flame: Experimental and numerical analysis. Int. J. Hydrogen Energy', 37(11):9412-9422, 2012

[18] F. HV Coppens, J. De Ruyck and A.A. Konnov. 'Effects of hydrogen enrichment on adiabatic burning velocity and NO formation in methane + air flames. Exp. Therm. Fluid Sci.', 31(5):437-444, 2007

[19] F. Halter, C. Chaveau, N. Dhebaili-Chumeix, I. Gokalp. Characterization of the effects of pressure and hydrogen concentration on laminar burning velocities of methane-hydrogen-air mixtures, 30(1):201-208, 2005

[20] M. I. Hassan, K. T. Aung, and G. M. Faeth. Measured and Predicted Properties of Laminar Premixed Methane/Air Flames at Various Pressures, Combustion and Flame, 115:539-550, 1998

[21] O.Colin, A. Benkeida and C. Angleberger '3D Modeling of Mixing, Ignition and Combustion Phenomena in Highly Stratified Gasoline Engines',58(1):47-62, 2003

[22] Convegent Science, 'CONVEGE manual', April 2017

[23] Ugo Sorge, 'Simulazione multidimensionale ed ottimizzazione del processo di conversione dell'energia in motori ad iniezione diretta di benzina', PhD thesis

[24] R. Cracknell, B. Head, S.Remmert, Y. Wu, 'Laminar burning velocity as a fuel characteristic: Impact on vehicle performance', Woodhead Publishing 149-156, 2013

[25] Semin, Rosli and Abu Bakar, 'A Technical Review of Compressed Natural Gas as an Alternative Fuel for Internal Combustion Engines', 302-311, 2008

[26] T. Korakianitis, A.M. Namasivayam, R.J. Crookes, 'Natural-gas fuelled spark-ignition (SI) and compression-ignition (CI) engine performance and emissions',37(1):89-112, 2011

[27] Kirby S. Chapman, Amar Patil, 'Performance, Efficiency and Emissions Characterization of Reciprocating Internal Combustion Engines Fueled with Hydrogen/Natural Gas Blends', June 2007

[28] Igor V. Dyakov, Jacques De Ruyck, Alexander A. Konnov, 'Probe sampling measurements and modeling of nitric oxide formation in ethane + air flames',86(1-2):98-105 June 2006

[29] F. N. Egolfopoulos, D. L. Zhu and C. K Law, 'Experimental and numerical determination of laminar flame speeds mixtures of C_2 – hydrocarbons with oxygen and nitrogen', 23(1):471-478, 1991

[30] G. Jomaas, X. L. Zheng, D.L. Zhu, C.K. Law, 'Experimental determination of counterflow ignition temperatures and laminar flame speeds of C_2 – C_3 hydrocarbons at atmospheric and elevated pressures',30(1):193-200 2005

[31] Igor V. Dyakov, Jacques De Ruyck, Alexander A. Konnov, 'Measurement of adiabatic burning velocity in ethane-oxygen-nitrogen and in ethane-oxygen-argon mixtures',27(4):379-384, 2003

[32] William Lowry, Jaap de Vries, Michael Krejci and al., 'Laminar Flame Speed Measurements and Modeling of Pure Alkanes and Alkane Blends at Elevated Pressures',2:129:140, 2011

[33] Okjoo Park, Peter S. Veloo, Fokion N. Egolfopoulos, 'Flame studies of C_2 hydrocarbons', 34(1):711:718, 2013

[34] L.K. Tseng, M.A. Ismail and G.M. Faeth, 'Laminar burning velocities and Markstein numbers of hydrocarbon/Air Flames',95:410-426, 1993

[35] Munzer SY Ebaid and Katiaba JM Al-Khishali, 'Measurements of the laminar burning velocity for propane: Air mixtures',8(6):1-17, 2016

[36] M. Goswami, R.J.M. Bastiaans, L.P.H. de Gey, A.A. Konnov, 'Experimental and modelling study of the effect of elevated pressure on ethane and propane flames', 16:410-418, 2016

[37] O. Mathieu, J. Goulier, F. Gourmel, M.S. Mannan et al., 'Experimental study of the effect of CF_3I addition on the ignition delay time and laminar flame speed of methane, ethylene, and propane', 35(3):2731-2739, 2014

[38] C.H. Osorio, A.J. Vissotski, Eric L. Peterson, M.S. Mannan, 'Effect of CF_3Br on $C_1 – C_3$ ignition and laminar flame speed: Numerical and experimental evaluation', 160(6):1044-1059, 2013

[39] O. Park, P. S. Veloo, David A. Sheen et al, 'Chemical kinetic model uncertainty minimization through laminar flame speed measurements', 172:136-152, 2016

[40] Victor Yakhot and Steven A. Orszag, 'Renormalization Group Analysis of Turbulence, I. Basic Theory', 1(1), 1986

[41] O. Colin, A. Benkenida and C. Angelberger, '3D Modeling of mixing, ignition and combustion phenomena in highly stratified gasoline engines', 58(1):47-62, 2003

[42] Altair, 'https://web.altair.com/introduction-to-loge-9am'

[43] LOGERESEARCH Manual, Book 4, LOGE AB, Lund, 2017

[44] LOGERESEARCH Manual, Book 1, LOGE AB, Lund, 2017

[45] Michal Pasternak, Fabian Mauss, Marc Sens et al, 'Gasoline engine simulations using zero-dimensional spark ignitionstochastic reactor model and three-dimensional computational fluid dynamics engine model', 17(1):76-85, 2015

[46] Martin Tunér, 'Stochastic Reactor Models for Engine Simulations', 2008

[47] T. Hirasawa, C. K. Law, C. J. Sung, H. Wang and Z. Yang, 'Determination of Laminar Flame Speeds of Ethylene/n-Butane/Air Flames Using Digital Particle Image Velocimetry', nd Joint Meeting of the U.S. Section of the Combustion Institute, Oakland, CA, 2001

[48] Wei Li, Guoqing Wang, Yuyang Li et al, 'Experimental and kinetic modeling investigation on pyrolysis and combustion of n-butane and i-butane at various pressures'

[49] S. G. Davis, C. K. Law, 'Determination of and Fuel Structure effects on laminar flame speeds of C1 to C8 Hydrocarbons', 140:427-449, 1998

[50] C. L. Tang, Z.H. Huang, C.K. Law, 'Determination, correlation, and mechanistic interpretation of effects of hydrogen addition on laminar flame speeds of hydrocarbon-air mixtures', 33(1):921-928, 2011

[51] Hao Wu, Erjiang Hu, Huibin Yu et al., 'Experimental and Numerical Study on the Laminar Flame Speed of n-Butane/Dimethyl Ether–Air Mixtures', 28(5):3412-3419, 2014

[52] Hai Wang, Xiaoqing You, Ameya V. Joshi, Scott G. Davis, Alexander Laskin, Fokion Egolfopoulos, and Chung K. Law, 'USC Mech Version II. High-Temperature Combustion Reaction Model of H2/CO/C1-C4 Compounds. http://ignis.usc.edu/USC_Mech_II.htm', May 2007.

[53] https://convergecfd.com/blog/converge-workflow-tips

[54] Mirko Baratta, Daniela Misul, Ezio Spessa et al., "Effects of H2 Addition to Compressed Natural Gas Blends on Cycle-to-Cycle and Cylinder-to-Cylinter Combustion Variation in a Spark-Ignition Engine", 182-202, 2012.

[55] Fabian Mauss, "Gasoline engine development using LOGEengine", Altair User Conference

[56] LOGERESEARCH Manual, Book 3, LOGE AB, Lund, 2017

[57] LOGEengine Manual, LOGE AB, Lund, March 2018

[58] Técnico Lisboa, 'Characterization and behaviour Flame stabilization Ignition'